Dynamic Processes in Heavy-Ion Collisions at Intermediate Energies

Cover illustration: *Delay cables of the Huygens detectors. Each signal from each subdetector is sent through a 30 meter long cable. In the time needed for the signal to pass through the cable, it is electronically decided if a collision has occurred. If this is true, the signals are read out by the data-acquisition system.*

Bottom right on each page: *Sequence of images of an IQMD simulation of a heavy-ion collision at 45 A MeV with an impact parameter of 3 fm (clustered). The sequence is from back to front with time steps of approximately* 1.3×10^{-23} *seconds (4 fm/c).*

Voorkant: *Verletkabels van de Huygensdetectoren. Elk signaal uit elke subdetector wordt gestuurd door een kabel, die 30 meter lang is. In de tijd die het signaal nodig heeft om door de kabel te lopen, wordt elektronisch beslist of er een botsing is waargenomen. Als dat het geval is, worden deze signalen uitgelezen.*

Rechtsonder op elke pagina: *Opeenvolgende beelden van een IQMD-simulatie van een zware-ionenbotsing bij 45 A MeV met een botsingsdoorsnede van 3 fm (geclusterd). De simulatie loopt van achter naar voor met tijdstappen van ongeveer* 1.3×10^{-23} *seconden (4 fm/c).*

Dynamic Processes in Heavy-Ion Collisions at Intermediate Energies

Dynamische Processen
in Zware-Ionenbbotsingen
bij Intermediaire Energieën

(met een samenvatting in het Nederlands)

Proefschrift

TER VERKRIJGING VAN DE GRAAD VAN DOCTOR AAN DE UNIVERSITEIT VAN UTRECHT OP GEZAG VAN DE RECTOR MAGNIFICUS PROF. DR. H.O. VOORMA INGEVOLGE HET BESLUIT VAN HET COLLEGE VOOR PROMOTIES IN HET OPENBAAR TE VERDEDIGEN OP WOENSDAG 3 MAART 1999 DES OCHTENDS TE 10.30 UUR

DOOR

Edward Paul Prendergast

GEBOREN OP 19 FEBRUARI 1971 TE LONDON

promotor: Prof. Dr. R. Kamermans (UU)
copromotor: Dr. P.G. Kuijer (NIKHEF)

ISBN 90-393-1830-1

Contents

1 Introduction **1**
- 1.1 Nuclear matter under extreme conditions . . . 1
- 1.2 Heavy-ion collisions at intermediate energies . . . 4
- 1.3 Outline of this thesis . . . 6

2 Experimental set-up **9**
- 2.1 The Huygens detector array . . . 11
  - 2.1.1 The CsI(Tl) wall . . . 11
  - 2.1.2 The central trigger detector . . . 12
  - 2.1.3 The MUR . . . 17
- 2.2 Upgrade of the TPC . . . 18
  - 2.2.1 Computer simulations of the MSGC . . . 18
  - 2.2.2 Experimental MSGC test set-up . . . 21
  - 2.2.3 Experimental and simulation results . . . 22
  - 2.2.4 Discussion and conclusion . . . 24
- 2.3 Electronics and software . . . 25
  - 2.3.1 Hardware modules . . . 25
  - 2.3.2 The trigger . . . 27
  - 2.3.3 Data acquisition . . . 28
- 2.4 Beam and target . . . 28

3 The calibration of the Huygens detectors **31**
- 3.1 The passage of particles through matter . . . 32
  - 3.1.1 Energy-loss calculations . . . 32
  - 3.1.2 The light output of a plastic scintillator . . . 34
  - 3.1.3 Time of flight through a medium . . . 35
- 3.2 Detector calibration . . . 37
  - 3.2.1 The MUR . . . 37
  - 3.2.2 The central trigger detector . . . 38
  - 3.2.3 The CsI(Tl) wall . . . 44
- 3.3 Detector performance . . . 45
  - 3.3.1 Acceptance and identification properties . . . 45
  - 3.3.2 The GEANT detector simulation . . . 47
  - 3.3.3 Conclusions . . . 49

4 Model calculations **51**
4.1 Introduction 51
4.2 The equation of state 56
4.2.1 The Skyrme potential 56
4.3 Isospin Quantum Molecular Dynamics 59
4.3.1 Theory 59
4.3.2 The IQMD program and the cluster algorithm 62
4.3.3 Results for ^{24}Mg+^{27}Al at 45 and 95 AMeV 63

5 Results and discussion **69**
5.1 Impact-parameter selection 70
5.2 Collective motion 72
5.2.1 Event-plane reconstruction 73
5.2.2 Directed in-plane flow 76
5.3 Azimuthal correlations and polar angles at mid-rapidity 80
5.3.1 Introduction 81
5.3.2 Acceptance and efficiency 82
5.3.3 Results 85
5.3.4 Discussion 89
5.4 Conclusions 91

Bibliography **93**

Summary **99**

Samenvatting **101**

Dankwoord **103**

Curriculum Vitae **105**

1

Introduction

This thesis describes the study of heavy-ion reactions at intermediate energies. In particular, it focusses on the multifragmentation process of small nuclear systems. Several features of these heavy-ion reactions and the way they are measured are discussed in detail and, at the end of this work, conclusions are drawn for specific (small) nuclear systems. In this chapter, however, a more general approach to the study of nuclear collisions is adopted.

Section 1.1 gives an overview of the field of heavy-ion collisions. It elaborates on the motivations for the study of these processes and indicates in what way other fields in physics might benefit from the results. Section 1.2 concentrates on the intermediate-energy heavy-ion collisions. First, the collective flow effects observed at these energies are focussed on. Then the nature of the particle-production process is discussed. This is the central topic of this thesis. The final section of this chapter shows the outline of this thesis.

1.1 Nuclear matter under extreme conditions

Heavy-ion collisions are the only way to create nuclear matter under extreme conditions in a laboratory situation. Studying these reactions is, therefore, the only method to explore the temperature-density relationship of nuclear matter. In fig. 1.1 a phase diagram of nuclear matter is sketched. The full lines indicate the phase boundaries of the nuclear material. The other lines show regions where nuclear matter in the indicated situations exist. All lines in this figure have large errors on their positions, and might in fact be disputed all together. This field in physics is still very much under investigation, the diagram should, therefore, only be seen as an indication of the

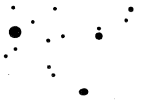

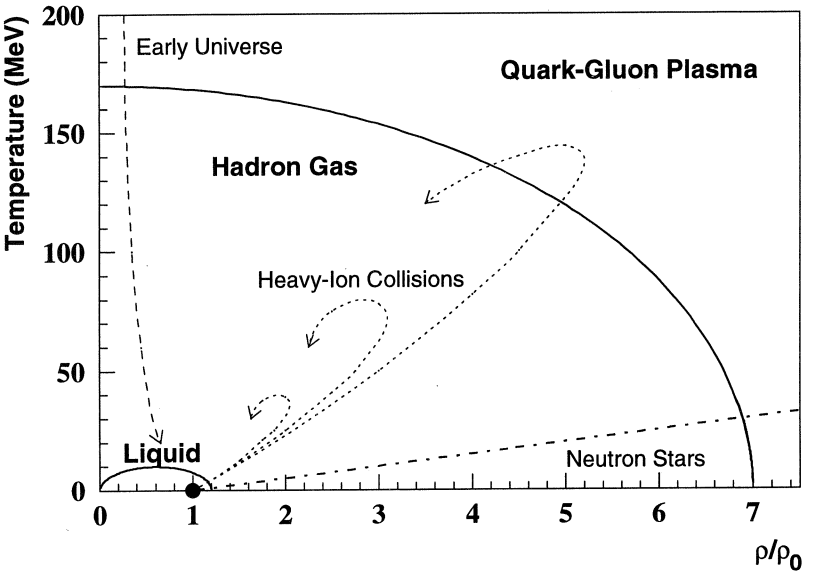

Figure 1.1: *Phase diagram of nuclear matter. On the vertical axis the temperature is plotted (in MeV), the horizontal axis indicates the baryon density normalised to the density of the ground state of nuclear matter ($\rho_0 = 0.15\ fm^{-3}$).*

processes which could take place at different points in the temperature-density plane of nuclear matter.

The phase transitions of nuclear matter

Normal nuclear matter exists at zero temperature and at density $\rho_0 = 0.15\ \mathrm{fm}^{-3}$. In fig. 1.1 the ground state is indicated with a black dot. In fact only this state of nuclear matter has been investigated thoroughly and has resulted in the development of the nuclear shell model [1, 2] and, therefore, increased the understanding of the nuclear forces within the nucleus. It was found that the nucleon-nucleon interaction is very similar to a Van der Waals force, with a short range repulsive and a long range attractive component. At low temperatures and pressure, such as the ground state, nuclear matter behaves similar to a liquid drop. Like a Van der Waals gas, it is expected that by increasing the temperature, and/or pressure in the nuclear material a phase transition occurs from a liquid-like state to a gaseous phase in which the nucleons move freely in the nuclear volume. In this state the matter consists of hadrons, which are made up of quarks and gluons. By increasing the temperature and/or density further a second phase transition of nuclear matter is expected, where the hadronic nature of matter is lost and a system is created consisting solely of quarks and gluons. This phase, where the quarks and gluons are no longer confined to the hadronic structure,

is called the quark-gluon plasma. At low temperatures this transition is expected at baryon density $\rho = 5\text{-}10\rho_0$, whereas for $\rho = 0$, lattice gauge calculations show that the quark-gluon plasma is created at 150-200 MeV [3, 4]. The shape of the phase diagram in the intermediate region is hitherto unexplored.
As was already stated, the exact position and nature of the phase transitions is still under investigation. The relationship between the macroscopic quantities like temperature and density, as plotted in fig. 1.1, is described by the equation of state (EOS) of nuclear matter. The determination of EOS can be regarded the Holy Grail of this field of physics [5].

Cosmologic interests

Nuclear matter normally exists in the ground state. Only at extreme conditions does nature itself explore the temperature-density plane of nuclear matter. Nowadays these conditions are only present in neutron stars and supernovae. However, just after the creation of the universe, in the *Big Bang* scenario, the complete universe traversed the nuclear phase transitions [6].
In fig 1.1 the path which the early universe followed in the first minutes of its existence is indicated with the dashed line. After its creation the universe is extremely hot and spatially confined. Its rapid expansion causes cooling of the existing matter. After approximately 10^{-5} seconds the universe, then consisting of photons, (anti-)leptons, (anti-)quarks and gluons, is approximately 1 km in diameter. At this point in time it reaches the phase transition between the quark-gluon plasma and hadronic matter and all free quarks are *condensed* into hadrons. The universe keeps expanding and a free hadron gas exists until approximately 10^2 seconds when nucleosynthesis sets in. In this final phase transition the light nuclei are created (nuclei with $Z > 7$ do not originate from this time, but are essentially made in stars only).
At present neutron stars are expected to (partially) consist of nuclear matter at high pressure. In fig 1.1 the area is indicated in which neutron stars can exist. After a star burns up all its nuclear fuel, gravity is no longer compensated by the radiative pressure of the nuclear fusion processes in the core and a star collapses. In such a supernova nuclear matter, especially in the core, is extremely compressed. If the star is heavy enough (between approximately 1.4 and 3 times the solar mass after the collapse) it will end up as a neutron star [7]. In these stellar objects gravity is so strong, that it compresses the complete mass into basically one single nucleus consisting mainly of neutrons. Near the surface the density of the neutron star has approximately the normal nuclear density, however, the pressure increases towards the centre of the star. It is speculated that the core of neutron stars could consist of a 'cold' quark-gluon plasma [8, 9]. Note that the EOS, i.e. the compressibility, of nuclear matter has a direct influence on the size and nature of neutron stars [10].

Heavy-ion collisions

During heavy-ion collisions, nuclear matter is strongly compressed and reaches high temperatures. This makes it possible to probe the pressure-density plane of nuclear matter.

Heavy-ion collisions are generally studied in fixed target experiments, where an accelerator provides pulses of energetic ions which are directed onto a (thin) target. The intensity of the beam and the thickness of the target are determined so that only one nucleus from the beam pulse collides with one target nucleus. By varying the energy of the beam and the mass of the colliding systems, different regions in the temperature-density plane of nuclear matter can be explored. In fig 1.1 the trajectories of heavy-ion collisions are sketched. Heavy-ion reactions are divided in three categories; intermediate energy, relativistic and ultra-relativistic heavy-ion collisions [10]. Below, the different categories are discussed briefly.
In this thesis intermediate-energy heavy-ion collisions are studied. These are roughly defined as collisions with a projectile energy between 10 and 100 AMeV, where A stands for the atomic mass number of the nucleus and AMeV is the energy per nucleon of an ion in MeV. Although, at these energies, only a small region of the phase diagram of nuclear matter is probed, the energy regime is of great interest for the study of the EOS. Firstly, because the reactions take place below the pion-production threshold, therefore, the kinetic energy of the system is (approximately) a preserved quantity. Secondly, because in this energy domain the phase transition between the nuclear liquid and the hadron gas can be studied. This phase transition is the basis for the nuclear multifragmentation process which is the central topic of this thesis.
Relativistic heavy-ion collisions have a projectile energy between 0.1 and 10 AGeV. The nuclear matter is compressed and heated more than in the intermediate-energy domain. At these higher energies a strong separation is present between nucleons participating in the reaction (from the overlap region) and *spectator* nucleons which retain their target or projectile velocity. Mainly the compressibility and other basic properties, such as in-medium cross sections, are studied. The most dominant collective process is a strong sideward flow (discussed in the next section), which is used to extract information on the EOS.
The ultra-relativistic heavy-ion collisions are performed at the most powerful accelerators available and have a beam energies up to 200 AGeV. The main goal of these studies is to verify experimentally the existence of the quark-gluon plasma. Although the most optimistic theoretical estimates show it is possible to create this phase already at 10 AGeV, it is extremely difficult to find a signal from the plasma in the enormous background from the hot-hadronic phase. So far no conclusive experimental evidence has been found for the quark-gluon plasma. For the near future, very energetic colliding-beam experiments are planned, which are expected to yield a clear signature from the plasma.

1.2 Heavy-ion collisions at intermediate energies

The experiments described in this thesis were performed with ^{24}Mg beams on a ^{27}Al target at 45 and 95 AMeV and are thus classified in the intermediate-energy range. As was already stated, this energy range explores an intriguing area in the phase diagram of nuclear matter. The collisions are expected to probe the phase transition between the nuclear fluid and the hadron gas. Information about the compressibility of nuclear matter is generally extracted from the collective motion of the colliding nuclear mate-

rial. The phase transition itself is studied via particle-emission processes, in particular the emission of intermediate-mass fragments (IMFs), usually defined with $Z \geq 3$, where Z is the atomic number of the fragment. However, as this thesis studies very small nuclear systems, i.e. ^{24}Mg+^{27}Al, $Z = 2$ is also incorporated in our investigation.

Directed flow

The interaction of the colliding system is governed by two opposite forces, both originating from the nucleon-nucleon potential. On the one hand, there is the attractive mean-field potential, the force which binds all nuclei, and on the other hand is the repulsive nucleon-nucleon hard-core interaction. The combination of these forces is the basis of the EOS. In the intermediate-energy range an interesting phenomenon occurs. At low energies ($E_{\text{beam}} \lesssim 40$ AMeV), the attractive mean-field potential dominates the reaction, resulting in a attractive force. Higher on the energy scale ($E_{\text{beam}} \gtrsim 100$ AMeV), the repulsive nucleon-nucleon collisions combined with the repulsive force from compression becomes stronger than the mean field, resulting in a repulsive interaction between the colliding systems. Both processes cause a sideward flow in the reaction plane, usually referred to as *directed in-plane flow*. At the *balancing energy* (E_{bal}), the two opposite forces are equal and no sideward flow is observed. This E_{bal} depends on the compressibility of nuclear matter and thus on the EOS. It is generally believed that measurement of E_{bal} is important for the determination of the EOS. Both experiment and simulations have shown that E_{bal} increases in energy with $A^{-1/3}$, where A is the summed mass of the target and projectile nuclei (e.g. [11, 12]). However, this relationship does not lead to a single possible value for the EOS. Experimental difficulties in the determination of the impact parameter and the reaction plane, which both have a great influence on the flow [13, 14, 15] are further obstacles in the accurate determination of the EOS with directed in-plane flow.

Dynamic or statistical multifragmentation?

The main goal of the study described in this thesis is to investigate the multifragmentation process of ^{24}Mg+^{27}Al. For small nuclear systems such an investigation has not yet been performed and for large systems the experimental results are heavily debated. The measured data presented in this thesis are clear evidence of dynamic IMF-production in small nuclear systems.

The multifragmentation process is directly associated with the phase transition between the nuclear liquid and the hadron gas [16, 17]. This process, where a sizable amount of the exit channel is occupied by IMFs was found to start at beam energies of approximately 35 AMeV [18]. It is speculated that after the initial compression and heating up of the nuclear system, it decompresses and cools into a region of the pressure-density plane where $\frac{dP}{d\rho} < 0$. In this region, the *spinodal region of instability*, nuclear matter is not mechanically stable and will *condense* into several small fragments: the IMFs. This process is discussed in more detail in section 4.2. Although there is general consensus that this process is indeed responsible for multifragmentation, the nature of the process is still debated. Two schools of thought are currently in a heated discussion about

the interpretation of the observed IMF spectra of systems with a combined mass of 200-250 amu [19, 20, 21]. The classical picture of IMF emission from a single (rotating) mid-rapidity source (statistical IMF production) [22, 23, 24, 25, 26] is challenged by the recent suggestion that the IMF emissions are a purely dynamic process [27, 28, 29, 30]. Although multifragmentation originates for both scenarios in the spinodal region of instability, they show a fundamental difference. IMF emission from a single source requires an equilibrated hot compound nucleus, which has lost, by definition, all information about its initial state. The dynamic scenario, however, has a strong initial-final state correlation. In section 5.3, this correlation is used to show that for small nuclear systems IMF production is a dynamic process.

The Huygens detectors

To measure the above-mentioned processes, the department of subatomic physics at Utrecht University designed and built the Huygens Detectors [31]. Because intermediate heavy-ion collisions are fixed-target experiments, the Huygens detectors have an asymmetric geometry with respect to the beam direction. In azimuthal angle they are completely symmetric. Each part of the Huygens detectors is adapted to cope with the specific conditions it endures in experimental conditions. The backward hemisphere is covered by a wall consisting of 64 CsI(Tl) crystals with low-energy detection thresholds (the CIW). In this region very few light particles with low energies are expected. The mid-rapidity region is covered by a time projection chamber (TPC) with multi-hit capacity, backed by an array of in total 48 plastic scintillators. In this region a good coverage in both energy and Z is necessary, to study the mid-rapidity IMF emissions. In the forward region 16 plastic scintillators of the Huygens detectors and the MUR [32], a forward time-of-flight wall consisting of 96 plastic scintillator sheets are located. In the forward region many, predominantly light particles with high energies, are expected. At low angles also projectile residues are detected in the MUR.
For data taking the Huygens detectors were used at the accelerator institute GANIL (Grand Accélérateur National d'Ions Lourds) in Caen (France). The experiment was performed in May 1996, with the primary goal to study the multifragmentation process of ^{24}Mg+^{27}Al at different beam energies. Due to technical problems it was only possible to measure at 45 and 95 AMeV. In total approximately 27×10^6 events were recorded on tape. For the analysis 3.9×10^6 events were used of 45 AMeV beam energy and 8.0×10^6 events of 95 AMeV beam energy.

1.3 Outline of this thesis

The goal of the investigation described in this thesis is the study of the multifragmentation process in ^{24}Mg+^{27}Al at 45 and 95 AMeV. Each chapter describes the successive steps which have to be taken in order to achieve this objective.
In chapter 2 the experimental set-up is described. In particular the investigations for the upgrade of the Huygens detector for the May 1996 experiment are elaborated on. After the experiment was performed all detector elements were calibrated individually. This process is explained in chapter 3. First the general theory of calibration, which

was partially developed for the Huygens detectors, is discussed. Then the calibration of the successive subdetectors of the Huygens detector array is focussed on.
Because of the complexity of the nuclear reaction it is not possible to interpret the data without making use of elaborate theoretical simulations. For these simulations the Isospin Quantum Molecular Dynamics (IQMD) model was used, which is described in chapter 4.
In chapter 5, finally the nuclear reaction itself can be studied. First the collective flow is focussed on. The experimental data show a strongly reduced flow at 95 AMeV compared to 45 AMeV. Then the multifragmentation process is studied. The data is compared to a statistical and a dynamic (IQMD) model, which reveals that IMF production in ^{24}Mg+^{27}Al at 45 and 95 AMeV is a dynamic process.

2

Experimental set-up

The experiments described in this thesis were performed at the GANIL heavy-ion beam facility in Caen (France). GANIL provided ^{24}Mg beams with energies of 45 and 95 AMeV. The beam was directed onto an aluminium target foil. The measurements of the ^{24}Mg+^{27}Al-collisions were performed using the Huygens detectors [31, 33]. This detector array was conceived and built at the department of subatomic physics at Utrecht University for the study of heavy-ion collisions at intermediate energies. The Huygens detector array covers (almost) the complete phase space and is, therefore, called a 4π-detector. This makes it possible to do an *event by event* analysis of the reaction. The Huygens detectors were used in conjunction with a forward time-of-flight wall, the MUR [32]. In fig. 2.1 an overview of the experimental set-up is shown. The set-up is approximately 2.3 m in length and at maximum (the MUR) 2.5 m in height and width. It is completely situated within the NAUTILUS, a large vacuum vessel. In fig. 2.1 the beam enters from the right. The target is located within the Huygens detectors. In the backward hemisphere the CsI(Tl) wall (CIW) covers 80% of the phase space. The main subdetector of Huygens is the central trigger detector (CTD), which covers the mid-rapidity region of the collisions described in this thesis. It has full azimuthal coverage from 11° to 78° in polar angle in the laboratory frame. The CTD consists of a time projection chamber (TPC) with microstrip read-out and an array of 48 plastic scintillators. The microstrips measure the angle and energy loss of the particle in the chamber. Particle identification and energy determination are achieved using the energy loss in the gas and the total energy measured in the plastics. Energetic particles in the forward region pass through the CTD and are also detected in the MUR. The MUR covers 3° to 30° in polar angle and consists of an array of thin plastic sheets. It is located 2.1 m from the target. The MUR measures the flight time of the particle and the energy loss in the sheet. For particles passing through the chamber to the MUR, the flight time of a particle to the MUR is combined with the

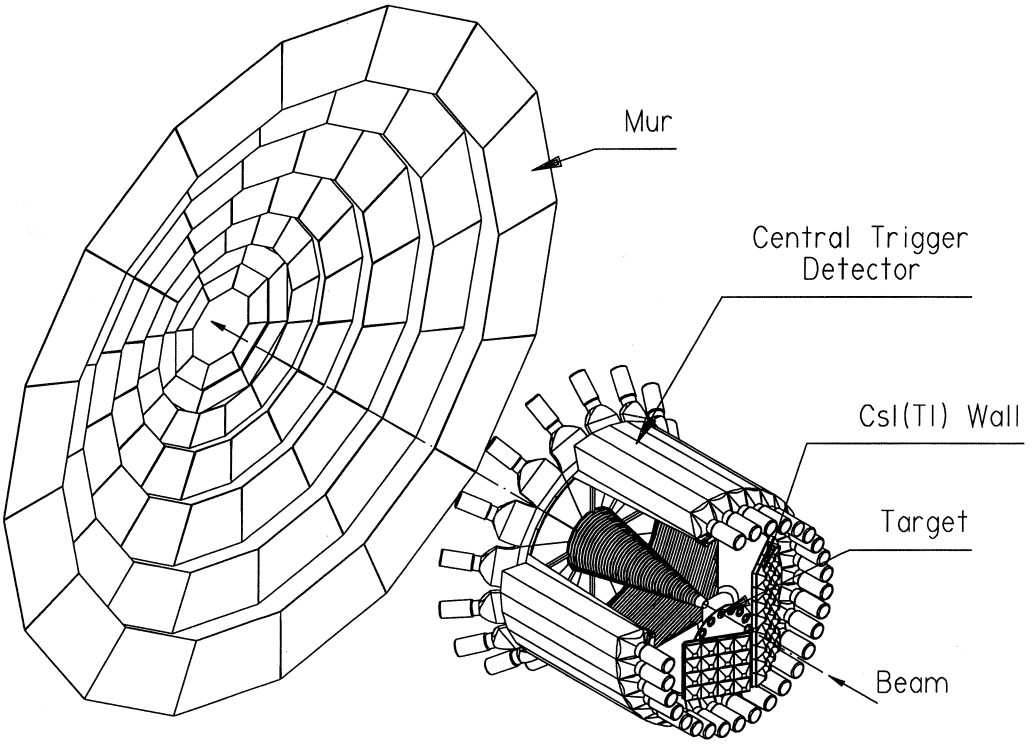

Figure 2.1: *The Huygens detector array. The beam enters the set-up from the right. The target foil is located inside the Huygens detectors. The detector array consists of three main parts, the CsI(Tl) wall in the backward region and the time projection chamber in the mid-rapidity region. The forward region is covered by the MUR, a time-of-flight wall located 2.1 m from the target.*

energy loss in the forward plastic to obtain particle identification. Particles between 3° and 10° in polar angle are only detected in the MUR. These particles are identified using the time-of-flight and the energy-loss information in the MUR.

In this chapter the experimental set-up is described. First the three subdetectors are discussed individually, in subsection 2.1.1 the CIW, in subsection 2.1.2 the CTD and finally in subsection 2.1.3 the MUR. An elaborate investigation was done in order to upgrade the TPC to increase the Z-coverage to $Z = 2$. This is discussed in section 2.2. The Huygens detectors include specially designed electronics, which are described in section 2.3. This section also elaborates on the trigger and the data-acquisition software. Section 2.4 discusses the characteristics of the beam and the target.

2.1 The Huygens detector array

The Huygens detectors were designed for the study of heavy-ion collisions at intermediate energies. The physics goal for the detector was to be able to do an *event by event* analysis of the reaction. Coverage of (almost) the complete phase space is therefore required. Heavy-ion collisions are generally fixed target experiments, this has important implications for the detector set-up. The Lorentz-boost will make the particle distribution forwardly peaked. Very few fragments will be emitted in the backward region and the energy of these fragments will be low. In the forward region energies up to twice the beam energy must be expected. Therefore, the Huygens detectors are asymmetric in polar angle and symmetric in azimuthal angle. In this section the different subdetectors of Huygens are discussed, including the MUR, which was kindly put at our disposal by the LPC (Laboratoire de Physique Corpusculaire) in Caen.

2.1.1 The CsI(Tl) wall

In a fixed-target heavy-ion experiment very few particles are emitted in the backward hemisphere. The only particles that have a reasonable probability to be detected in this region originate from target (spectator) emission. Generally these fragments will have low kinetic energies. The detector covering the backward hemisphere can therefore be relatively simple. In the Huygens detector the backward hemisphere is covered by a wall of 64 CsI(Tl) crystals (CIW). This inexpensive solution combines a low detection threshold with sufficient angular resolution.

Fig. 2.2 shows a schematic picture of the CIW. The 64 modules are stacked in two blocks of each 8×4 crystals. These two blocks are placed with a mutual angle of 120° left and right of the beam The centre of the double structure is located 12.7 cm from the target. Each of the 64 detector modules is 5×5 cm^2, with an effective area of 4.8×4.8 cm^2. The crystals are 1 cm thick. The CIW is located between 121° and 177° in polar angle and covers approximately 80% of the backward hemisphere.
Each crystal is connected to a trapezoidal light guide, resulting in a position-independent signal to within 5%. All crystals are covered by a 12 μm thick mylar foil, which has three advantages. Firstly, this foil stops electrons and some of the γ-rays coming from the target. Secondly, it reflects the produced light in the crystal increasing the light yield by a factor of 1.3. Thirdly, it isolates the crystal optically from the rest of the set-up. The light guide is read-out by a 1×1 cm^2 photo-diode (Hammamatsu S1790-04). The signal from the diode is amplified by a PAC-LP87 preamplifier. The threshold of the mylar foil and the electronic noise of 950 electrons from the diode-preamplifier combination yield an intrinsic detection threshold of 1 AMeV. Particles with energies above 40 AMeV will not be stopped in the 1 cm thick crystal and can therefore not be identified correctly.

The intrinsic properties of CsI with Tl doping can be used to achieve both particle identification and energy determination. This makes it possible to use the crystals without the complication (and energy-threshold enhancement) of a transmission detector in front of the module. The deposited energy of particles stopped in a CsI(Tl)-crystal

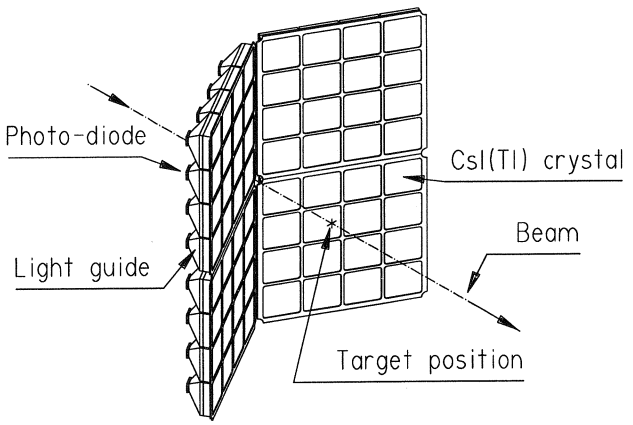

Figure 2.2: *Three dimensional view of the CIW.*

will predominantly be released by scintillation processes. The time characteristics of these processes can be used for particle identification and the amplitude of the produced light is a measure of the deposited energy [34, 35]. In pure CsI two scintillating processes dominate the light production in the matrix [36, 37]. The first originates from the decay of self-trapped excitons and has a wavelength of approximately 320 nm. The second is due to the luminescence of I^--vacancies and emits photons of around 420 nm. If Tl is introduced in the crystal, the characteristics of the light output changes [38]. The 320 nm radiation is reabsorbed by the Tl^+-ions. The decay of the excited Tl^+-ion is a slow scintillation process, whereas the primary light production is fast. At higher ionisation densities the secondary scintillation process becomes more important. This property makes it possible to do particle identification. The ionisation density in the crystal is dependent on the type of particle travelling through the medium. The crystals are read out by an integrating amplifier. Using the rise time of the integrated light output it is possible to distinguish between the different scintillation processes and consequently between the different particle species [35].

2.1.2 The central trigger detector

The primary part of the detector array is the central trigger detector (CTD). The CTD covers the region between 11° and 78° in polar angle. For the reactions under investigation in this thesis, this is approximately the mid-rapidity area. In this region particles created by multifragmentation processes are emitted. High multiplicities and

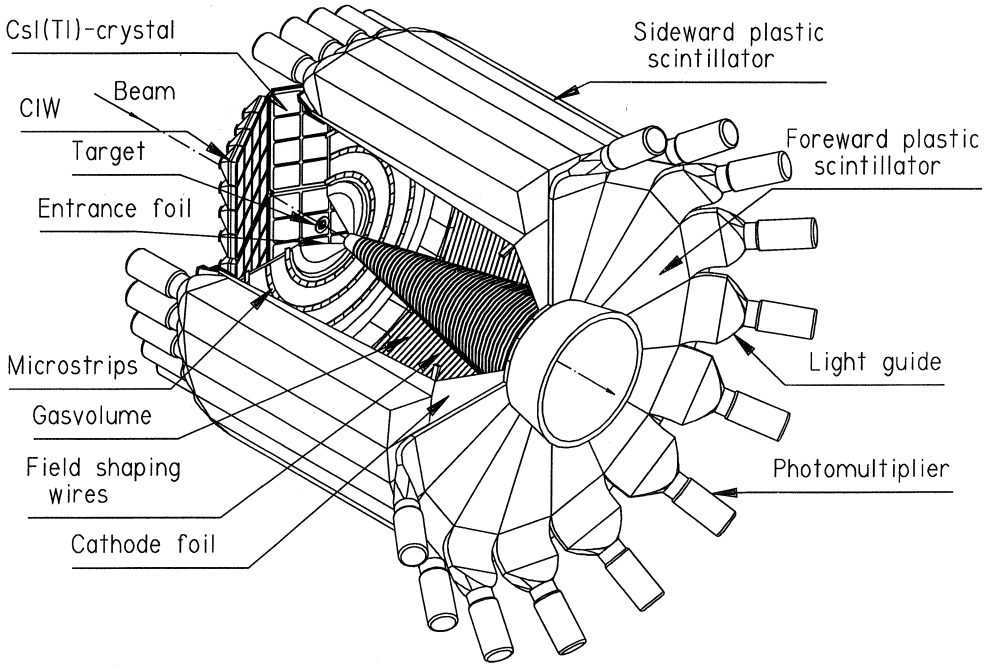

Figure 2.3: *Detailed view of the central trigger detector with the CIW.*

a large Z-range are expected. The kinetic energies can be very low, particularly in the transverse direction. In the mid-rapidity region also many light particles from the overlap region in the nuclear collision will be emitted. Therefore, it is necessary to have low energy thresholds and a large Z coverage. Furthermore a good spatial resolution is required. To meet these requirement the CTD was designed to be a time projection chamber (TPC) with microstrip read-out, backed by 48 scintillator plastics. The gas chamber combines a low energy threshold with good spatial resolution. Particle identification is achieved using the energy loss in the gas and the total energy measured in the plastic scintillators.

Fig. 2.3 shows the CTD with the CIW. The plastic scintillators stop the mid-rapidity particles, more energetic particles in the forward region will be identified with the MUR (see section 2.1.3). Particles travelling through the chamber will liberate electrons in the gas. Under the influence of a 5 kV electric field these electrons drift towards the microstrips, which record their drift times and signal amplitudes. The drift time is used to determine the angle of the track. The amplitude is proportional to the energy deposition in the gas and is used in conjunction with the plastic scintillator signal to

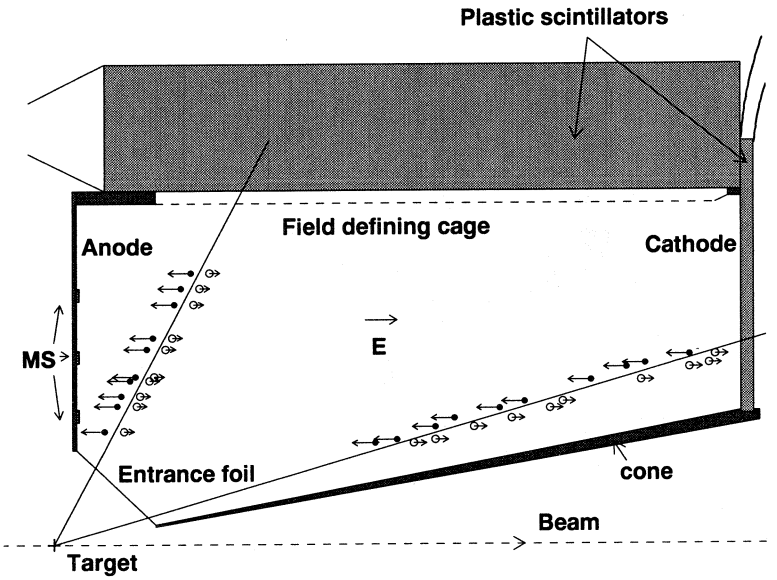

Figure 2.4: *Schematic cut-through of the CTD. The volume defined by the sideward plastics at 28 cm from the beam pipe, the forward plastics at 54 cm from the target, the anode plate, the cone at 11° and the entrance foil contains the drift gas. Particles enter the chamber through the entrance foil. Electrons and holes are created along a particle trajectory. The electrons drift towards the microstrips which measures the drift time and amplitude of the signal.*

achieve particle identification.

Microstrips and drift gas

Fig. 2.4 shows a schematic cut-through picture of the CTD. The sideward plastic scintillators have a distance of 28 cm to beam. The forward plastics are located 54 cm from the target. The volume defined by the plastics, the anode plate, the cone at 11° and the entrance foil contains the drift gas. The gas is contained in the chamber by a 24 μm mylar foil in front of the sideward plastics, and an aluminium coated 24 μm mylar foil (the cathode foil) in front of the forward plastics. Particles created in the heavy-ion collision enter the chamber through the 36 μm thick entrance foil (mylar). While passing through the gas volume they create electron-ion pairs. A 5 kV drift field is defined by thin wires close to the plastic scintillators and on the cone. The electrons drift to the anode where a certain fraction is collected by the microstrips. The microstrips measure a signal amplitude from which the $\mathrm{d}E/\mathrm{d}x$ in the gas can be calculated. The $\mathrm{d}E/\mathrm{d}x$ is used in conjunction with the total energy measured in the

plastics to achieve particle identification (see section 3.2). The drift time of the electrons can be used to calculate the angle of the particle (also see section 3.2). The TPC detects particles emitted between 11° and 78° in polar angle. Insensitive areas are a 1° support structure between 27° and 28° polar angle and several support structures of 0.5° every 45° and of 1° every 90° in azimuthal angle.

The signal of the electrons in the gas is very weak. A large amplification is necessary to achieve a significant signal. Microstrip gas counters (MSGCs) do this without disturbing the TPC drift field. MSGCs have found extensive use in nuclear and high energy physics since their introduction by Oed in 1988 [39]. A microstrip detector consists of an alternating pattern of parallel anode and cathode strips on a substrate. The width of the strips is of the order of microns , the length is typically several centimeters. The mechanical properties of such a structure are very stable. Through a voltage difference between the anodes and cathodes a strong electrical dipole field is obtained, which extends only a few hundred micrometer from the substrate. This allows for the use of microstrip counters in conjunction with a time projection chamber. The MSGC is capable of handling high count rates with excellent position resolution. The detection limit is strongly dependent on the number of primary electrons and on the gas amplification. A large number of primary electrons can be achieved by operating under high pressure. This, however, has a negative effect on the gain. Furthermore, in the Huygens detectors a high pressure in the gas chamber would constitute a high threshold for the particles to reach the plastic scintillators. This makes it necessary to operate the gas chamber in the low pressure region (< 1 bar). Because the number of primary electrons is inversely proportional to the pressure, a high gain for the MSGCs is necessary in this region.

In fig. 2.5 a microstrip used in the Huygens set-up is shown. The aluminium structure (black in fig. 2.5) is deposited on a 600 μm thick glass substrate (Desag D263). The MSGC consists of 50 anodes, which are connected in parallel. The 50 cathodes are also mutually connected. The anode is approximately 10 μm wide, separated by 50 μm from a 90 μm wide cathode (detail in top-right corner). The MSGC has an effective width of 10 mm and is approximately 22 mm long. Fig. 2.6 shows the calculated field lines of a microstrip in an area of 500 μm over the microstrip to 500 μm in the substrate. The calculations were performed with both the microstrip dipole field and the drift field. Close to the microstrip, where the field lines are dense, i.e. the electric field is strong, the amplification occurs. This figure shows the compatibility of the microstrip with the TPC: the amplification area extends no more than 200 μm over the microstrip, at a larger distance from the microstrip only the drift field is present. The microstrips have a trapezoidal shape, so they can be arranged in a circular pattern without introducing dead areas. Three rings of microstrips are located at approximately 90° polar angle, perpendicular to the beam. For each ring the angle of the trapezoid is slightly different. The first microstrip ring is located 100 mm (radially) from the target and contains 28 microstrips. The second ring holds 44 microstrips and has a distance of 145 mm from the target. Finally at 197 mm the third ring has 56 microstrips. The microstrips are read out by an integrating preamplifier (Vitrohm 559-064), with a noise of approxi-

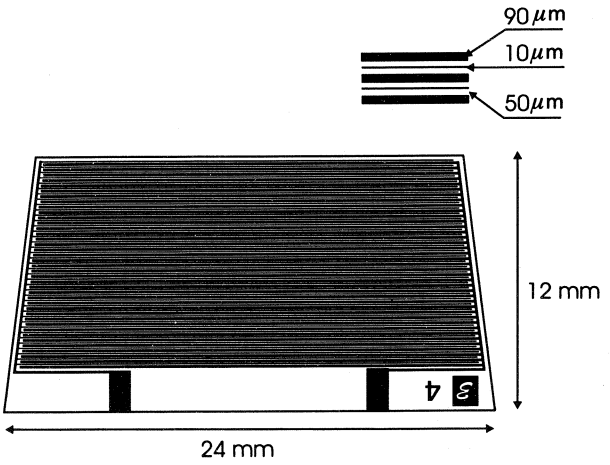

Figure 2.5: *Microstrip gas counter as used in the third ring. The top-right shows in detail the anode-cathode spacing.*

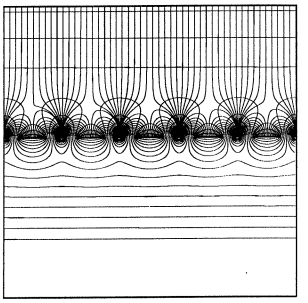

Figure 2.6: *Field lines close to the microstrip surface*

mately 2000 electrons [40]. The amplitude measured in the first ring is used for particle identification. Microstrips from this ring are read out by two main amplifiers each, one with a high gain and one with a low gain. Thus a high dynamical range for particle identification is obtained. For the second ring one main amplifier per microstrip is used and MSGCs in the third ring are coupled in pairs to a main amplifier. The response of the preamplifier is strongly dependent on the width of the incoming signal. Charge collected over a time interval of 200 ns will be identified with an amplitude 3 times higher than the same charge collected over 600 ns. During the previous experiment [41] isobutane was used in the drift chamber. Although this gas shows a large gain it has a very low drift velocity, which results in a large collection time for the liberated charge. This effect is especially important at small angles where the liberated charge over the microstrip has a large spatial distribution.

Extensive research was done in order to find the best drift gas for the TPC. Section 2.2 describes these efforts. During the experiment described in this thesis CF_4 was used in the TPC at 150 mbar. The drift field was kept at 5 kV, resulting in a drift velocity of 8.9 cm/μs. The bias voltage over the microstrips was 400 V. This gives a detection limit for protons of 25 AMeV and for α-particles of 125 AMeV.

Plastic scintillators

The TPC is backed by 48 plastic scintillators: 32 sideward plastics and 16 forward plastics. The scintillators are made of NE102a material. The sideward plastic scintillators are approximately 50 cm long and 10 cm thick, they have an approximate

width of 5 cm, but have a trapezoidal shape so that when the 32 are placed side by side they form a cylindrical volume with an inner radius of 28 cm. In fig. 2.3 some of the sideward plastics are removed to reveal the gas chamber. The plastics are optically isolated on three sides by teflon foil. The fourth side faces the chamber and is covered by a 2 μm germanium-coated mylar foil, completing the optical isolation. This specially developed foil [42] has a low conductivity which makes it possible to use it in conjunction with the high electric drift field (100 V/cm). Furthermore, the thin foil has a low threshold for ionising particles. At approximately 85° polar angle the scintillators are connected by a light guide to a photo-multiplier (Thorn/EMI 9266B). The photo-multipliers are operated at approximately 900 V. The sideward plastics are used as a calorimeter, the energy deposited in the plastic is used in conjunction with the energy loss in the gas to do particle identification. At 50° polar angle the intrinsic threshold for protons is 5.6 AMeV, for boron it is 8.5 AMeV.
The forward plastics are also shown in fig. 2.3. These wedge-shaped plastics are approximately 25 cm long and 1 cm thick, they are between 4 and 14 cm wide. The scintillator is wrapped in 1 mm thick teflon to ensure optical isolation. At approximately 35 cm perpendicular to the beam direction the plastic is connected to a photo-multiplier (Thorn/EMI 9266B) by a curved light guide. The photo-multipliers of the forward plastics are operated at approximately 800 V. Signals from particles that are stopped in the forward plastics are treated the same as signals from the sideward plastics. Punch-through particles are also detected in the MUR. The signal from the forward plastics is then used in conjunction with the timing signal from the MUR to achieve particle identification. The energy is calculated with the time measurement in the MUR. At 15° polar angle the intrinsic threshold for protons is 4.1 AMeV, for boron it is 6.1 AMeV.
Because the photo-multipliers are sensitive to temperature variations, they are continuously monitored. A nitrogen laser emits pulses of 337 nm at approximately 1 Hz into a diffusor. The diffusor is coupled by quartz fibres (QSF600W) to the plastic scintillators and to a Si-photo-diode (Hammamatsu S1790-04). The photo-diode is used to monitor the laser intensity and to trigger the read-out of the laser events (see section 2.3.2).

2.1.3 The MUR

In fig 2.1 the MUR is shown in conjunction with the Huygens detectors. The MUR is a time-of-flight wall covering 3° to 30° polar angle at 2.1 m from the target [32]. It consists of 96 sheets of 2 mm thick NE102a plastic scintillator material. The sheets are arranged in seven concentric rings, the first two consist of eight sheets with an azimuthal resolution of 45°, the other five rings consist of sixteen sheets with an azimuthal resolution of 22.5°. A curved light guide is mounted on the edge of each sheet. The light guide is connected to a photo-multiplier (RTC 2262B) which is located at the exterior of the vacuum chamber. The other three sides of the scintillator are painted to improve the uniformity of the signal. To ensure optical isolation a 18 μm aluminium foil covers the sheet. The inner three rings are covered by an additional 50 μm thick aluminium foil to filter out low energy electrons from the target. The remaining rings are shielded by the TPC.

Particles with polar angles between 3° and 10° are only identified in the MUR. The time-of-flight information in conjunction with the energy loss in the sheet can be used to achieve particle identification. From the time of flight the energy is calculated. This procedure is only possible if the particles are not stopped in the sheet, yielding an energy threshold at 6° for protons of 14 AMeV and for boron of 23 AMeV. Between 11° and 27° polar angle particles have to pass through the TPC before they can reach the MUR. Therefore, only particles with energies higher than approximately 36 AMeV are identified in the MUR. These particles can be identified in the same way as particles identified with the lower MUR modules, however, combining the time-of-flight signal with the energy-loss signal from the forward plastics yields a much better result (see section 3.2).

2.2 Upgrade of the TPC

In the previous Huygens experiment it was found that the TPC was not able to detect protons and that the detection of α-particles was limited to those with a kinetic energy less than 25 AMeV [41]. For the 1996 experiment an upgrade of the detector was proposed to enhance the coverage to the complete $Z = 2$ energy range, i.e. at least to 100 AMeV. The acceptance of the microstrips can be improved, either by increasing the gain of the microstrip, or by the creation of more primary electrons in the gas chamber. The gain can be changed using the bias voltage over the strips. This increases the gain exponentially. However, increasing the voltage is only possible until the voltage itself starts creating electron avalanches over the microstrip. The microstrips have to be operated well below this breakdown voltage. Furthermore increasing the gain does not reduce noise originating from within the chamber. The number of primary electrons is linearly proportional to the energy loss in the gas. By increasing the gas pressure, more electrons will be liberated. However, an increase in the pressure leads to a decrease in the drift velocity, which is unacceptable with respect to the preamplifier of the microstrip. In order to find the optimal drift gas for the Huygens detectors several drift gases were investigated, both experimentally and with computer simulations.

2.2.1 Computer simulations of the MSGC

The software discussed in this section was developed at the Utrecht University department of Computational Physics for the simulation of MSGC-like detectors. The development and implementation were done by Dr. E.H. Agterhuis [43, 44, 45]. The software consists of two parts. The first part deals with the computation of the electric field in the detector. The second part simulates the behaviour of free electrons in the detection gas.

To calculate the electric field the device is defined in terms of standard building blocks, which can be either rectangular or elliptical. The output is a description of the electrostatic potential and the electric field in terms of values at a discrete set of positions, which are situated at the vertices of a rectangular regular grid. The computation is performed in two dimensions, which imposes the restriction that only structures with

a geometry which does not change along at least one axis can be used. This is the case for most MSGC-like detectors. In this case the computational domain, i.e. the area for which the field was actually computed, was taken in a plane perpendicular to the cathode and anode strips, thus exploiting the fact that the MSGC geometry does not change in this direction. Although at the very ends of the strips fringe effects are present, which can only be simulated with a three-dimensional field computation, the two-dimensional computation is correct for the main part of the MSGC. The computational domain did not cover the entire width of the MSGC; only one anode strip and one cathode strip were taken into account. Periodic boundary conditions were applied to simulate the repetition of the strip pattern along the horizontal axis.

The simulation of the behaviour of free electrons is based on a semi-stochastical model. Collisions between the electrons and the gas molecules are treated in a stochastical manner. The trajectories of the electrons between collisions are computed in a deterministic way. The probability that an electron suffers a collision with a gas molecule between time t and $t + \mathrm{d}t$ is given by:

$$P = w_{\mathrm{c}}\, \mathrm{d}t, \tag{2.1}$$

with w_{c} the collision probability per unit time, or the 'collision rate'. To calculate the time interval between two subsequent collisions, eq. 2.1 is used to find the probability P_{S} that an electron survives a time $t + \mathrm{d}t$ without suffering a collision. This quantity is given by the probability that the electron does not collide during a time t, multiplied by the probability that there is also no collision in the interval $[t, t + \mathrm{d}t]$. Using eq 2.1 this yields:

$$P_{\mathrm{S}}\left(t + \mathrm{d}t\right) = P_{\mathrm{S}}\left(t\right)\left(1 - w_{\mathrm{c}}\, \mathrm{d}t\right). \tag{2.2}$$

With the definition:

$$P_{S}\left(t + \mathrm{d}t\right) = P_{\mathrm{S}}\left(t\right) + \frac{\mathrm{d}P_{\mathrm{S}}}{\mathrm{d}t}\, \mathrm{d}t, \tag{2.3}$$

and eq. 2.2, the following differential equation is obtained:

$$\frac{1}{P_{\mathrm{S}}} \frac{\mathrm{d}P_{\mathrm{S}}}{\mathrm{d}t} = -w_{\mathrm{c}}\,. \tag{2.4}$$

It is assumed that w_{c} only depends on time via the time-dependent momentum of the particle through the relation:

$$w_{\mathrm{c}}\left(p\right) = \sigma\left(p\right) \eta \frac{p}{m_{\mathrm{e}}}, \tag{2.5}$$

where $\sigma\left(p\right)$ is the total scattering cross section, η the density of the gas, p the momentum of the electron and m_{e} its mass. The general solution of eq. 2.4 is given by:

$$P_{\mathrm{S}}\left(t\right) = \alpha \exp\left[-\int_{t_0}^{t} w_{\mathrm{c}}\left(p\left(t'\right)\right)\, \mathrm{d}t'\right]. \tag{2.6}$$

The starting time t_0 is defined to be the moment of the last encountered collision, so that $P_S(0) = 1$ and thus $\alpha = 1$. The probability, $P_c(t)dt$, for a particle not to collide during a time t and subsequently encounter a collision in the interval $[t, t + dt]$ is then given by the product $w_c P_S(t)\ dt$:

$$P_c(t) = P_c \exp\left[-\int_0^t w_c(p(t'))\ dt'\right]. \tag{2.7}$$

During a simulation, random numbers are drawn from the distribution defined by eq. 2.7 to find the intervals between the collisions. To calculate this probability the momentum of the electron between collisions has to be known. The momentum is calculated by solving its equation of motion with a method known as Verlet's algorithm [46]. This not only yields the electron's momentum but also its trajectory.
A stochastic method is used to determine what type of collision takes place. Each possible process has its own momentum dependent collision rate, $w_c^i(p)$, the sum of these rates being the total collision rate $w_c(p)$. The probability for a certain type of event to occur, $P_c^i(p)$, is equal to the ratio between the individual collision rate and the total collision rate:

$$P_c^i(p) = \frac{w_c^i(p)}{w_c(p)}. \tag{2.8}$$

For the present study three different types of processes were taken into account: elastic scattering, inelastic scattering and ionisation. The collision probabilities were derived from cross-section data, which were kindly placed at our disposal by Dr. S. Biagi [44, 47]. Each process is characterised by a specific loss of kinetic energy of the electron. Processes involving ionisation also lead to the production of new free electrons, which subsequently take part in the simulation. It is assumed that the scattering processes are all isotropic, i.e. after each encounter with a gas molecule an electron is given a random direction from a distribution which assigns equal probabilities to all possible orientations [48].
It is important to note that the simulation of the motion of the electrons is performed in three dimensions, in contrast to the computation of the electric field. When, during the solution of the equations of motion, the electric-field strength at a certain position must be evaluated, the coordinate along the direction of the strips is simply ignored. As explained before, the electric-field values are given at a discrete set of positions only. The evaluation of the force acting on an electron is performed by taking the value of the field strength at a discrete position nearest to the actual position and multiplying it by the charge of the electron.
To study the gain of the detector the evolution of single-electron avalanches, resulting from a predefined ensemble of primary electrons were simulated. The simulations were performed for the same set of bias voltages and pressures used in the experiment. The starting positions of the primary electrons were chosen at a distance of 900 μm from the substrate. To eliminate dependencies on the horizontal coordinate, four different starting positions were used, each 50 μm apart. For each data point 200 single electron avalanches were simulated; 50 for each of the four starting positions.

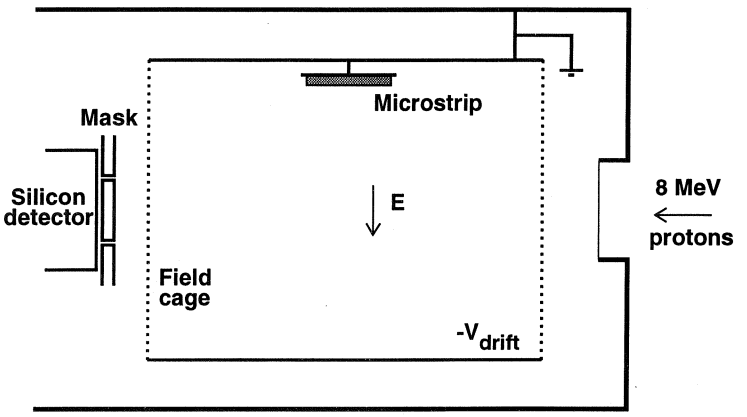

Figure 2.7: *Schematic overview of the test set-up. A field defining cage is placed within a grounded box. The voltage over this cage can be varied. A silicon detector is located behind a mask containing two slits. The distance between the slits is 12.7 ± 0.5 mm. The top slit is located approximately 10 mm vertically from the microstrip. The 8 MeV protons move parallel to the microstrip.*

2.2.2 Experimental MSGC test set-up

The drift gas properties of several drift gases were investigated using the test set-up shown in fig. 2.7. A microstrip is placed within the small chamber. The hardware used for the readout is the same as used in the Huygens detectors and is described in section 2.3.1. The trigger signal for the readout is provided by a silicon detector, which is situated behind the effective area of the microstrip. The silicon detector has a two slit entrance, parallel to the MSGC, with a slit spacing of 12.7 ± 0.5 mm. The Utrecht Van de Graaff tandem accelerator provided 8 MeV protons, which were elastically scattered off a thin gold target. The scattered protons pass parallel to the microstrip surface at a distance of 1 to 2 cm with a direction perpendicular to the anodes and cathodes. A drift field is provided by a field defining cage with dimensions $5 \times 6 \times 9$ cm^3 and a wire spacing of 2.5 mm. The time difference between electrons originating from particles passing through the different slits is used to determine the drift velocity in the counting gas. In order to gauge the amplification of the read-out system, the microstrip was taken out of the set-up and a known charge was injected into the circuit with similar time characteristics as a pulse from the microstrip. This output signal was used to determine the gain of the combined response of the preamplifier, the fast main amplifier and the flash ADC (see section 2.3.1).

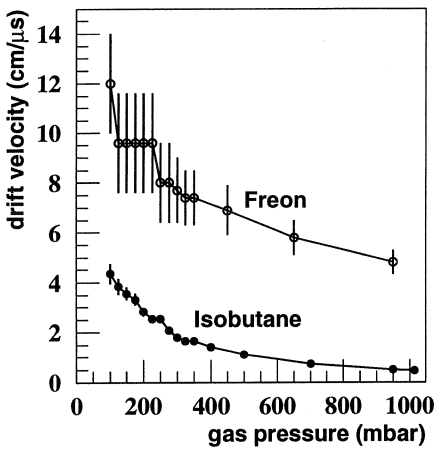

Figure 2.8: *Drift velocity as a function of pressure for a drift field of 200 V/cm for CF_4 and isobutane.*

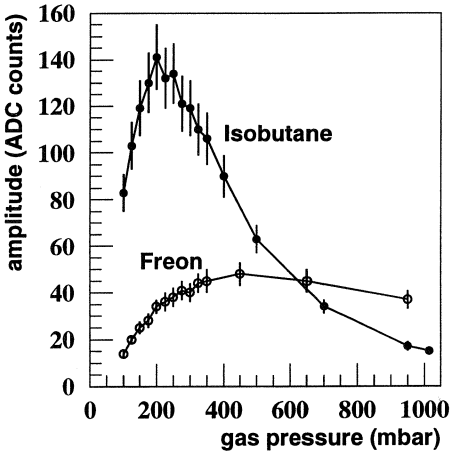

Figure 2.9: *Microstrip signal amplitude as a function of pressure for a bias voltage of 384 V.*

2.2.3 Experimental and simulation results

Several gases and different mixtures of gases were tested with the Huygens microstrips. Because the gain depends exponentially on the bias voltage, the breakdown voltage, which limits the gain, should be measured first. It was found that isobutane has a breakdown voltage of approximately 510 V at 300 mbar. For freon (CF_4) this value is 530 V. Mixtures of CF_4 with argon, isobutane with CF_4 and argon, and isobutane with argon, all showed breakdown voltages below 350 V. The latter are, therefore, rejected because the microstrip gain is limited. Further investigations were concentrated on the properties of CF_4 and isobutane.

Firstly the drift velocity in the counting gas was measured as a function of pressure. The electric field was kept constant at 200 V/cm Fig. 2.8 shows the results of these measurements. The maximum drift velocity was measured in CF_4 at the minimum pressure of 100 mbar: $v_d = 11 \pm 2$ cm/μs for a reduced field of $E/p = 2.0 \pm 0.1$ Vcm^{-1}mbar^{-1}. At the same reduced field the value of the drift velocity in isobutane is: $v_d = 4.2 \pm 0.2$ cm/μs. These results are in good agreement with literature [49, 50], even though we measured at very different settings to achieve the same reduced field. The simulations were able to reproduce these values within an accuracy of 10%. The measurements show that an increase in pressure decreases the drift velocity in the counting gas.

Secondly the signal amplitude and the gain of the MSGC at different gas pressures were investigated. For the major part of the measurements the drift field was kept constant at 200 V/cm and the anode voltage at 384 V while the pressure was varied

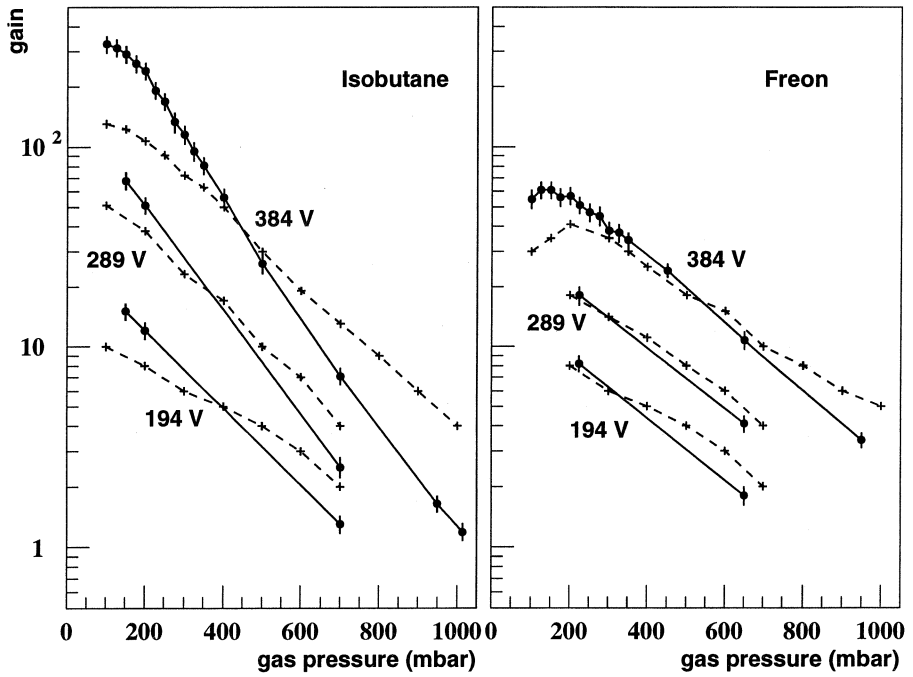

Figure 2.10: *Gain as a function of pressure for isobutane and CF_4. The voltages shown in the graph are the applied bias voltages over the microstrip. The lines serve to guide the eye. Data points connected with straight lines are experimental, the dashed lines connect the simulated gain.*

between 100 and 1015 mbar. The results of these measurements are shown in fig. 2.9. Note that isobutane has a sharp maximum at approximately 200 mbar. CF_4 does not show a pronounced maximum in the detected signal within our pressure range. At several pressures the gain of the MSGC was measured at different bias voltages. In fig. 2.10 the actual gain (number of detected electrons divided by the number of primary electrons) for the measurements with isobutane is shown on the left-hand side and with CF_4 on the right-hand side. Both graphs also show the simulated data. The graphs show that the pressure has a negative influence on the gain of the MSGC. Note that the gain at high pressure in isobutane becomes less than the gain in CF_4. In the graphs also the results for different bias voltages are shown. These data indicate that the slope of the curves is largely independent on the bias voltage. All the simulated data show essentially the same dependence of the gain on pressure as was found in the experiment. The curves for isobutane are somewhat less steep than the experimental curves, but the general agreement is good. The simulation results for CF_4 are in good agreement with the experimental data. Like the experiment, the simulations show a flattening of the curves and eventually a drop in gain for pressures below 200 mbar.

This effect is most prominent for CF_4 and also occurs at a somewhat higher pressure than for isobutane.
The graphs can be understood by investigating the ionisation probability. This probability is proportional to the ionisation cross section and the gas pressure (eq. 2.5). The cross section for ionisation is a rising function of the electron energy above a certain threshold value. The mean energy of the electron decreases with pressure due to an increase in the number of energy reducing collisions. Therefore the ionisation cross section decreases. On the other hand the number of possible collision partners increases proportionally with the pressure. From the data we can conclude that the decrease in gain with pressure must be the result of a fast decrease of the ionisation cross section. The flattening of the graphs at low pressure indicates a levelling off of this cross section. The measured difference in the slope for the two gases is directly related to the different momentum-dependent collision cross sections of the two gases. This is confirmed by the simulations which also show a slope difference.
For both gases, the measured curves show a steeper slope than the simulated curves. This effect can be attributed to the accuracy with which the electric field can be reproduced in the region close to the surface of the microstrip. Simulations show that small changes in the electric field configuration have a strong influence on the slope of the graphs [44].

2.2.4 Discussion and conclusion

The main goal of the investigation into the properties of the different gases was to choose the optimal drift gas for the Huygens detectors. In earlier experiments the microstrips were not able to measure α-particles [41]. To improve on this, it is necessary to increase the signal in the chamber. This can be achieved by increasing the gas pressure. Fig. 2.8 shows that an increase in pressure yields a decrease in drift velocity. Because the preamplifier has a large dependence on the signal width, this is an important feature. For isobutane the drift velocity was already quite low at 60 mbar, approximately 4.4 cm/μs in the previous Huygens experiment (in agreement with fig. 2.8). This could be compensated by increasing the drift field. However, tests with the TPC showed that it was impossible to increase the drift field over 10 kV, which would merely compensate the drift velocity for an increase in pressure by a factor of two. For CF_4 the drift velocity is high, this in itself causes higher signals in the chamber (per unit time). The mechanical stability of the gas chamber limits the gas pressure to 150 mbar. Because the breakdown voltage increases with pressure, it possible to operate the microstrips under a higher bias voltage. It was concluded that the optimal settings for the TPC were to use CF_4, a drift field of 100 V/cm and a bias voltage of 400 V. Fig. 2.10 shows the measured gain for isobutane and CF_4. From this figure an estimate can be made for the gain of isobutane at 60 mbar with a bias voltage over the microstrip of 260 V and for CF_4 at 150 mbar with 400 V bias voltage. According to this estimate, both settings yield approximately the same gain. Because the pressure is increased by a factor of 2.5 and the drift velocity is increased by a factor of 2 (see fig. 2.8), the upper limit for the detection of $Z = 2$ is expected to be raised by a factor of 5, to 125 AMeV.

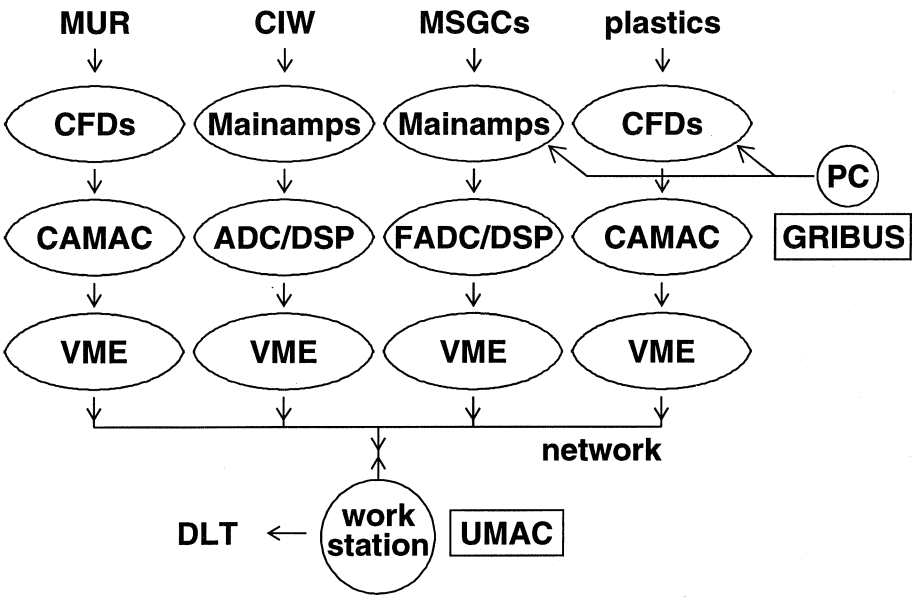

Figure 2.11: *Schematic representation of the data flow (see text).*

This would enable us to identify all α-particles. The drift velocity measured during the experiment was 8.9 ± 0.1 cm/μs, which is in good agreement with fig. 2.8.

2.3 Electronics and software

For the read-out of the different modules of the Huygens detectors many channels of sophisticated electronics are needed. The electronics was designed and built at the department of subatomic physics at Utrecht University [51]. The general research instruments bus (GRIBUS) was developed for the control of the electronics' settings, such as gain and threshold levels [51]. For the data acquisition and run control the Utrecht measurement and control (UMAC) program [52] was used on a switched ethernet with an ATM uplink to an alpha workstation with storage [53]. The data acquisition is enabled by a multiplicity trigger incorporated in the hardware. Fig. 2.11 shows a schematic representation of the data flow between the hardware modules. In this section the different modules represented in this figure are discussed.

2.3.1 Hardware modules

The electronics for each subdetector of the Huygens array were especially designed for the different modules. They were optimised for signal type and the number of channels

from the modules. Therefore, the crates are not standardised, although several are connected to the GRIBUS control system.

GRIBUS

The settings of several of the hardware modules described below are controlled by a special purpose bus called GRIBUS (general instruments research bus) [51]. The GRIBUS backplane includes sixteen data lines, eight address lines for use in the modules, six control lines and eight power lines. Each module has a an identification code from which it is recognised by the host computer. The connection between the modules and the host computer is via a standard RS232 link. Because of the noise generated by computer power supplies, the whole RS232 connection is electrically isolated from the data flow. The data exchange is completely in ASCII format, making it possible for any computer to control the GRIBUS. During the experiment the host computer was a standard PC. For easy access, the GRIBUS computer interface is completely menu driven. The parameter settings can be changed per channel, per group of channels or all channels together. To reduce set-up errors, all values are displayed in the correct units (i.e. volts, seconds, etc.). The settings can be viewed directly for monitoring purposes and can be stored on disk.

The CIW

The signals from the preamplifiers of the CsI(Tl) crystals are led to a main amplifier which has a gain of 50. The analogue signals are subsequently digitised by two 8-bit analogue-to-digital converters (ADCs). One of the ADCs converts the full range of the analogue signal. The other is set to a resolution four times better than the first, resulting in a cut-off of the signal at 25% of the full scale. Both ADCs are read out, during the calibration the two 8-bit signals can be combined to one pseudo-10-bit signal. The ADCs are processed by a ADSP2101 digital signal processor (DSP) to extract several parameters for the on-line monitoring of the CIW. The full signal from the ADCs and the calculated values from the DSP are then sent to a VME-crate which is connected to the ATM network. The VME-bus is controlled by a board with a 68030 CPU.

The MSGCs

Both the amplitude and the timing information from the TPC signals are essential for particle identification. Because the microstrips have a multiple-hit capacity, it is important that the main amplifiers have a fast shaping time. To achieve this, fast main amplifiers were developed, which have a shaping time of 50 ns [51]. The gains of these amplifiers can be set via GRIBUS between 20 and 500 in 255 steps. Each channel is then processed by a flash ADC (FADC) with a DSP (ADSP2105) [54]. For the microstrip signals the DSP plays an essential role. Contrary to the CIW signals, it is not possible to store all 128 complete MSGC signals. The DSP processes the signals extracting the timing information and the amplitude of each pulse. Also the pulse width and the integral are extracted. The DSP can identify up to 10 pulses per MSGC. The data

acquisition is started by an external trigger and runs for a predetermined number of samples. The integrated time of the samples should be longer than the maximum drift time in the gas (i.e. maximum drift distance × drift velocity). The VME-crate for the MSGC electronics is also controlled by a 68030 microprocessor.

The plastic scintillators

The signals from the plastic scintillator modules are identified by constant fraction discriminators (CFDs) [55]. The crate containing the 24 dual CFDs also has a GRIBUS module and a trigger module [51]. In the dual CFD the threshold, zero-crossing level, input buffer offset level and output blocking pulse width are all controlled by GRIBUS. Three output signals are generated in the CFD. The first is a logical signal, indicating whether or not a hit was registered in a module and is led directly to the trigger module. There it is decided whether a trigger signal is to be generated (see section 2.3.2). The second signal holds the timing information, it is led through a delay cable to a CAMAC TDC module (LeCroy 2228A). The TDC is started by a signal from the trigger module, the CFD signal provides the stop. The third signal is simply the input signal, it is led via a delay cable to a CAMAC ADC module (LeCroy 2249A). This ADC integrates the incoming signal over 90 ns from the time a trigger is generated. The data is further processed via a VME bus controlled by a 68030 processor.

The MUR

The negative signal from the photo-multiplier of each MUR module is split by a resistive splitter. One signal is delayed and integrated by a LeCroy 2249W charge to digital converter. The second signal is the timing signal. It is delayed and led to a CFD, which generates the stop for a time to analogue converter (TAC). The TAC is started by a signal from the trigger module (see section 2.3.2). The timing signal from the TAC is digitised by LeCroy 4300 ADCs. The ADC is connected to a standard VME-bus with a 68030 processor.

2.3.2 The trigger

The trigger of the Huygens detector array is based on the number of hits in the forward and sideward plastics. The particle multiplicity is generally regarded as a measure of the impact parameter of the colliding nuclei (see section 5.1). Thus with different trigger settings an impact-parameter range is selected. The trigger electronics is located in the CFD crate of the CTD. The multiplicity in the forward and sideward plastics can both be set manually between one and four. The trigger is a logical .OR. between the multiplicity in the two groups of plastics.
From the cyclotron phase, a beam pulse is deduced which has a fixed relation with the time of an event. If the multiplicity requirement is met, this signal is taken as the 'start' of the data acquisition. While an event is processed by the different units, each unit generates a busy signal, which inhibits the generation of a new trigger.
During data taking, the photo-multipliers are monitored by the injection of a laser pulse (see section 2.1.2), because this (usually) does not coincide with a cyclotron pulse, an

additional signal is generated by the laser as a substitute for the beam pulse. These laser events occur at approximately 1 Hz.
The trigger can also be run in singles mode. Then no beam pulse is necessary and the 'start' is the time of the first signal from a plastic. In this mode cosmic radiation can be measured, which is used for the calibration of the sideward plastic scintillators.

2.3.3 Data acquisition

The data flow from the VME crates is controlled by the Utrecht measurement and control program (UMAC) [52]. UMAC runs on a UNIX workstation and controls the start and the stop of the data taking in the VME environment. Because of the large amount of data, ATM (asynchronous transfer mode) technology and LANE (local area network emulation) were for the first time applied in an existing data acquisition system [53]. Ethernet to ATM bridges and ATM switches were used in the set-up to improve the data rate with a factor of five to the previously used shared ethernet solution. The LANE has the advantage of shielding the ATM layer details from the protocol stacks on top. This makes it possible to use the VME software without modifications and it still achieves the high transfer rate of ATM. Each of the four VME crates was individually linked by a 10 Mbit/s ethernet line to a ethernet to ATM bridge/switch (LS2700). The full ATM bandwidth (155 Mbit/s) was used to connect the bridge via a ATM switch (3Com cellplex 7000) to the workstation (DEC Alpha 3000-400). This resulted in a bottleneck-free connection between the VME crates and the host computer. The data taking was only limited by the detector and electronics' properties and the DLT unit (11 Mbit/s). In test mode the data acquisition system was able to process a data flow of 30.4 Mbit/s. For data taking a much lower data rate was sufficient, at maximum 2 Mbit/s. UMAC combines the data from the different modules (event building) and stores the events on tape (DLT) for later analysis. While running with an event rate of 300 events/s, UMAC can process up to 1400 one-dimensional histograms and 300 two-dimensional histograms for on-line monitoring of the detector modules.

2.4 Beam and target

This section elaborates on the two basic elements of the experiment, the beam and the target. The heavy-ion beam beam consisted of $^{24}Mg^{12+}$ ions, the target was a 92 $\mu g/cm^2$ aluminium foil.

Beam

The experiments described in this thesis were performed at the GANIL (Grand Accélérateur National d'Ions Lourds) accelerator facility in Caen (France). This facility can produce heavy-ion beams of ions with masses between 12 and 238 amu with energies between 4 and 95 AMeV, depending on the ion. The GANIL accelerator equipment consists of two cyclotrons, the first injecting its output in the second. The first cyclotron accelerates the ions to an energy between 4 and 13 AMeV, at this point the ions can also be injected into the experimental areas. After the beam is accelerated it is led

through a splitting magnet, which directs the beam through a small diaphragm. This eliminates any residual contaminations of other ion species. Because the acceleration is performed by the cyclotrons, the beam is pulsed with a frequency between 7 and 13 MHz. The intensity of the beam can be regulated at the source and by using the the diaphragm behind the splitting magnet.

The beams considered in this thesis consisted of fully stripped ^{24}Mg ions, with a kinetic energy of 45 and 95 AMeV. The current of both beams was below 1 nA and the FWHM of each beam pulse was approximately 500 ps.

Target

The target in the Huygens detectors is a thin metal foil with a radius of approximately 1 cm. It is placed on a target wheel which can hold up to 16 targets. The target wheel can be operated from outside the experimental area. For alignment purposes some of the target holders contain diaphragms, the others hold targets with a variety of elements and thicknesses. Different targets are used in test mode to get a high count rate to tune the electronics. During the experiment aluminium targets of different thicknesses can be used to achieve an optimal count rate. For final data taking an aluminium target was used of 92 μg/cm^2 (340 nm).

Aluminium is very easily oxidised when exposed to air. However, the oxidation layer encloses the aluminium matrix and therefore limits the oxidation rate and the maximum thickness of the oxidation layer. Because the target is a very thin foil it was argued that this layer could constitute a large atomic fraction (at%) of the foil. Oxidation of the target would cause a fraction of the measured collisions to be ^{24}Mg+^{16}O instead of ^{24}Mg+^{27}Al . This would contaminate the complete data set. Therefore, great care was taken to minimise the oxidation of the target. The targets (both the various aluminium targets and the other targets) were fabricated using vapour deposition in vacuum. After this process the targets were stored in a nitrogen environment. The targets were taken out of this environment and mounted on the detector just before the set-up was placed under vacuum. After the experiment the targets were quickly reemerged in nitrogen. With the kind assistance of Dr. D.K. Inia of the department of Atomic & Interface Physics at Utrecht University, the oxygen content of the target was determined using elastic recoil detection (ERD) [56]. For the ERD measurement a beam of ^{108}Ag with an energy of 48 MeV (0.44 AMeV) was used. This revealed an oxygen content of 2 at%, amounting to a layer of Al_2O_3 with a thickness of 1.5 nm on both sides of the foil. Therefore, the oxygen content of the target was neglected in the analysis.

3

The calibration of the Huygens detectors

The study of nuclear phenomena is inherently coupled to the use of elaborate experimental techniques. During an experiment the raw data, consisting of large amounts of integer numbers, are stored on tape. These numbers have to be processed to become physical quantities, such as energy, charge and angle of a particle. To be able to do so, it is necessary to understand and calculate the physical processes taking place after the *creation* of a particle until it is either stopped in the detector or it leaves the detector set-up. With *creation* is meant the moment in time after which the particle no longer undergoes any interaction associated with the actual (nuclear) process under investigation.
The Huygens detectors were designed to measure intermediate-mass fragments (IMFs), with atomic number, Z, between two and eight. The calibration of the Huygens detectors for these particles is discussed in this chapter.

In section 3.1 a general overview of detector physics is presented. Several approximations and parametrisations convenient for the particles and energy range measured with the Huygens detectors are elaborated on. The three subsections focus firstly on the energy loss of particles passing through a medium (subsection 3.1.1) and then on the two primary observables in an experiment; the light output of a plastic scintillator (subsection 3.1.2) and the time of flight of a particle in a medium (subsection 3.1.3).
Section 3.2 applies the framework of equations derived in section 3.1 to the Huygens detectors. The subsections each discuss one of the subdetectors; the MUR, the central trigger detector and the CsI(Tl) wall.
In the final section of this chapter, section 3.3, the detector performance is discussed.

In subsection 3.3.1 the acceptance and particle-identification properties of the different subdetectors are investigated. Subsection 3.3.2 focuses on the detector simulation. Finally in the last subsection some conclusions about the detector performance are drawn.

3.1 The passage of particles through matter

Particles travelling through a medium will dissipate their energy predominately by collisions with electrons in this medium. IMFs will, therefore, travel in most cases in a straight line. Only on very rare occasions a nuclear collision will occur. These nuclear events are not taken into account.

Work described in this section is based on work done by Snellings [41, 57] and Hulsbergen [58].

3.1.1 Energy-loss calculations

The average energy loss of a particle with atomic number Z, mass m and velocity β moving through a medium with electron density n_e is given by the well known Bethe-Bloch equation [59, 60, 61]:

$$-\frac{dT}{dx} = 2\pi a_0^2 m_e c^2 n_e \frac{Z^2}{\beta^2}\left(\ln\left(\frac{2m_e c^2\gamma^2\beta^2 W_{max}}{I^2}\right) - 2\beta^2 - \delta - 2\frac{C}{Z}\right). \quad (3.1)$$

Due to the statistical nature of the collisions, the energy loss per unit length, $-\frac{dT}{dx}$, is the average value of a Landau distribution. The electron mass is m_e, c is the speed of light and γ is the relativistic Lorentz factor. The atoms in the medium have an average ionisation potential I, and a_0 is the Bohr radius. The maximum energy transfer in a collision, W_{max}, is given by:

$$W_{max} = \frac{2m_e c^2\eta^2}{1 + 2s\sqrt{1+\eta^2} + s^2} \approx 2m_e c^2\eta^2. \quad (3.2)$$

Where $s = m_e/m$ and $\eta = \beta\gamma$. The approximation in eq. 3.2 holds for $s \ll 1$. The last two terms in eq. 3.1 are semi-empirical corrections for the medium density (δ) and for shell effects of the orbital electrons (C).

By substituting eq. 3.2 in eq. 3.1 a powerful tool is created to calculate the energy loss of a particle moving in a medium. One drawback of this equation is its inability to be integrated analytically. In the energy domain investigated, the energy loss of particles in several millimeters of material is an important fraction of the total energy of a particle. Therefore, the energy loss can not be neglected and integrating eq. 3.1 becomes important. To solve this problem a parametrisation of the Bethe-Bloch equation has been used, given by [57]:

$$-\frac{d\epsilon}{dx} = \frac{Z^2}{m}\frac{\kappa}{(\epsilon+\epsilon_0)^\mu}. \quad (3.3)$$

parameter	value	unit
μ	0.895	
ϵ_0	$0.949 \cdot 10^{-3}$	
$\kappa_{\text{plastic(NE102A)}}$	$0.178 \cdot 10^{-3}$	m_p/mm
$\kappa_{\text{aluminium}}$	$0.342 \cdot 10^{-3}$	m_p/mm
κ_{mylar}	$0.235 \cdot 10^{-3}$	m_p/mm
$\kappa_{\text{freon(150mbar)}}$	$0.772 \cdot 10^{-7}$	m_p/mm
κ_{vacuum}	0.	m_p/mm

Table 3.1: *Calibration values for stopping (see text).*

In this equation κ, μ and ϵ_0 are medium-dependent constants. The left-hand side of the equation contains the quantity ϵ, which is the kinetic energy divided by the rest mass, $\epsilon = T/mc^2$. Numerically calculated stopping values are used to fit the medium-dependent parameters. The values of μ and ϵ_0 are close to 1 and 0, respectively and are approximated to be medium independent. All material-dependent features, such as electron density, can be incorporated in the parameter κ. This gives a good approximation of the Bethe-Bloch formula within a specific energy range (for this analysis the energy range is 1 to 100 AMeV). Integrating eq. 3.3 leads to:

$$(\epsilon(x) + \epsilon_0)^{\mu+1} = (\epsilon(0) + \epsilon_0)^{\mu+1} - x\kappa\frac{Z^2}{m}. \tag{3.4}$$

The *translated* kinetic energy is defined as $\epsilon_t \equiv \epsilon + \epsilon_0$. Substituting this in eq. 3.4 leads to the energy loss in a medium of j layers with thickness d_j, given by:

$$\epsilon_{t,f}^{\mu+1} = \epsilon_{t,i}^{\mu+1} - \frac{Z^2}{m}\sum_j \kappa_j d_j. \tag{3.5}$$

The quantities $\epsilon_{t,i}$ and $\epsilon_{t,f}$ denote the initial and final energies, respectively. The third term is the summation of punch-through energies of the different layers d_j.
The parameters μ, ϵ_0 and κ_j were fitted to numerically calculated stopping values based on proton data by Ziegler *et al.* [62]. The fit was done in the energy range from 1 to 100 AMeV. The values for μ and ϵ_0 were fitted to calculations for plastic scintillator material, as this is the most abundant material in the detector. The values for κ_j were fitted to calculations of the stopping of α-particles in the different materials. The α-particles where used throughout the calibration as a gauge, as they are the most abundant IMF which is measured over the complete energy range. The fit is accurate within 1% in this energy range for $Z \leq 8$. The calibration values are listed in table 3.1

3.1.2 The light output of a plastic scintillator

In plastic scintillator detectors the ionisation process, caused by the particle travelling through the medium, involves the release of one or more photons, usually in the blue region of the spectrum. As the medium is transparent, the deposited energy can be measured by detecting the intensity of this light. However, the efficiency of this conversion process depends on the type and energy of the incident particle.
The first successful semi-empirical formula describing this dependency was published by Birks in 1951 [63]. Birks assumed a linear response of the scintillator material for the light output. Deviations were explained by a quenching interaction between molecules which are excited by the particle passing through the medium. These interactions drain energy from the system which would otherwise produce light.

A particle passing through a medium produces along its track *damaged* molecules, by the production of an *exciton*. The ratio of the damaged over the undamaged molecules is proportional to the energy loss in the medium: $P_{\text{damaged}}/P_{\text{undamaged}} = B\mathrm{d}E/\mathrm{d}x$. The number of excitons produced is also proportional to the energy loss by a factor S, the scintillation efficiency. If an exciton is captured by a damaged molecule, the energy is dissipated non-radiatively. However, if it is captured by an undamaged molecule, detectable light is produced. If the probability that an exciton is captured by a damaged molecule is k times the probability that it is captured by an undamaged molecule, the probability of a radiative emission is given by:

$$P_{\text{scintillation}} = \frac{P_{\text{undamaged}}}{P_{\text{undamaged}} + kP_{\text{damaged}}}. \tag{3.6}$$

This leads to eq. 3.7, which is known as Birks' Law, this expression gives the light output per unit length, $\frac{\mathrm{d}L}{\mathrm{d}x}$ as a function of the energy loss per unit length $\frac{\mathrm{d}E}{\mathrm{d}x}$:

$$\frac{\mathrm{d}L}{\mathrm{d}x} = S\frac{\mathrm{d}E}{\mathrm{d}x}\frac{1}{1+kB\frac{\mathrm{d}E}{\mathrm{d}x}}. \tag{3.7}$$

It should be noted that the two parameters k and B can not be determined separately. Therefore, the product kB is treated as a single adjustable parameter. By inserting eq. 3.3 in Birks' Law, an expression is obtained in which the light output of a particle in a plastic scintillator is related to its kinetic energy:

$$\frac{\mathrm{d}L}{\mathrm{d}\epsilon_t} = -\frac{Sm}{1+aZ^2\epsilon_t^{-\mu}}, \tag{3.8}$$

where

$$a = kB\frac{c^2\kappa}{\mu+1}. \tag{3.9}$$

For $\mu = 1$, this expression can be integrated to obtain an equation for the total light output L:

$$L = Sm\left(\epsilon_{t,i} - \epsilon_{t,f} - aZ^2\log\left(\frac{\epsilon_{t,i}+aZ^2}{\epsilon_{t,f}+aZ^2}\right)\right). \tag{3.10}$$

parameter	value
a	0.30(3)
ζ_a	0.79(4)
ζ_S	0.18(1)

Table 3.2: *Calibration values for light output (see text). The parameters are dimensionless.*

Although μ is not quite equal to unity a comparison of the result of eq. 3.10 with the data shows good agreement. Since the integral of eq. 3.8 with μ not equal to unity is rather awkward, eq. 3.10 has been used to calibrate the data.

The equation derived from Birks' Law and the approximation of the Bethe-Bloch equation can successfully describe the light output of ions with $Z \leq 2$ in a medium. However, Birks' Law does not hold for heavier particles, as other light producing processes will occur [34, 64]. Therefore, an *ad hoc* extension to Birks' Law was used to fit the data. For $Z > 3$, a and S in eq. 3.10 are related to a and S for $Z \leq 2$ in the following way:

$$a(Z) = a_\alpha(\frac{Z}{Z_\alpha})^{\zeta_a} \tag{3.11}$$

$$S(Z) = S_\alpha(\frac{Z}{Z_\alpha})^{\zeta_S}, \tag{3.12}$$

Where the subscript α denotes the value for this parameter for α-particles. The values for ζ_a and ζ_S were fitted to the boron line ($Z = 5$) in one of the inner modules of the MUR. This gives a good description of the data for all detected masses. The values are given in table 3.2.

3.1.3 Time of flight through a medium

Time-of-flight information of a particle can be used to determine its energy accurately. Both in our central plastics and in the MUR plastics this observable is measured. The timing information from the MUR is the most accurate energy measurement in our set-up and is used as the basis for the calibration of several other subdetectors. It is, therefore, important to be able to determine the time of flight of a particle through a medium accurately.

The time of flight of a particle is the integral of the inverse velocity over the thickness d of the medium:

$$ct = \int_0^d \frac{\mathrm{d}x}{\beta(x)}. \tag{3.13}$$

It must be noted that a particle loses energy, e.g. velocity, when travelling through this medium. Eq. 3.3 can be used to calculate the velocity for each point on the trajectory

of the particle. However, as the velocities are relativistic, the integration can not be done analytically. The relativistic relationship between β and ϵ is given by:

$$1+\epsilon = \frac{1}{\sqrt{1-\beta^2}}. \tag{3.14}$$

In order to obtain an analytical function for eq. 3.13, it will be calculated separately for very low energies and very high energies. From these two expressions an equation will be constructed which is valid over the energy range between 1 and 200 AMeV.

At very low energies it is not necessary to use the relativistic relation between β and ϵ. In this region it is sufficient to use the classical expression: $\epsilon = \frac{1}{2}\beta^2$. Because the kinetic energy is much smaller than the rest energy, $\epsilon \ll 1$ and neglecting ϵ_0, eq. 3.13 can be integrated (almost) exactly:

$$ct = \frac{1}{\beta(0)}\int_0^d \sqrt{\frac{\epsilon_t(0)}{\epsilon_t(x)}}\,\mathrm{d}x \tag{3.15}$$

$$= \frac{d}{\beta(0)}\frac{2\mu+2}{2\mu+1}\left(\frac{\epsilon_t(0)}{\epsilon_{t,pt}}\right)^{\mu+1}\left(1-\left(1-\left(\frac{\epsilon_{t,pt}}{\epsilon_t(0)}\right)^{\mu+1}\right)^{\frac{2\mu+2}{2\mu+1}}\right) \tag{3.16}$$

$$= \frac{d}{\beta(0)}\left(1+\frac{\eta}{4(\mu+1)}+O(\eta^2)\right). \tag{3.17}$$

In the second line eq. 3.3 is inserted, with $\epsilon_{t,pt}$ the punch-through energy. In the third line a Taylor expansion in $\eta = (\epsilon_{t,pt}/\epsilon_t(0))^{\mu+1}$ is performed.

At relativistic energies, it is no longer possible to neglect the kinetic energy. However, if the energy is sufficiently high, the energy loss of a particle in a medium is far less than its initial energy. Then it is possible to do a Taylor expansion in η of the integrand and perform the integration afterwards. In order to calculate $\frac{\mathrm{d}\beta^{-1}}{\mathrm{d}\eta}$, the quantity $\frac{\mathrm{d}\beta^{-1}}{\mathrm{d}\epsilon}\frac{\mathrm{d}\epsilon}{\mathrm{d}\eta}$ has been calculated. From eq. 3.14 the first term can be determined:

$$\frac{\mathrm{d}\beta^{-1}}{\mathrm{d}\epsilon} = \frac{-1}{\beta^3(1+\epsilon)^3}. \tag{3.18}$$

The second term can be found with eq. 3.3 and with the definition of η :

$$\epsilon_t(x) = \epsilon_t(0)\left(1-\eta\frac{x}{d}\right)^{\frac{1}{\mu+1}} \quad \Longrightarrow \tag{3.19}$$

$$\frac{\mathrm{d}\epsilon}{\mathrm{d}\eta} = \frac{\mathrm{d}\epsilon_t}{\mathrm{d}\eta} \tag{3.20}$$

$$= -\frac{\epsilon_t(0)}{\mu+1}\frac{x}{d}\left(1-\eta\frac{x}{d}\right)^{\frac{-\mu}{\mu+1}}. \tag{3.21}$$

Where $\beta(x) = \beta(0)$ and $\epsilon(x) = \epsilon(0)$ for $\eta = 0$. The Taylor expansion of the integrand can then be expressed as:

$$\frac{\beta(0)}{\beta(x)} = 1 + \eta\frac{1}{4(\mu+1)}\frac{2\epsilon_t(0)}{\beta(0)^2(1+\epsilon(0))^3}\frac{2x}{d} + O(\eta^2), \tag{3.22}$$

which can be integrated from 0 to d :

$$ct = \frac{d}{\beta(0)}\left(1 + \frac{\eta}{4(\mu+1)}\frac{2\epsilon_t(0)}{\beta(0)^2(1+\epsilon(0))^3} + O(\eta^2)\right). \quad (3.23)$$

By comparing eq. 3.17, the low energy result, with eq. 3.23, the high energy result, it is clear that the latter can be regarded as an expansion of the first if it is written as:

$$ct = \frac{d}{\beta}\frac{2\mu+2}{2\mu+1}\frac{\beta^2(\epsilon+1)^3}{2\epsilon_t}\left(\frac{\epsilon_t}{\epsilon_{t,pt}}\right)^{\mu+1} \times\left(1 - \left(1 - \frac{2\epsilon_t}{\beta^2(\epsilon+1)^3}\left(\frac{\epsilon_{t,pt}}{\epsilon_t}\right)^{\mu+1}\right)^{\frac{2\mu+1}{2\mu+2}}\right), \quad (3.24)$$

where all velocities and energies are at $x = 0$ and η is replaced by its definition.
Eq. 3.24 is exact to first order in the energy loss. At higher energy loss it is at least a good approximation as it converges to 3.17 for low energies (although it should be noted that ϵ_0 is neglected in the derivation of 3.17).

3.2 Detector calibration

The equations derived in the previous section give a framework for the calibration of the Huygens detector. Essential for each calibration is that at some point the modules have to be gauged on one fixed point. The accuracy which can be reached for this point determines the maximum accuracy which can be obtained in all measurements. For the MUR modules and the forward plastics this point is the punch-through energy for α-particles. The sideward plastics were calibrated via measurements of the energy deposition of cosmic radiation. The microstrip gas chamber was calibrated for the energy loss in an *ad hoc* manner as this information was only used for particle identification. The Huygens detectors basically identify the atomic number, Z, of a particle. The atomic mass number was taken to be Z^2 for $Z \leq 2$ and $2Z$ for heavier particles.

3.2.1 The MUR

The MUR is a time-of-flight wall which covers the polar-angular range from 3° to 30° [32]. Fig. 2.1 shows the MUR together with the other modules of the Huygens detectors. The MUR is located 2.10 m from the target and is subdivided in 96 modules arranged in seven rings. The first two rings consist of eight modules each, while the other rings consist of sixteen modules. Each module is a plastic scintillator sheet (NE102A) of 2 mm thickness.

The time-to-analogue converters (TACs) used in the read-out of the MUR modules were calibrated with pulser data taken directly after the experiment. All modules had a sampling time of approximately 250 ns. In order to determine the TAC offset, the

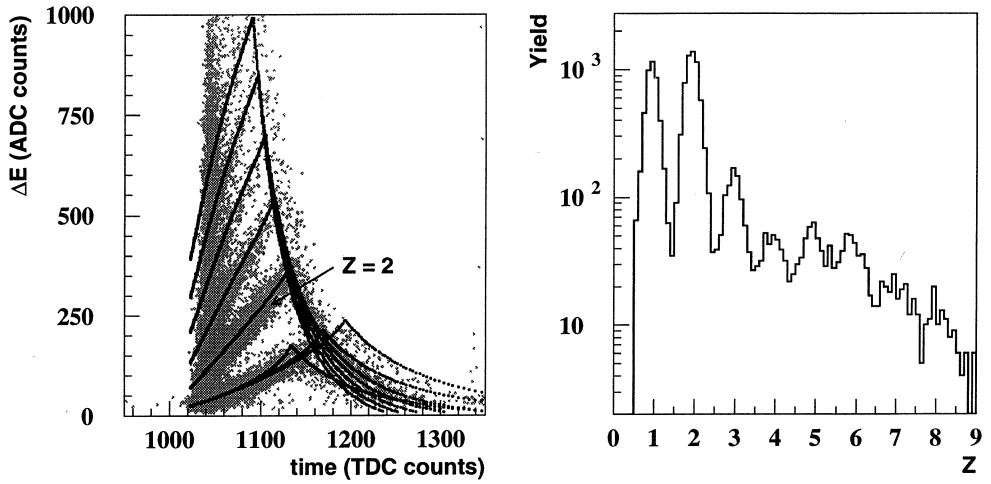

Figure 3.1: *On the left: uncalibrated time of flight versus light output measurement from one of the inner MUR-modules. The lines are the calculated values for the detector response. On the right: calibrated Z values of the punch-through particles.*

digitised TAC value belonging to punch-through α-particles was determined from the data for each module. As the energy of these particles is known, the flight time can be calculated with eq. 3.24. This determines the TAC offset.
The light output for punch-through α-particles was also determined. With this observable the light output for each module can be normalised. Eq. 3.10 and eq. 3.24 can now unambiguously give energy and particle identification for each particle passing through the module. Particles stopped in the module can not be identified, unless they are also detected by the forward plastic scintillators. In fig. 3.1 data from a module of the second ring is shown (left). The lines are the calculated detector response. On the right the projected Z values are shown. Fig. 3.1 shows a good agreement between the calculated detector response and the data. Furthermore Z-separation at least up to $Z = 8$ can be achieved.

3.2.2 The central trigger detector

The central trigger detector (CTD) is the primary detector in our set-up. Fig. 2.3 shows the CTD with the CIW. It consists of 48 plastic scintillators, 32 arranged cylindrically around the beam axis (the sideward plastic scintillators) and 16 perpendicular to this axis (the forward plastic scintillators), which results in a barrel shaped detector. This barrel is filled with a counting gas and is read out by 128 microstrip detectors, arranged in three concentric rings also perpendicular to the beam axis. A 5 kV electric field makes the liberated electrons in the gas drift to the microstrips. The event trigger is a logical .OR. between a selectable number of forward and sideward plastic scintillators.

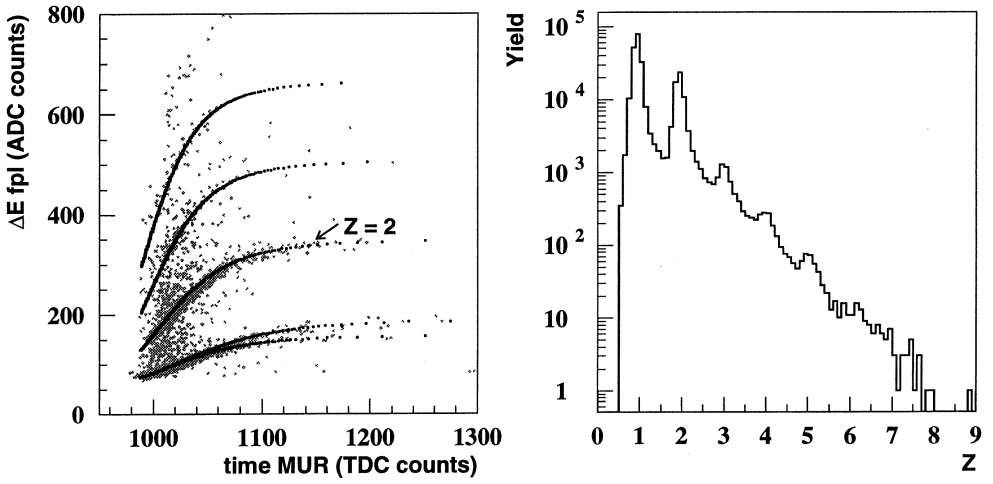

Figure 3.2: *On the left: uncalibrated time of flight from the MUR versus the light output from one of the forward plastics. The lines are the calculated values for the detector response. The lower line is the proton line, followed by the deuteron line, the other lines are the the most abundant isotopes for $Z = 2$, 3 and 4. On the right: calibrated Z values of the particles accumulated for all forward plastic modules.*

The forward plastic scintillators

The forward plastic scintillators are 16 trapezoidally shaped scintillators (NE102A), with dimensions $10 \times 180 \times 75$ mm^3. The angular range of the forward plastics is from 11° to 27° in polar angle. The modules all cover 22.5° in the azimuthal angle ϕ. Each module fits, like a piece of pie, in the ensemble of the other plastics, perpendicular to the beam axis, as shown in fig. 2.3.

Because of the relatively long flight distance and the accurate calculation of the flight time, the best energy measurement in the Huygens-detector set-up is done with the timing in the MUR modules. Therefore, this measurement is taken as a gauge for the forward plastics. In order to calibrate the forward plastics, each module was divided in four sections, corresponding to the four MUR modules behind each section. For each separate subsection the TDC and QDC value of the punch-through α-particles were determined. The QDC value is the digitised signal amplitude including the pedestal. Because the sampling time of the forward plastics is known, i.e. 100 ns, the time offset can be calculated. The QDC pedestal is measured throughout the experiment. The light output can then be normalised and again eq. 3.10 and eq. 3.24 give energy and particle identification. As the detector is situated close to the vertex, the timing information is not very accurate. It was found that the best particle identification can be obtained with the timing of the MUR module in conjunction with the light output of the forward plastic. This procedure is only possible for particles with enough energy

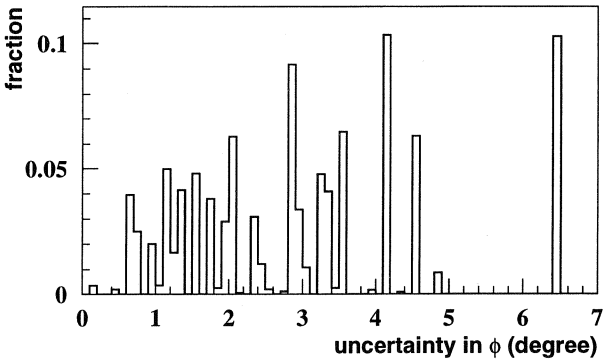

Figure 3.3: *The distribution of the uncertainty in ϕ measured in the TPC. Each microstrip in the first ring has a generic uncertainty of 6.4°. By combining the different hits of a track the resolution is improved.*

to reach the MUR module. In fig. 3.2 the raw data and the calculated detector response are given. Particles with lower energies are identified with the QDC value in the plastic scintillator and the QDC value of the microstrip. The calibration of the microstrip is discussed in the next subsection.

The time projection chamber

The time projection chamber (TPC) is read out by 128 microstrip gas counters (MSGCs) arranged in three concentric rings around the beam axis. The first ring consists of 28 microstrips, the second of 44 and the third ring contains 56 microstrips. The distance from the MSGCs to the cathode foil is 52 cm. The TPC covers 11° to 78° in polar angle. Each microstrip has a resolution in ϕ of 6.4° in the first ring, 4.1° in the second and 3.2°in the third ring. By combining the angle measured in the plastics and the different microstrips, it is often possible to obtain a better resolution. In fig. 3.3 the distribution of the uncertainty in ϕ in the TPC is plotted. The mean resolution is approximately 3.1°.
The TPC was designed to measure two observables. Firstly, the drift time of the electrons in the counting gas is used to determine the angle of a particle passing through the chamber. Secondly, the amplitude of the signal measured in the chamber, in conjunction with the signal in the plastic scintillator, is used to determine the atomic number of the particle. Several corrections on the microstrip observables are necessary.

There are two simple corrections needed on the data due to the geometry of the TPC. If the field lines in the TPC are straight, the flight path of a particle passing over the detection area of the microstrip will be proportional to $1/\tan(\theta)$, where θ is the polar angle of the particle. The liberated charge in the gas is proportional to this flight path and a correction for this effect is necessary. Still assuming straight field

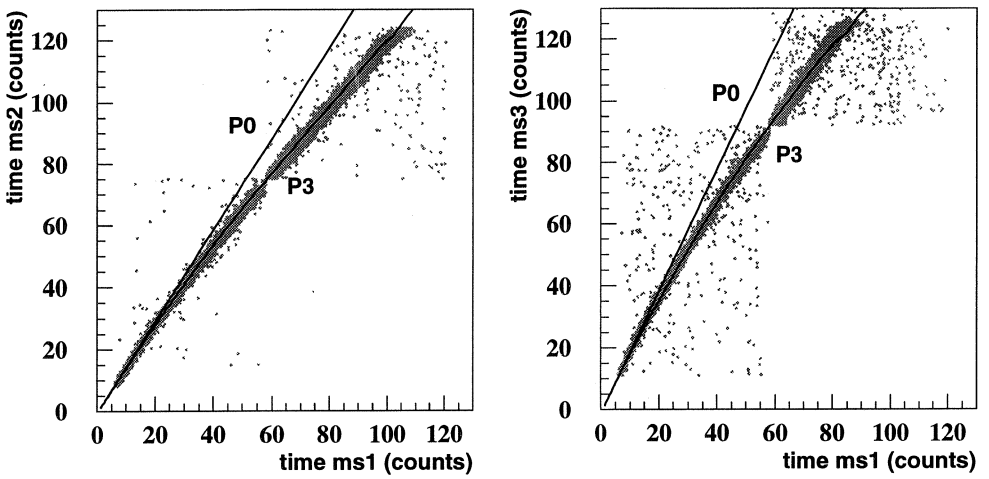

Figure 3.4: *Correlations between time measurements in ring 1 and 2 (left) and 1 and 3 (right). The lines concur with the detector response if there are straight, horizontal field lines (P0) and if the field lines are a third-order polynomial (P3).*

lines, the distance between the first and the last liberated electron will be proportional to $\cos(\theta)$. This distance is proportional to the time needed for the preamplifier to collect all the charge. The response of the preamplifier is influenced by the collection time, which makes corrections necessary for both the time measurement and the charge measurement of the microstrip. However, as CF_4 has a high drift velocity, i.e. short signals, these corrections are small ($< 5\%$).
In fig. 3.4 the time measurements in the different microstrip rings are plotted. The correlations between the time measurements in the different rings do not concur with the assumption that the field lines are horizontal, in this figure indicated by the line P0. Three third-order polynomials were fitted to the data to parametrise the field lines. First the transition points between the MUR modules and between the forward and the sideward plastics in the TDC of the microstrips were determined. The angles belonging to these TDC values are known. These transition points, and the TDC values of the first-ring microstrips as a function of the other two rings were used in a least-square fit to the three polynomials. The resulting field lines yield the time measurements indicated in fig. 3.4 with the line P3 and are in good agreement with the data. The resolution of the polar angle measurement is better than 1° at 78° and better than 0.25° at 10° polar angle. In fig. 3.5 a scaled representation of these field lines in the TPC is shown.

With these corrections it is possible to determine the angle of the particle. However, two additional *ad hoc* corrections are needed for particle identification. Firstly, the measured signal amplitude showed an increase in the yield from the microstrip as the

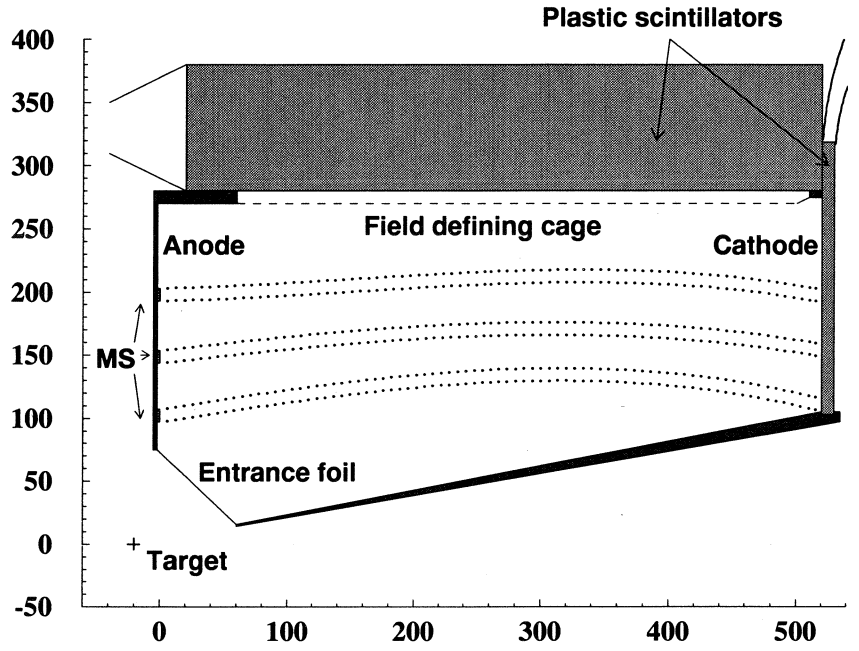

Figure 3.5: *Shape of the field lines in the TPC (dimensions in mm).*

drift path shortens. This effect was quantified and the data was corrected for an approximate 30% increase in gain over the length of the TPC. It can be argued that this increase in yield is caused by the divergence of the field lines. As the field lines do not follow a straight line, it is likely that a divergence is also present, which would explain this effect. In fig. 3.6 the correction factor to the microstrip gain (averaged over all microstrips) is plotted as a function of the angle of a particle. As the microstrips were calibrated separately for the sideward and forward scintillators the smooth transition in this graph at 27.5° is an indication that the calibration is correct. The dip at 10° is attributed to the vicinity of the cathode foil. Electrons liberated from the foil by the particle enhance the measured signal. This is not included in the signal calculation and, therefore, lowers the gain.
Secondly, the parametrisation used to calculate the energy loss in the plastic scintillator with eq. 3.3, could not describe the energy loss accurately over the whole Z range in the drift chamber. This could be compensated for by multiplying this function with $(Z^2/m)^{0.3}$. This is equivalent to changing the medium-dependent constant μ for the gas. It should be stressed that these corrections have no effect on the energy measurement of the particle and merely allow for a correct Z identification.

In fig. 3.7 the result of the calibration is shown. On the left-hand side the QDC value

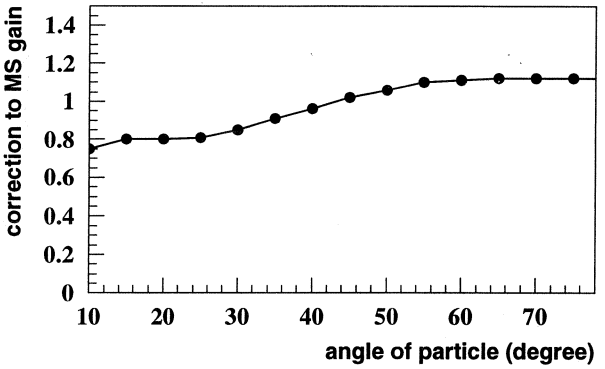

Figure 3.6: *The correction factor for the gain in the microstrip (MS) as a function of the angle of the particle. The line serves to guide the eye.*

of a microstrip is plotted against the light output of the forward plastic scintillator. The lines are the calculated detector response. The plot on the right-hand side is the Z-projection of this data.

The sideward plastic scintillators

The sideward plastic scintillators (NE102A) are a barrel shaped ensemble of 32 trapezoidal plastics, 10 cm thick, approximately 5 cm wide and 50 cm long. The ensemble covers 28° to 78° in polar angle. Each module covers 11.25° in ϕ and is read out by a single photo-multiplier at approximately 85° polar angle. The detector is used as a calorimeter; the particles are stopped in the plastics and the signal is proportional to the incident energy.

The uncalibrated data indicated a large influence of attenuation of the signal as a function of distance to the photo-multiplier. Therefore, this effect was measured by determining the 0.481 MeV and the 0.975 MeV β peaks from a $^{207}_{83}$Bi radioactive source. In fig. 3.8 the results of the measurements are shown. The different marker types are results of measurements from different plastic modules. It was found that the attenuation effect was significantly more than what is described in the specifications of NE102A. However, the measurements could be described by a model, which calculates the trajectories of the light rays in the geometry of the plastics assuming 80% reflection at the sides and the attenuation length from literature of 250 cm. This model is described in [41, 65]. The results of the model are also shown in fig. 3.8 and are in agreement with the measurements.

The sideward plastic scintillators were calibrated with cosmic-ray data taken immediately after the experiment. The cosmic-ray data was simulated by a GEANT simulation

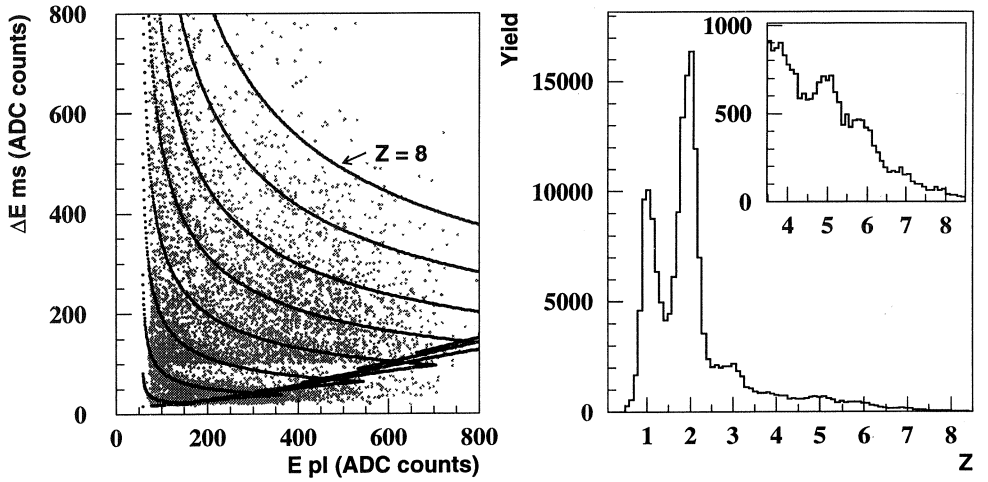

Figure 3.7: *On the left: uncalibrated data of the energy loss in the TPC versus the light output in a forward plastic between 15° and 20°. The lines are the calculated values for the detector response. The data with a ΔE value less than 100 are reduced in statistics by a factor of 10. On the right: calibrated Z values of the particles accumulated for all forward modules at these angles.*

program, including the aforementioned attenuation effect (see section 1.3.2). The most probable energy deposition calculated by GEANT was 20.0 MeV. The gain extracted from the cosmics was taken to be equal to that of the $\frac{dL}{dE}$ of high-energy protons, which is similar to that of high-energy α-particles.

3.2.3 The CsI(Tl) wall

The CsI(Tl) Wall (CIW) is an array of 64 CsI(Tl) modules located in the backward hemisphere in the laboratory frame. The CIW in conjunction with the CTD is shown in fig. 2.3. Fig. 2.2 shows the CIW in detail. The modules are each 5 cm wide, 5 cm high and 1 cm thick. In the laboratory frame the detectors are situated between 121° and 177° polar angle. They are grouped in 4 arrays of 16 detectors and cover approximately 80% of the backward hemisphere. It was designed as a low-threshold detector for light ions with Z=1 or 2.

Due to experimental difficulties the signal to noise ratio was quite poor. Therefore, it was not possible to achieve particle identification and energy determination. However, it was possible to use the CIW as a multiplicity counter with an estimated energy threshold of 5 AMeV.

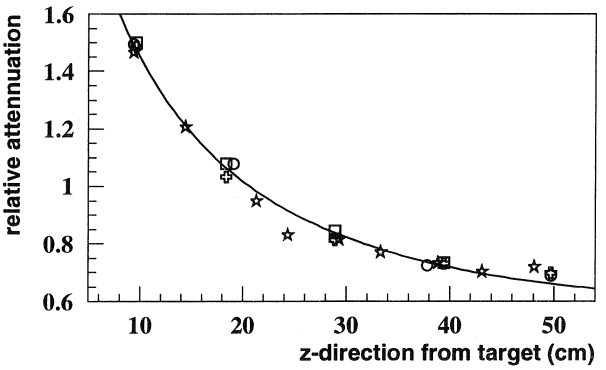

Figure 3.8: *Relative attenuation in the sideward plastic modules as a function of the distance from the target parallel to the beam direction. The marker types indicate measurements from different plastic modules. The line is the result of a light-tracing model calculation with an attenuation length of 250 cm and 80% reflection at the surfaces.*

3.3 Detector performance

The physics of a nuclear reaction can not be studied without the full knowledge of the effects the detector has on the observables. Therefore, the acceptance, the thresholds and the identification properties of the Huygens detector have been investigated. Furthermore a GEANT detector simulation was used to verify the calibration accuracy.

3.3.1 Acceptance and identification properties

In order to check the calibration and the efficiency of all the subdetectors, the energy and angular distributions of the different subdetectors were compared.

In the region between 10° and 27° in polar angle, depending on the energy of the particle, the identification is done in the forward scintillators in conjunction with either the TPC or the MUR. If the particle is stopped in the forward scintillators, the TPC is used to identify it, otherwise the MUR gives a better Z-separation. It is evident that the energy distribution should be continuous over this transition. In fig. 3.9 the energy distribution for protons (on the left) and α-particles (on the right) in the forward region are plotted. In the upper panel the data is shown for a beam energy of 45 AMeV. The lower panel contains the 95 AMeV data. The proton results show that the TPC can only detect protons up to approximately 25 MeV. As was already argued in section 2.1.2, this should give a complete coverage for α-particles. Indeed the right-hand side of fig. 3.9 shows an almost continuous transition between the TPC and the MUR. The continuity is slightly distorted by particles stopped in the 2 mm thick MUR module, which show a systematic preference to be identified with a higher energy than what is expected. For the 95 AMeV data a minimum in the distribution

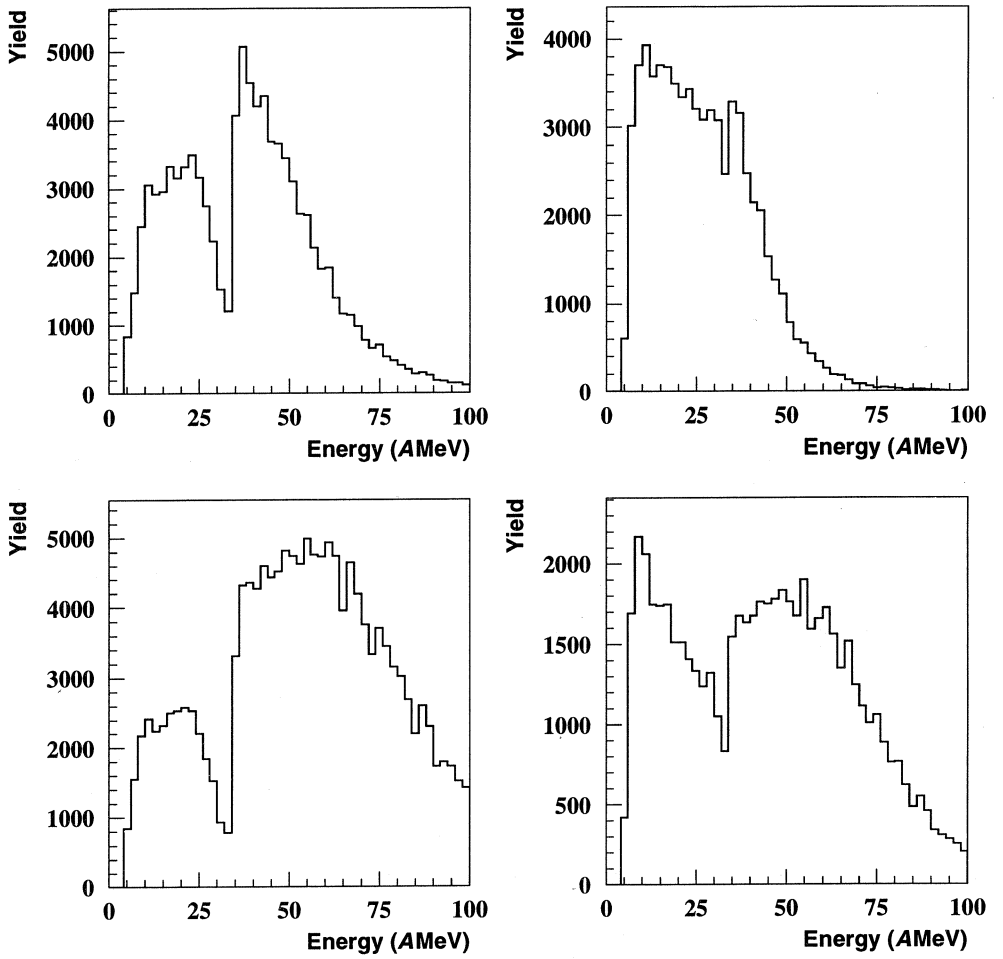

Figure 3.9: *Energy distribution of protons (left) and α-particles (right) for 45 (top) and 95 (bottom) AMeV. Below approximately 36 AMeV particles are identified in the CTD. Above this energy particles are detected and identified in the MUR and the forward scintillators. For α-particles an almost continuous curve is seen for both energies. Protons are only identified in the TPC up to approximately 25 AMeV.*

is expected at approximately the punch-through energy. Particles emitted by the target cause a maximum at low energies and at high energies a maximum is caused by particles originating from the projectile.

At 27.5° polar angle a support structure covering approximately 1° separates the forward from the sideward scintillators. In fig. 3.10 the angular distribution for α-

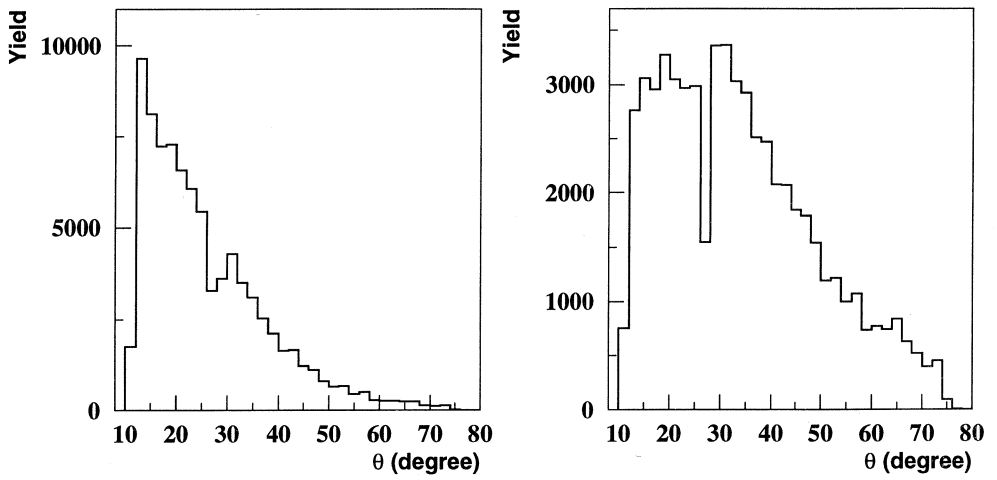

Figure 3.10: *Angular distribution of α-particles in the laboratory frame for particles with energy between 10 and 30 AMeV for 45 (left) and 95 (right) AMeV. Under 27.5° polar angle the identification is done in the forward scintillators. Above this angle particles are detected with the sideward scintillators. Both graphs show a continues distribution. For 95 AMeV the energy cut excludes the projectile like fragments in the forward region.*

particles with an energy between 10 and 30 AMeV in the laboratory frame is plotted for 45 AMeV (left) and 95 AMeV (right) beam energy. With the exception of the missing channel at 27.5°, both graphs are continuous. The shape of the distributions are governed by the energy cuts. For the 95 AMeV data the particles from the projectile are excluded from the graph at small angles (as can be seen in fig. 3.9), which qualitatively explains the decrease in yield at these angles.

Fig. 3.11 shows the measured energy distribution for $Z = 2$, 3, 4 and 6 in the sideward scintillators (28° to 78° polar angle). The slopes indicate a complete energy coverage for all the shown particles, as was expected from the detection limit of the protons. The lower thresholds for particle identification are angle and particle dependent. Below 10° polar angle the thresholds are equal to the punch-through energy of the particle in the 2 mm thick scintillator. For $Z = 1$ and 2 this amounts to 14 AMeV, for $Z = 6$ the energy threshold is 26 AMeV. In the TPC the angular dependence is small, ranging from 6 AMeV at 10° to 7 AMeV at 30° to 4 AMeV at 75° for $Z = 2$. For $Z = 6$, these values are respectively 10, 11 and 9 AMeV.

3.3.2 The GEANT detector simulation

Any detector set-up will have an effect on a measurement. Thresholds and angular resolutions are obvious effects, but also signal distortion due to for instance multiple

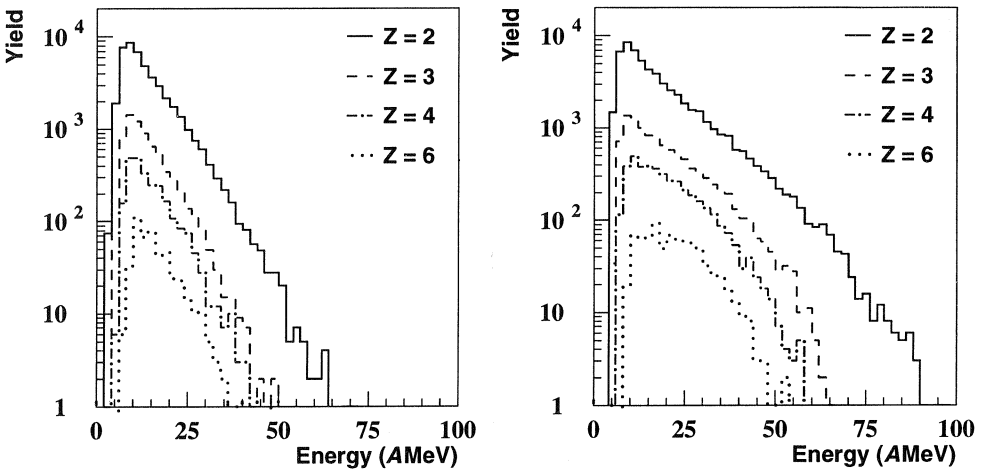

Figure 3.11: *Energy distribution for Z = 2, 3, 4 and 6 between 28° and 78° polar angle for 45 (left) and 95 (right) AMeV*

hits will influence the data. These effects have to be taken into account. One possible method is to *unfold* the data extrapolating it to the areas which have not been measured. This is a solution when doing a statistical analysis. Furthermore, this is only possible if all detector effects are known and parametrised. When doing an *event by event* analysis this method is not applicable. Comparison of data to simulations is then only possible by filtering the simulation with detector effects. The GEANT program [66] was used to describe the Huygens detector set-up. GEANT uses an accurate geometric description of all materials in a set-up. It then calculates for all (input) tracks the trajectories through the detector. Energy losses are calculated stochastically, as are nuclear-collision probabilities. GEANT was developed for particles with ultra-relativistic energies, therefore, the energy loss tables had to be slightly modified to match the expected energy loss in the TPC. To calculate the energy loss in the gas correctly, a flag was set to simulate energy loss in thin materials. For further details see section PHYS334 of [66]. Each simulated event can thus be filtered for the detector effects. The GEANT simulations were primarily used to filter the IQMD simulations (described in the next chapter) with the detector effects.
They were also used to calculate the energy loss of cosmic radiation in the sideward scintillators. In both the data and the simulation an angular constraint was used by demanding a hit in two opposite scintillators, therefore, the energy distributions for the different plastics differ only in statistics. The most probable energy loss of muons with an energy distribution equal to that of cosmic radiation is 20.0 MeV. The attenuation effect, described in the previous section (see fig. 3.8), was folded into simulated cosmic-ray data in GEANT. This amounted to a shift of 10% of the maximum in the energy distribution. In fig. 3.12 the energy measurement with and without the attenuation

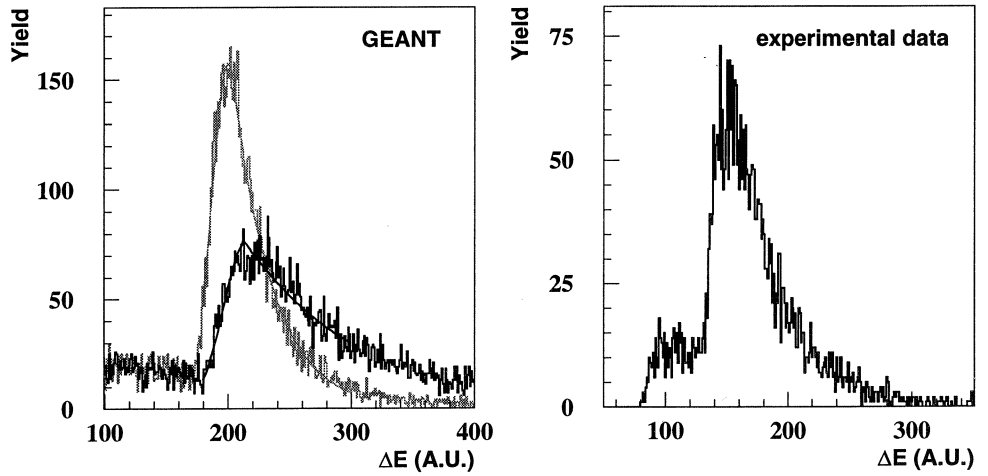

Figure 3.12: *On the left: the effect of the attenuation in the sideward scintillators on the measurement of the cosmic radiation. The gray line is the simulation without the attenuation effect. The black line shows the simulation with the attenuation. The effect amounts to an approximate shift in the maximum of 10%. On the right: experimental data. The pedestal for this data is 47 channels (x-axis).*

effect are plotted on the left-hand side. The dark line shows the simulation with attenuation, the gray line is the simulation without this effect. On the right-hand side a plot is shown of the experimentally measured data with one of the plastic scintillators.

3.3.3 Conclusions

The following conclusions can be reached about the detector performance:

- Particle identification is possible between 3° and 78° polar angle in the laboratory frame. In this region 360° azimuthal angle is covered. The polar angle resolution is better than 1° between 10° and 78° and the mean azimuthal resolution is 3.1°. The backward hemisphere is covered for 80% by a multiplicity counter with a particle threshold of approximately 5 AMeV.
- Identification of ions between $Z = 1$ and $Z = 8$ is possible.
- For $Z > 1$ the complete energy range of the reaction can be measured with an angle and particle dependent threshold of around 10 AMeV.

4

Model calculations

Experiments with heavy-ion collisions yield many observables which contain information about the reaction mechanics. It is not possible to draw conclusions from these observables in an easy way. As in most subatomic physics experiments it is necessary to do elaborate calculations to extract information from the data. Because of the complexity of the reaction, i.e. the large number of participant nucleons, the only feasible way of doing this is to compare the data to simulations in which the reaction mechanism is known.

This chapter describes several of the models available for the interpretation of heavy-ion collisions, but mainly elaborates on Isospin Quantum Molecular Dynamics (IQMD), which is compared to the data in the following chapter. The first section is a short introduction in the field of model calculations for heavy-ion collisions. In this part the motivation for the use of IQMD is discussed. In section 4.2 one of the primary features in the study of heavy-ion collisions is discussed, the equation of state (EOS). The emphasis is put on the implementation of the EOS in the simulations. In section 4.3 a more detailed description of IQMD is given. Section 4.3.1 gives the framework of the theory on which IQMD is based. In section 4.3.2 the IQMD program and cluster algorithm is discussed. The final section, 4.3.3, presents some more general results of IQMD simulations for the ^{24}Mg+^{27}Al reaction at 45 and 95 AMeV.

4.1 Introduction

During the last two decades a great deal of progress has been made in the study of heavy-ion reactions, both in experiments and in theory. The development of better

nuclear-accelerator facilities, extending the energies and Z-ranges for projectile nuclei and the advent of full-coverage detectors have induced major advances in the experimental field. Furthermore, the exponential growth of computing power has made it possible to develop complex models for the study of heavy-ion reactions.
In this thesis the *intermediate*-energy range is studied. Projectiles with energies from 20 to approximately 100 AMeV are part of this domain. Unless otherwise stated, the models discussed in this chapter can all be used in this energy domain. Many of them can also be applied at much higher energies.

One of the goals in the study of heavy-ion collisions is the determination of the equation of state (EOS) of nuclear matter. In the overlap region of two heavy ions during a collision a region is created with high nuclear pressure and temperature. Early hydrodynamical models show that, in the intermediate energy range, a density in the overlap region 2-5 times the normal nuclear density is created. In this region of high pressure the temperature will also rise sharply [67, 68]. Probing the temperature-density relation by varying the experimental conditions should yield information on the EOS. However, it is by no means trivial to extract this information from the data. Note that the macroscopic quantities temperature and pressure imply that the system is at thermal equilibrium. However, the discussion about how and when thermal equilibrium is reached is not settled yet. In fact, in this thesis it will be shown that for small nuclear systems, there is no evidence of thermal equilibrium.
The main method to extract information from heavy-ion collisions on the EOS is to study the collective motion of nuclear matter. Hydrodynamical models are able to describe the global features of collective motion. In these models, nuclei are represented by droplets of nuclear matter with a uniform density [69, 70]. The most important input for these models is the EOS, the relationship between the internal energy and the pressure, thus directly linking the EOS and the observables. This feature makes these calculations a convenient tool to study heavy-ion collisions. The hydrodynamic approximation gives a good picture of the collective motion of nuclear matter. During the collision three different systems are created [71, 72], firstly in the overlap region, matter is compressed and heated. Secondly, two separated regions, target-like and projectile-like, of cold spectator matter are present. The matter in the overlap region will experience a pressure gradient which is strongest perpendicular to the reaction plane, because the phase space in the reaction plane itself is shielded by the cold spectator matter. This leads to collective motion called *out-of-plane flow*. Within the reaction plane, the colliding nuclear matter experiences two opposite forces. It is attracted by the strong nuclear binding force and deflected by the pressure gradient, filling up the energy states in the collision region. At low beam energies, the first force is the strongest. As the pressure increases with increasing beam energy, the latter process becomes dominant. This collective motion is known as *directed in-plane flow*. The commonly associated observable with this directed flow is the *balancing energy* (E_{bal}): the beam energy where the two processes cancel. Depending on the mass of the target and projectile, E_{bal} will be less than 40 AMeV for large ions to over a 100 AMeV for small ions.
Hydrodynamical models were reasonably successful in describing nuclear collisions, but

there were some obvious drawbacks. The discrete properties of nuclear matter are not described by these models. The approximation of nuclear matter as a fluid with a continuous density profile will not be able to describe any effects due to the statistical fluctuations associated with a system with a finite number of nucleons. This is not only a fundamental problem of hydrodynamics, it also gives difficulties in the comparison of the model to the data. There are two ways to solve this problem. In the first place it is possible to unfold the data, extrapolating it to the thermodynamic limit. Alternatively a Monte Carlo procedure can be incorporated in the simulation, drawing *events* from the calculation with a finite number of fragments. Because the microscopic features are not included, only global observables can be studied.
Although in this way a reasonable description of collective motion can be achieved, it is not possible to give a good description of the fragment distribution. In particular the production of intermediate mass fragments (IMFs), fragments with $Z \geq 2$, is not possible. It was found that at $E_{\mathrm{beam}} > 35$ AMeV a reaction channel opens where several of these IMFs are produced and that multifragmentation becomes the dominant reaction channel [18]. The power law behaviour of the mass yields, $\sigma(A) = A^{-\tau}$, was deduced to be a signature of the phase transition between liquid and gaseous nuclear matter [73]. Nuclear-matter theory predicts a phase transition, similar to a Van der Waals system, to occur in an infinite system at nuclear densities higher than $\rho_0 = 0.15$ fm^{-3} [16, 17, 74, 75, 76]. As in a Van der Waals gas, nuclear matter exists of elements which have a long range attractive force and a short range repulsive force. After the initial compression and heating of the nuclear matter, a decompression phase provides the conditions for multifragmentation. It is speculated that at this point in time the system breaks up into *droplets* of nuclear matter (prompt multifragmentation). It is also possible that the fragments are formed in a sequence of well separated emissions from a hot source (sequential decay). It should be noted that both scenarios explicitly require an equilibrated nuclear system. Statistical models based on prompt multifragmentation (e.g. [77, 78]) and sequential decay (e.g [79, 80]) both neglect the dynamics of a heavy-ion collision and start with an equilibrated source with a number of nucleons A_0, atomic number Z_0, volume V_0 and excitation energy E_0. In multifragmentation models this compound system expands (thermodynamically) until it reaches the breakup volume $V_{\mathrm{b}} > V_0$. At this point the system breaks up into several fragments. After this primary breakup, excited fragments may evaporate (into) nucleons or undergo secondary breakup. In sequential decay models each event can be represented by a tree where each branching represents a certain emission of a fragment with atomic number Z_{f} after a time t_{f}, which are determined stochastically. For high excitation energies the model becomes somewhat complex and it is convenient to make approximations. This can be done by coupling the kinetic energy generated by the fragment emission to the expansion of the volume of the system and decreasing the temperature as excited fragments are emitted [80]. There are several drawbacks to the use of these statistical models. Firstly, it is questionable whether it is viable to assume an equilibrated source. Furthermore the parameters A_0, Z_0, V_0 and E_0 are *a priori* not known. As is the case with V_{b}, t_{f} and Z_{f}. These variables have to be tuned to the data, or might be taken from theory. Especially in the intermediate-energy region the source size, or the existence of a source, is unknown. Moreover, comparison with experiment is made

difficult by the fact that in the measurements the signal from the (possible) source is diluted by spectator decay products.
A phase transition is also studied in the percolation [81] or nuclear lattice model [82]. In these rather abstract models nucleons are represented as points on a lattice. Not the nucleon-nucleon collisions are studied, but the bonds between the nucleons. The probability of a bond being broken is introduced in the model. With a Monte Carlo technique it is decided which of the bonds are broken and thus which fragments are formed. It can be assumed that the probability of a bond being broken is an increasing function of the excitation energy of the compound system.
A logical evolution in the approach to the modelling of heavy-ion collisions was the diversion from the phenomenological approach toward a microscopic description of the event. Cascade models attempt to do this [83]. In fact a complete nucleus is initialised with all its constituent nucleons, without taking into account Fermi motion or a nuclear potential. Then the target and projectile are made to collide. These simulations show a strong participant spectator separation. In experiments this is only seen at $E_{\text{beam}} > 200\ A\text{MeV}$, which renders the model inadequate for lower energies. In the overlap region the collisions between nucleons are stochastically determined to be either elastic or inelastic. The exit channel and particle angles after the inelastic collisions are also generated stochastically. Like hydrodynamical models, microscopic models allow an experimenter to calculate quantities such as pressure and temperature during the evolution of the collision, which is not possible in the phenomenological decay models. However, unlike hydrodynamics, they also take into account the microscopic properties of the nuclei. Neglecting Fermi motion and the nuclear potential makes the cascade model a somewhat crude approximation.

The growth in computing power made it possible to develop increasingly complex microscopic models for the simulation of heavy-ion collisions. Nowadays two different approaches are dominant, firstly the single-particle mean-field approach, secondly quantum molecular dynamics.

Several models follow the single-particle mean-field approach and are fundamentally the same. In this work the name Vlasov-Uehling-Uhlenbeck (VUU) is used [84, 85], however, Boltzmann-Uehling-Uhlenbeck (BUU) [84, 86], Boltzmann-Nordheim (BN) [87] or Landau-Vlasov [88] are also widely used in literature. The distinction between the models is the numerical realisation of the simulation. In the VUU models two-body and higher-order correlations between nucleons are ignored. Every nucleon is represented as $\tilde{n}$ test particles moving in a mean field. This mean-field potential can be defined in terms of the density of these test particles. Usually a Skyrme potential, which is discussed in section 4.2 and a Yukawa potential are the main contributors to the mean field. A Coulomb interaction can also be included. Fermi motion is assigned to the particles in the mean field in accordance with the Pauli principle. Test particles move through the mean field following the classical Hamilton equations. The Liouville-equation is used as the fundamental many body transport theory. After an integration of the N-body function over $N-1$ degrees of freedom and neglecting two-body correlations, the Vlasov equation is obtained. This equation only yields one-

body correlations. Collisions are not incorporated in the described transport equation, therefore, the Uehling-Uhlenbeck collision term [84] is added in, also taking into account Pauli blocking. The VUU-equation can then be written as:

$$\begin{aligned}\frac{\partial f_1}{\partial t} + \mathbf{v}_1 \cdot \nabla_{\mathbf{r}} f_1 - \nabla_{\mathbf{r}} U \cdot \nabla_{\mathbf{p}} f_1 &= -\frac{1}{(2\pi)^6} \int \mathrm{d}^3\mathbf{p}_2 \mathrm{d}^3\mathbf{p}_1' \mathrm{d}^3\mathbf{p}_2' \; \sigma \; v_{12} \\ &\times \; (f_1 f_2 (1 - f_1')(1 - f_2') - f_1' f_2' (1 - f_1)(1 - f_2)) \\ &\times \; \delta^3(\mathbf{p}_1 + \mathbf{p}_2 - \mathbf{p}_1' - \mathbf{p}_2'). \end{aligned} \tag{4.1}$$

The left-hand side of eq. 4.1 is the Vlasov equation, where f_1 represents the single particle distribution function containing the properties of all the particles, $\mathbf{v}_1$ the velocity distribution of the particles and U the potential. The subscripts of the vector derivative ∇ indicate if the operator works in coordinate or in momentum space. The right-hand side is the Uehling-Uhlenbeck collision term, with σ the effective nucleon-nucleon cross section normalised to the number of test-particles $\tilde{n}$ and v_{12} the initial velocity difference between the particles. The $f_1 f_2$ term calculates the probability that two particles with momentum $\mathbf{p}_1$ and $\mathbf{p}_2$ collide into states with momentum $\mathbf{p}_1'$ and $\mathbf{p}_2'$. Pauli blocking is taken into account by the $(1 - f_1')(1 - f_2')$ factor, making sure that the scattering cannot occur into states which are already occupied. States that are occupied after the collision because scattering could not occur due to Pauli blocking are accounted for by the term $f_1' f_2' (1 - f_1)(1 - f_2)$. Momentum conservation is ensured by the integral over the δ-function. For a derivation of eq. 4.1 see [89]. It should be noted that in the VUU-method the particles, which are mentioned above, are the test particles of which $\tilde{n}$ make up a nucleon. Unavoidably using many test particles to represent a single nucleon suppresses statistical fluctuations during a collision. In fact an event in VUU is an averaging of (or summation over) $\tilde{n}$ collisions. This smears out the fluctuations and correlations within an event deemed essential for the formation of IMFs.

Quantum Molecular Dynamics (QMD), discussed in section 4.3, is a model which does include these effects and thus gives a natural description of fragment formation [90, 91, 92]. QMD is a classical N-body theory with the Pauli principle, stochastic scattering and particle production added in. Nucleons are represented by Gaussian wave packets. The particle trajectories are calculated for each nucleon individually, taking into account the Coulomb potential, the Yukawa potential and a Skyrme-type local potential. Extensions to the theory may include effects like a momentum dependent force and isospin asymmetry. Because each nucleon is represented individually and not, like in VUU, averaged over several events, fluctuations are natural, similar to the experiment. Although this might influence the stability of the system, it ensures that the correlations within an event are conserved. Thus QMD is a self-consistent model which includes fluctuations, fragment formation and correlations.
Because the analysis in this thesis focusses on the correlation between IMFs, a QMD-type model is the best option available. The only other models including fragment formation and correlations are statistical decay models, but these do not include the collision dynamics, which is important in heavy-ion collisions of small systems.

4.2 The equation of state

The equation of state (EOS) is a thermodynamic equation, which describes the relationship between two or more macroscopic quantities, e.g. temperature and pressure. Using statistical mechanics, such a macroscopic relationship can be derived from the microscopic properties of the interacting particles. So in order to calculate the EOS of nuclear matter a description should be found of the interaction between the nucleons in a nuclei. This can be done in two different ways. Firstly a description can be made using the physical reaction which takes place between the nucleons: the exchange of virtual mesons. Secondly an effective potential can be constructed, which only describes the effect of the interaction of the virtual meson field for two, three or more nucleons. The resulting force of the two methods should be the same. Obviously the latter is a more convenient method for the use in computer simulations.

Any description of the nucleon nucleon forces should conform to three requirements:

- The interaction between nucleons is described by an attractive long range component and a repulsive short range part, the hard core. The two forces should be equal at $\rho_0 = 0.15$ fm^{-3}.
- The minimum in the binding energy should be -16 AMeV (for infinite nuclear matter).
- The compressibility, $\mathcal{K} = 9\rho\frac{\partial^2(E/A)}{\partial\rho^2}$ should be between 200 and 400 MeV.

The most commonly used potential in the models described above is the Skyrme potential [93, 94], both VUU and QMD use this potential.

4.2.1 The Skyrme potential

The Skyrme potential has been developed to describe the effective potential between nucleons in a infinite nuclear system [93, 94]. It does not account for the surface effects in finite systems. The potential takes into account the two- and three-body interactions:

$$V = \sum_i \sum_{j>i} V_{ij}^{\mathrm{A}} + \sum_i \sum_{j>i} \sum_{k>j} V_{ijk}^{\mathrm{B}}. \tag{4.2}$$

The potential for one nucleon in the ensemble of the other nucleons can then be calculated by integrating over the positions and momenta of all interacting particles. For the two-body potential the following *ansatz* is used:

$$\begin{aligned} V_{ij}^{\mathrm{A}} = t_0(1 + x_0\mathbf{P}_\sigma)\ \delta(\mathbf{r}_i - \mathbf{r}_j)\ &+\ \tfrac{1}{2}t_1(\mathbf{k}^{\dagger 2}\ \delta(\mathbf{r}_i - \mathbf{r}_j) + \delta(\mathbf{r}_i - \mathbf{r}_j)\mathbf{k}^2) \\ &+ t_2\mathbf{k}^\dagger \cdot \delta(\mathbf{r}_i - \mathbf{r}_j)\mathbf{k}\ +\ iW_0\mathbf{k}^\dagger\delta(\mathbf{r}_i - \mathbf{r}_j)\boldsymbol{\sigma}\cdot\mathbf{k}, \end{aligned} \tag{4.3}$$

where $\mathbf{k} = \frac{1}{2i}(\boldsymbol{\nabla}_i - \boldsymbol{\nabla}_j)$ is the relative momentum operator, $\mathbf{P}_\sigma = \frac{1}{2}(1 + \boldsymbol{\sigma}_i \cdot \boldsymbol{\sigma}_j)$ the spin exchange operator, $\boldsymbol{\sigma}$ the Pauli spin matrices, x_0 the spin exchange parameter and

EOS	$\mathcal{K}$ (MeV)	α (MeV)	β (MeV)	γ
hard	380	-124	70.5	2
soft	200	-356	303	$\frac{7}{6}$

Table 4.1: *Parameters for eq. 4.7 leading to different EOS with compressibility $\mathcal{K}$.*

W_0 the short range spin-orbit potential. The values of t_0, t_1 and t_2 can be changed to obtain different equations of state. The first term in eq. 4.3 contains a constant (zero-range) term and a spin-coupling term. Because in spin-saturated infinite nuclear matter the latter term is zero, it is usually neglected in model calculations. The second and third terms of eq. 4.3 are momentum dependent terms. In QMD these terms are also neglected, although an extra potential can be used to incorporate a momentum dependent repulsive force between the nucleons. The last term is the spin-momentum coupling. Again this term is not taken into account in most calculations.
For the three-body interaction also a zero-range force is assumed:

$$V_{ijk}^{\mathrm{B}} = t_3 \delta(\mathbf{r}_i - \mathbf{r}_j)\delta(\mathbf{r}_i - \mathbf{r}_k), \tag{4.4}$$

where t_3 is also a parameter depending on the EOS. This force can be approximated as a density dependent two-body interaction [95]. Neglecting the spin this yields:

$$V_{ijk}^{\mathrm{B}} \approx V_{ij}^{\mathrm{B}} = \tfrac{1}{6} t_3 \delta(\mathbf{r}_i - \mathbf{r}_j)\rho(\mathbf{r}_{ij}), \tag{4.5}$$

where $\mathbf{r}_{ij} = \frac{\mathbf{r}_i - \mathbf{r}_j}{2}$. With a Hartree-Fock approximation in infinite symmetric nuclear matter, neglecting the Coulomb potential, the global nuclear properties can be calculated using the Skyrme potential, see [95]. This calculation yields the single particle potential, U as a function of the nuclear density, ρ:

$$U = \tfrac{3}{4} t_0 \rho + \tfrac{3}{16} t_3 \rho^2 + \tfrac{3}{80}(3t_1 + 5t_2)\rho k_{\mathrm{f}}^2, \tag{4.6}$$

with $k_{\mathrm{f}} = (\frac{3}{2}\pi^2\rho)^{1/3}$ (in the Fermi gas approximation). Eq. 4.6 can be generalised to obtain:

$$U = \alpha\rho + \beta\rho^{\gamma}, \tag{4.7}$$

where α, β and γ depend on the properties of the EOS. Eq. 4.7 should describe the three features of nuclear matter listed at the beginning of this section. This gives us three boundary conditions for eq. 4.7. Thus it is possible to define different equations of state for different values for the compressibility $\mathcal{K}$. In table 4.2.1 the parameters are given for two of the most commonly used EOS, the *hard* and the *soft* equation of state. They can be tested in QMD or VUU to calculate the relation of observables to the EOS. Calculations show that the density regions covered in heavy-ion collision differs greatly for the hard and soft EOS. However, the difference between the compression energies reached, turns out to be quite small. Therefore, many observables are not very dependent on the EOS. Experimentally the determination of the EOS is difficult.

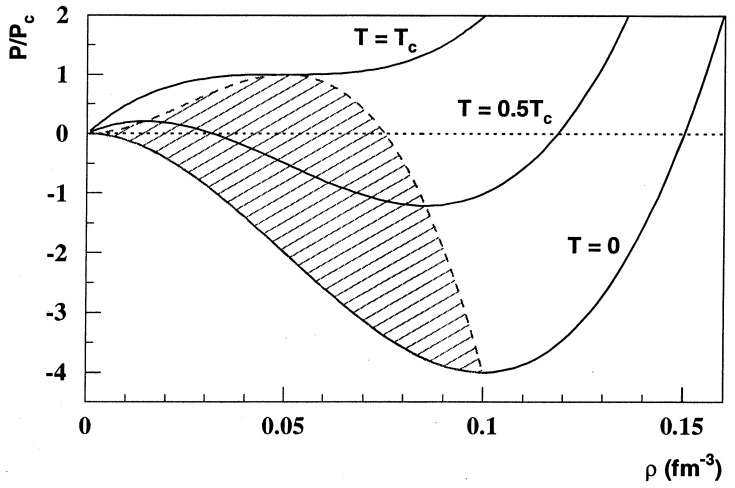

Figure 4.1: *Equation of state for different temperatures, calculated with the Skyrme potential. The normalised pressure P/P_c is plotted versus the nuclear density ρ. P_c and T_c are the maximum pressure and temperature for the coexistence of the liquid and gaseous phase. The hatched area is the spinodal region of instability. Adapted from [17].*

Variables, such as the impact parameter, are difficult to determine and have a large effect on for instance flow, making it difficult to distinguish between the hard and the soft EOS.

With the Skyrme potential it is possible to study the thermodynamic properties of nuclear matter. The density-pressure relation for a Fermi gas of nucleons interacting via a Skyrme potential can be obtained with finite temperature Hartree-Fock theory [16, 17]. In fig 4.1 this relationship is plotted for different temperatures. The normalised pressure P/P_c is plotted versus the nuclear density ρ. P_c and T_c are the maximum pressure and temperature for the coexistence of the liquid and gaseous phases. Normal nuclear matter has zero temperature and pressure (by definition). In fig. 4.1 lines for calculations with $T = 0$, $T = 0.5T_c$, $T = T_c$ are plotted. The hatched area is the *spinodal region of instability*, if a system is in this area, multifragmentation can occur naturally. In this region nuclear matter can not exist as a stable equilibrated system, due to the negative derivatives of the lines of fixed temperature. A system on such a line would simply collapse into a system with a higher density, which is energetically favourable. During this collapse several fragments will be created, which are the condensed IMFs, thus allowing for multifragmentation. During a heavy-ion collision nuclear matter first experiences an increase in temperature and pressure. After this initial phase, the nuclear system cools and decompresses. In this part of the time evolution the system may reach the spinodal region of instability, where the condensation of nuclear matter

leads to multifragmentation.

4.3 Isospin Quantum Molecular Dynamics

In this thesis simulations are described, which were performed with a QMD-type model. It was already discussed in section 4.1, that this microscopic model best suits our purposes, because it includes single-event correlations and fragment formation. The IQMD-model [96] is an extended version of the original QMD model [92], taking into account the isospin asymmetry of the nucleons. Because of this feature, IQMD was preferred over QMD.
In recent years there have been developments in extending QMD with the explicit antisymmetrisation of the nuclear wave function, thus taking into account the Fermionic nature of the nucleons. The development of these models (FMD [97], AMD [98]) is still ongoing and some problems still exist. Firstly it is difficult to antisymmetrise large nuclear systems (A > 40). Secondly the treatment of nucleon-nucleon collisions still offers problems in the dynamical situation of heavy-ion collisions. Furthermore, due to the long time needed to simulate the events it is problematic to gather enough statistics.
The IQMD model is an established model, which on present-day computers calculates events in a reasonable time (for ^{24}Mg+^{27}Al at 45 AMeV several events per second). Therefore, IQMD simulations were used in the analysis of chapter 5.

4.3.1 Theory

In this section the basic framework for QMD is given. It is outside the scope of this thesis to give the complete formalism of QMD, for this the reader is referred to [92].

In QMD each nucleon is represented by a Gaussian wave packet in the Euclidian space,

$$\phi_i(\mathbf{r},t) = \left(\tfrac{2}{L\pi}\right)^{\frac{3}{4}} e^{-(\mathbf{r}-\mathbf{r}_i(t)-\mathbf{p}_i(t)t/m)^2/L} e^{i(\mathbf{r}-\mathbf{r}_i(t))\mathbf{p}_i(t)} e^{-i\mathbf{p}_i^2(t)t/2m}, \tag{4.8}$$

with $\hbar$, $c = 1$. The wave function has two time-dependent parameters, $\mathbf{r}_i(t)$ and $\mathbf{p}_i(t)$, the space and momentum vectors of the nucleon. The width of the wave packet is kept constant at $L = 1.08$ fm^2. In QMD it is assumed that the total wave function of the system is given by the product of the individual wave functions of the participating nucleons of target and projectile ($A_\mathrm{T} + A_\mathrm{P} = N$):

$$\phi = \prod_{i=1}^{N} \phi_i, \tag{4.9}$$

which does not take into account the antisymmetrisation of the wave function. The time evolution of the N-body system is reduced to 6N coupled equations by means of the generalised variation principle. This principle states that a system will develop in time such that the action S is at an extremum, with the action between time t_1 and

t_2 defined as:

$$S = \int_{t_1}^{t_2} \mathcal{L}\left(\mathbf{r}_1, \ldots, \mathbf{r}_N, \mathbf{p}_1, \ldots, \mathbf{p}_N, t\right) \mathrm{d}t, \tag{4.10}$$

where the Lagrangian $\mathcal{L}$ is a function of the space and momentum coordinates of the N particles. To require that S is at an extremum, the derivative is set to 0:

$$\delta S = 0. \tag{4.11}$$

This, in accordance with Hamilton's principle, leads to a set of 6N Euler-Lagrange equations, six for each particles i:

$$\frac{\mathrm{d}}{\mathrm{d}t}\frac{\partial \mathcal{L}}{\partial \dot{\mathbf{r}}_i} - \frac{\partial \mathcal{L}}{\partial \mathbf{r}_i} = 0 \tag{4.12}$$

$$\frac{\mathrm{d}}{\mathrm{d}t}\frac{\partial \mathcal{L}}{\partial \dot{\mathbf{p}}_i} - \frac{\partial \mathcal{L}}{\partial \mathbf{p}_i} = 0. \tag{4.13}$$

For a quantum mechanical system the Lagrangian is defined by:

$$\mathcal{L} = \left\langle \phi \left| i\hbar\frac{\mathrm{d}}{\mathrm{d}t} - H \right| \phi \right\rangle, \tag{4.14}$$

where the Hamiltonian H is the sum of the kinetic and potential energies, T_i and V_{ij} over all particles,

$$H = \sum_i T_i + \frac{1}{2}\sum_{ij} V_{ij}. \tag{4.15}$$

The Lagrangian can now be evaluated:

$$\mathcal{L} = \sum_i \left(\dot{\mathbf{r}}_i \mathbf{p}_i - \frac{1}{2}\sum_j \langle V_{ij} \rangle - \frac{3}{2Lm} \right), \tag{4.16}$$

where the expectation value of the potential energy is defined as:

$$\langle V_{ij} \rangle = \int \mathrm{d}^3\mathbf{r}_1 \mathrm{d}^3\mathbf{r}_2 \left\langle \phi_i \phi_j \left| V(\mathbf{r}_1, \mathbf{r}_2) \right| \phi_i \phi_j \right\rangle. \tag{4.17}$$

Eq. 4.16 can now be inserted in eq. 4.12 and eq. 4.13. It is convenient to transform the coordinate system: $\bar{\mathbf{r}}_i \equiv \mathbf{r}_i + \mathbf{p}_i t/m$, which yields the set of 6N coupled equations defining the time evolution of the system:

$$\dot{\bar{\mathbf{r}}}_i = \frac{\mathbf{p}_i}{m} + \nabla_{\mathbf{p}_i} \sum_j < V_{ij} > \tag{4.18}$$

$$\dot{\mathbf{p}}_i = -\nabla_{\bar{\mathbf{r}}_i} \sum_j < V_{ij} > \tag{4.19}$$

This set of equations is to be solved numerically in QMD.

With the framework of QMD being established, a realistic nucleon potential has to be defined. Note that eq. 4.18 and eq. 4.19 use the expectation value of this potential, which is given by eq. 4.17. Several specific interaction types make up the QMD-potential.
The Skyrme potential, discussed in section 4.2, describes two- and three-body interactions:

$$V^{\text{loc}} = \sum_i \sum_{j>i} t_1 \delta(\mathbf{r}_i - \mathbf{r}_j) + \sum_i \sum_{j>i} \tfrac{1}{6} t_2 \delta(\mathbf{r}_i - \mathbf{r}_j) \rho(\mathbf{r}_{ij}), \tag{4.20}$$

where t_1 and t_2 depend on the equation of state and $\mathbf{r}_{ij} = \frac{\mathbf{r}_i - \mathbf{r}_j}{2}$. Because the Skyrme potential does not include surface effects, the Yukawa potential is also included in the model:

$$V^{\text{Yuk}} = \sum_i \sum_{j>i} t_3 \frac{\exp\left(-\frac{|\mathbf{r}_i - \mathbf{r}_j|}{a}\right)}{\frac{|\mathbf{r}_i - \mathbf{r}_j|}{a}}. \tag{4.21}$$

The parameters t_3 and a are used to obtain the optimal stability for the nucleus. In QMD this is achieved with $t_3 = 15$ MeV and $a = 1.5$ fm [92]. These two potentials are the main contributors to the nucleon potential within the nucleus. Although usually the Coulomb force within the nucleus is small, the trajectories of the fragments after a heavy-ion collision can be influenced by this interaction. Therefore, the Coulomb potential is introduced:

$$V^{\text{Coul}} = \sum_i \sum_{j>i} \frac{Z_i Z_j e^2}{|\mathbf{r}_i - \mathbf{r}_j|}, \tag{4.22}$$

with Z_i and Z_j the atomic numbers of the particles i and j and e the electron charge. A decade ago it was found that an increase in momentum of two colliding nucleons leads to an additional repulsive force between these nucleons [99]. Therefore, a momentum dependent interaction is introduced in QMD:

$$V^{\text{mdi}} = \sum_i \sum_{j>i} t_4 \ln^2 \left(1 + t_5 \left(\mathbf{p}_i - \mathbf{p}_j\right)\right) \delta(\mathbf{r}_i - \mathbf{r}_j), \tag{4.23}$$

where $t_4 = 1.57$ MeV and $t_5 = 5 \cdot 10^{-4}$ MeV^2. The influence of V^{mdi} in the energy domain which is studied in this thesis is limited. For computational purposes it can therefore be advantageous to exclude this potential from the model. The difference between QMD and IQMD is the explicit incorporation of the isospin asymmetry. This is done with a fifth potential added to the model:

$$V^{\text{sym}} = t_6 \frac{1}{\rho_0} \sum_i \sum_{j>i} s_i s_j \delta(\mathbf{r}_i - \mathbf{r}_j). \tag{4.24}$$

The isospin term s_i is -1 for neutrons and $+1$ for protons, ρ_0 is the nuclear density in the ground state and $t_6 = 25$ MeV. The inclusion of V^{sym} influences the stability of the nucleus. Therefore the parameters have to be tuned to obtain an optimal

stability for the nuclei. This changes the values for L in eq. 4.8 to 4.33 fm and a in eq. 4.21 to 0.4 fm [100]. The sum of these potentials is the final potential used in IQMD.

4.3.2 The IQMD program and the cluster algorithm

In the previous section the theory of IQMD model was outlined. In this section some basic aspects of the IQMD program are discussed.
IQMD requires several input parameters. It is possible to choose the EOS for the simulations. Standard options are the aforementioned hard EOS and soft EOS. Furthermore it is possible to exclude the momentum-dependent interactions in order to speed up the calculations. The calculations presented in this thesis were performed with the hard EOS without the incorporation of the momentum-dependent interaction. Next the specifics of the interaction have to be defined. The beam energy E_{beam}, the sizes and atomic numbers of the target (A_{T} and Z_{T}) and projectile (A_{P} and Z_{P}) have to be selected. As default a random impact parameter b is taken conform the geometric probability, but it is also possible to define a specific impact-parameter range. The target and projectile are placed at such a distance that they collide after 15 fm/c and the simulations are stopped after 200 fm/c. This time is sufficiently large that the nucleons are separated in Euclidian space, except for the nucleons which are also close in phase space. These nucleons will be clustered into fragments.

Initialisation

To build a stable nuclear system, it is not sufficient to place the appropriate amount of protons and neutrons randomly in a sphere with the size of a nucleus. Such a nucleus would most likely be a metastable excited state which would decay by emitting particles. Therefore, the initialisation of the target and projectile are essential to the model. During this process isospin asymmetry is taken into account. First the nucleons are placed in a sphere of the radius $R = 1.12A^{1/3}$ fm. This is done randomly, rejecting coordinates which would position the centres of the nucleons closer than $r_{\text{min}} = 1.5$ fm. The inclusion of Fermi motion is done differently in QMD and IQMD. In QMD first the local potential $U(\mathbf{r})$ generated by the other nucleons is determined at the centre of each nucleon. Then the local Fermi momentum is calculated with: $p_{\text{F}}(\mathbf{r}_i) = \sqrt{2mU(\mathbf{r}_i)}$. Finally the momentum of the nucleon is chosen randomly between zero and $p_{\text{F}}(\mathbf{r}_i)$, taking into account that no particles should be closer in phase space than a certain minimum value. In IQMD the Fermi momentum only depends on the ground state density of the nucleus and has no local constraints. The momenta of the nucleons are uniformly distributed within a sphere with radius $p_{\text{F}}(\mathbf{r}_i)$. This can cause nucleons near the surface of the nucleus to evaporate spontaneously. However, this method has the advantage that it makes available the full Fermi energy for the nucleus.

Collisions

Section 4.3.1 deals with the fundamentals of the propagation of the particles. Although the implementation of this theory in the computer simulation is not straightforward, it

is sufficient for understanding IQMD. The interaction between the nucleons in IQMD is in de first place via the discussed potentials and secondly via collisions. Nucleons can collide if the distance between two nucleons becomes less than a certain value. This value depends on the two collision partners (e.g. n-n, p-p, or p-n) and their relative momenta. However, IQMD does not take into account medium-density effects. The cross sections are experimentally determined for free particles. Collisions can either be elastic or inelastic (particle production), where several elastic channels are taken into account. The decision which exit channel is occupied is done stochastically, with a weight relative to the cross section of the specific channel. This extends to the elastic collisions, where the angle of the outgoing particle is determined also stochastically in such a way that the angular distribution is in agreement with experimental data on free particles. After each collision the exit channels are checked for the Pauli blocking and, if necessary, the collisions are reversed.

Clustering

The IQMD model itself does not include fragment formation. The output of the model is restricted to the phase space coordinates of all the participant nucleons (at 200 fm/c). After the simulation is stopped, the output is clustered with a minimum-spanning-tree method. All nucleons within a radius $r_{\min} = |\mathbf{r}_i - \mathbf{r}_j|$ are considered to form a fragment. This method does not incorporate the momenta of the nucleons, although nucleons which at this time are clustered in coordinate-space are also likely to be clustered in phase space. The cluster algorithm was used with $r_{\min} = 3$ fm, however, variation of this value shows little influence on the outcome of the clustering.

4.3.3 Results for ^{24}Mg+^{27}Al at 45 and 95 AMeV

In this chapter some global results of IQMD are presented. These results can be divided in two categories. First the time evolution of an IQMD event is studied. In IQMD it is possible to look at a heavy-ion collision at any given moment in time. This is of course only possible in simulations, and gives the opportunity to study the time characteristics of an event. In this part the implication of the cluster algorithm is also discussed.
The second part of this section presents some distributions simulated with IQMD which are directly related to the geometry of the Huygens detectors. These distributions are used to validate statements made in the previous chapters about the expected experimental particle distributions.

Time evolution and clustering

To gain insight in the dynamics of a heavy-ion collision, this section discusses some features of the time evolution in IQMD. Fig. 4.2 shows the time evolution of a simulated IQMD event for a beam energy of 45 AMeV. The event is projected onto the reaction plane, defined by the vector connecting the centre of the colliding nuclei and the beam

is sufficient for understanding IQMD. The interaction between the nucleons in IQMD is in de first place via the discussed potentials and secondly via collisions. Nucleons can collide if the distance between two nucleons becomes less than a certain value. This value depends on the two collision partners (e.g. n-n, p-p, or p-n) and their relative momenta. However, IQMD does not take into account medium-density effects. The cross sections are experimentally determined for free particles. Collisions can either be elastic or inelastic (particle production), where several elastic channels are taken into account. The decision which exit channel is occupied is done stochastically, with a weight relative to the cross section of the specific channel. This extends to the elastic collisions, where the angle of the outgoing particle is determined also stochastically in such a way that the angular distribution is in agreement with experimental data on free particles. After each collision the exit channels are checked for the Pauli blocking and, if necessary, the collisions are reversed.

Clustering

The IQMD model itself does not include fragment formation. The output of the model is restricted to the phase space coordinates of all the participant nucleons (at 200 fm/c). After the simulation is stopped, the output is clustered with a minimum-spanning-tree method. All nucleons within a radius $r_{\min} = |\mathbf{r}_i - \mathbf{r}_j|$ are considered to form a fragment. This method does not incorporate the momenta of the nucleons, although nucleons which at this time are clustered in coordinate-space are also likely to be clustered in phase space. The cluster algorithm was used with $r_{\min} = 3$ fm, however, variation of this value shows little influence on the outcome of the clustering.

4.3.3 Results for ^{24}Mg+^{27}Al at 45 and 95 AMeV

In this chapter some global results of IQMD are presented. These results can be divided in two categories. First the time evolution of an IQMD event is studied. In IQMD it is possible to look at a heavy-ion collision at any given moment in time. This is of course only possible in simulations, and gives the opportunity to study the time characteristics of an event. In this part the implication of the cluster algorithm is also discussed.
The second part of this section presents some distributions simulated with IQMD which are directly related to the geometry of the Huygens detectors. These distributions are used to validate statements made in the previous chapters about the expected experimental particle distributions.

Time evolution and clustering

To gain insight in the dynamics of a heavy-ion collision, this section discusses some features of the time evolution in IQMD. Fig. 4.2 shows the time evolution of a simulated IQMD event for a beam energy of 45 AMeV. The event is projected onto the reaction plane, defined by the vector connecting the centre of the colliding nuclei and the beam

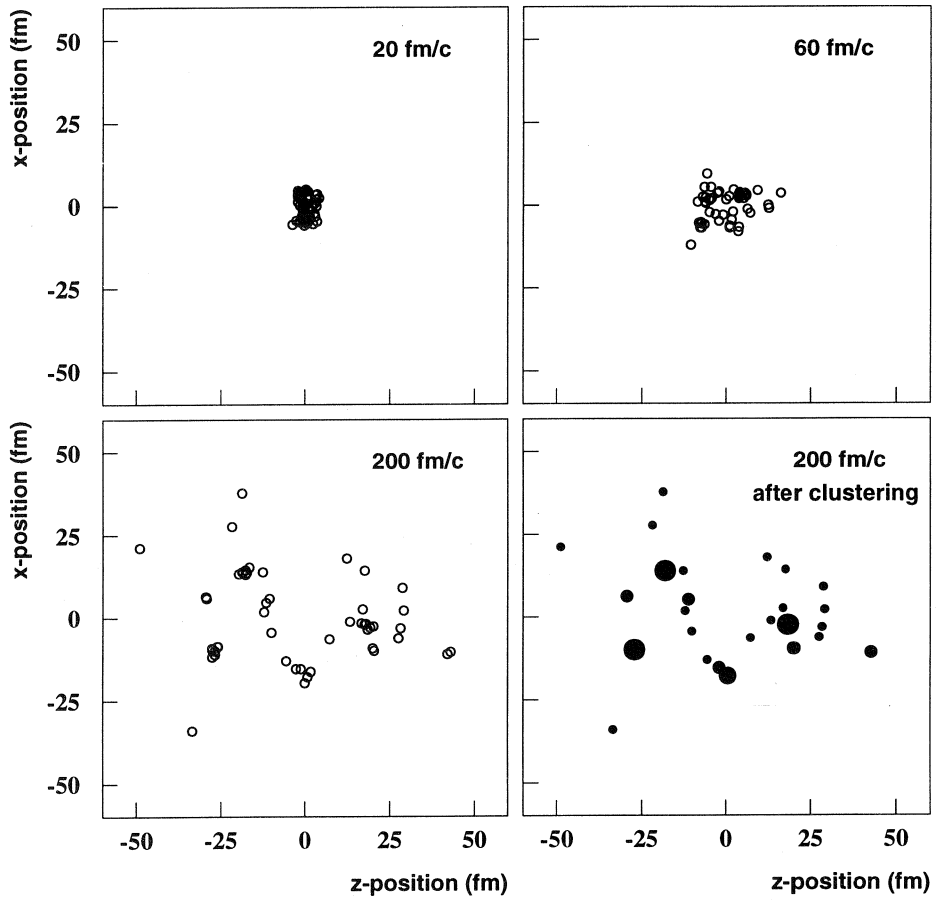

Figure 4.2: *Simulated IQMD event for $E_{\text{beam}} = 45$ $AMeV$ with an impact parameter $b = 3.1$ fm. The x-position is plotted versus de z-position, which defines the reaction plane. The simulation time is indicated in the top-right corner. At 15 fm/c the two nuclei collide. The bottom right figure shows the result after clustering. The size of the markers indicates the mass of the cluster.*

direction. The impact parameter is 3.1 fm. The simulation time is indicated in the top-right corner of each figure. At 15 fm/c the two nucleons collide and after 200 fm/c the simulation is stopped. The bottom left figure shows the result of IQMD at this point. In this figure it is visible that some of the nucleons are close together. These nucleons have formed fragments or are the residue of the primary nuclei. The bottom right figure shows the results of the minimum-spanning-tree clustering method. Different fragment masses are qualitatively represented by four different sizes of the marker. Fig. 4.2 gives us a picture of the evolution of the colliding systems in IQMD, be it

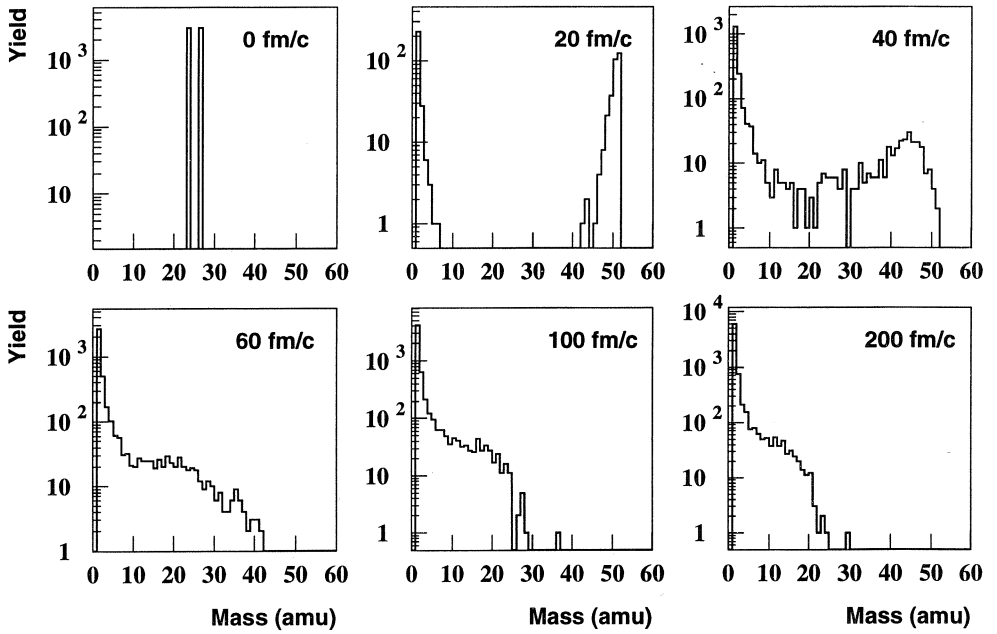

Figure 4.3: *Time evolution in IQMD of clusters defined by the minimum-spanning-tree method. Before the collision at 15 fm/c only two clusters exist; the original nuclei. After the collision the system evolves from a hot, dense state to a system consisting of many separate light particles.*

somewhat qualitatively. In order to quantify the time evolution, 3000 events with a minimum-bias impact parameter where simulated. The cluster algorithm was applied on each event at different times. This is shown in fig 4.3. Again the IQMD-time is indicated in the top-right corner. At $t = 0$ fm/c two clusters are present, the target and the projectile. At 5 fm/c after the collision ($t = 20$ fm/c) almost all nucleons are clustered into one composite system, except for a few very light particles. Note that the cluster algorithm does not take into account the momentum-space coordinates of the nucleons. Therefore the particles in the clusters do not have to be bound in this 'compound' system (and in fact at this point in time they are not). After another $t = 20$ fm/c particles are rapidly separating from the 'compound' system. Also larger fragments are being formed. At this point the nucleons are still confined to a small area in coordinate space, therefore the nucleons within a cluster might be separated in momentum space. At $t = 60$ fm/c the shape of the distribution already resembles the final shape at the end of the simulation (200 fm/c), although some fragments are still excited and will decay further. The distributions at 100 and at 200 fm/c are very similar, indicating that at 100 fm/c the system is already stabilised and it is valid to stop the simulation at 200 fm/c. It also shows that the cluster algorithm yields a stable solution.

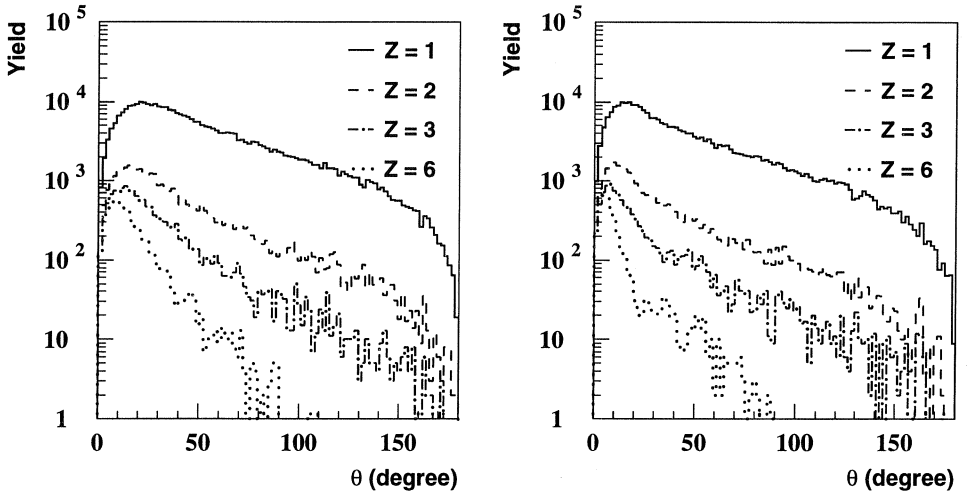

Figure 4.4: *Polar angle distribution of IQMD in the laboratory frame for 45 A MeV on the left-hand side and 95 A MeV on the right-hand side. The legend in the top-right shows the atomic number of the distributions.*

IQMD laboratory distributions

In this section the one-particle distributions from IQMD in the laboratory system are related to the Huygens detector set-up (chapter 2) and some of the distributions measured with the Huygens detector (chapter 3). In fig. 4.4 the polar angle distributions in the laboratory system calculated by IQMD are shown. The left figure contains results of simulations at $E_{\text{beam}} = 45$ AMeV, the right figure are results of simulations at $E_{\text{beam}} = 95$ AMeV. The simulated data is shown for fragments with atomic number 1, 2, 3 and 6. An energy cut-off of 5 AMeV was imposed on the simulations, to give a rough comparison with the experiment. This figure shows that the IMFs are predominantly present in the forward region. In the Huygens set-up this region is covered by the TPC and the MUR, which are able to identify the IMFs. In the backward region the multiplicity is very low and the particles are predominantly protons, In this region the CIW is used as a multiplicity counter.

In order to verify the energy coverage of the TPC, the energy distribution according to IQMD is studied. Fig 4.5 shows the energy distributions, divided into the two main subdetector groups of the Huygens detector array. Again the 45 AMeV data is shown on the left and the 95 AMeV on the right-hand side. In the upper panel the polar angle in the laboratory system is smaller then 30°. The lower panel shows data in the region between 30° and 90° polar angle in the laboratory system. The simulations of the data between 30° and 90° polar angle show the particles which in the Huygens detector would be identified by the sideward plastics. These subdetectors can identify $Z = 2$ and higher Z up to 125 AMeV. The distributions show that this enables us to

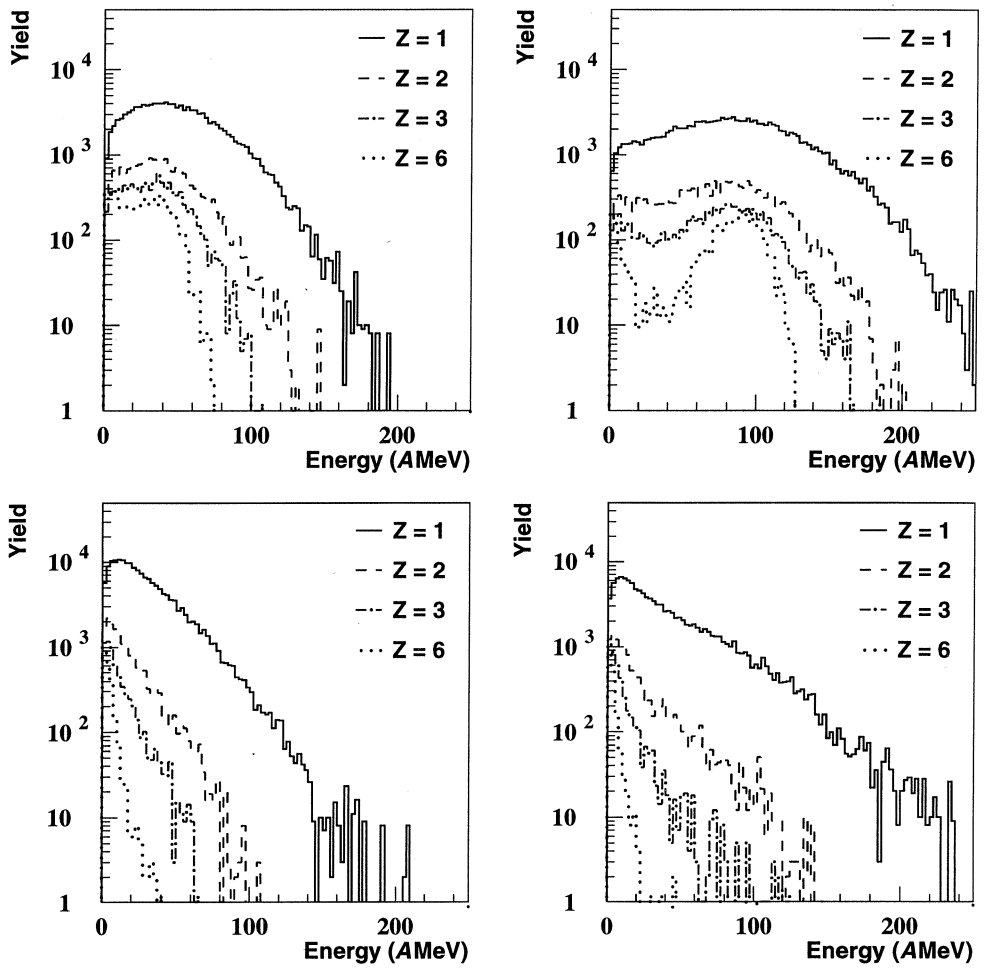

Figure 4.5: *Energy distribution of IQMD in the laboratory system for 45 AMeV on the left-hand side and 95 AMeV on the right-hand side. The top panels are for a polar angle in the laboratory system smaller then 30° and the bottom panels for a polar angle in the laboratory system between 30° and 90°.*

see all IMFs. In the forward region fragments with energy higher than 36 AMeV are no longer identified in the TPC but in the MUR (in conjunction with the forward plastics, see section 3.2). In this region the distribution shows a clear maximum at the beam energy. Especially for the heavy fragments at 95 AMeV a pronounced dip in the distributions is present. It was already argued that the dip in the experimental data of fig. 3.9 is not caused by detector effects, but is due to the physics of the collision, which is confirmed by IQMD.

5

Results and discussion

In this chapter the analysis of the experimental data is presented and compared to simulations. This makes it possible to draw conclusions about the reaction dynamics of heavy-ion collisions of small systems. This is the first time that the collisions of these small systems have been investigated on such an extensive scale. The reaction is studied on two basic levels. First the collective effects of ^{24}Mg+^{27}Al are focussed on, the event plane is reconstructed and flow of fragments within the reaction plane is studied. The inherent inaccuracy of the event-plane reconstruction is an intrinsic problem in the study of these effects. This is especially the case for small systems, were the number of fragments, which can be used to reconstruct the reaction plane is small. Therefore, a second method was used to study the reaction, which does not need a reaction plane to be reconstructed, but uses the azimuthal-correlation between emitted fragments. This method was previously used to show the characteristics of a (thermalised) rotating source at mid-rapidity [101, 102, 103, 104, 105]. The data presented here does not show such a source, but, in conjunction with the polar-angle distributions, is evidence of dynamic IMF production.

The analysis of the data is restricted to IMFs, which for the small system under investigation have been defined as $2 \leq Z_{\mathrm{IMF}} \leq 8$. Protons are not measured by the TPC over a sufficiently large energy range to justify an analysis. Furthermore, heavier fragments were not measured in a substantial amount. Therefore, only the IMFs feature in this chapter. The velocity (in the beam direction) of the particles is discussed in terms of the rapidity Y:

$$Y = \tfrac{1}{2} \ln \left(\frac{E + p_z}{E - p_z} \right), \tag{5.1}$$

where E and p_z are the energy and the z-momentum of the particle in the centre-of-

mass frame of the colliding nuclei. Rapidity differences are Lorentz-invariant quantities. Because ^{24}Mg+^{27}Al is an almost symmetric system, $Y_{\mathrm{target}} \simeq -Y_{\mathrm{proj}}$, the mid-rapidity region is defined as $|Y_{\mathrm{mid}}| \leq \frac{1}{2} Y_{\mathrm{proj}}$.

Before the study of the reaction mechanism is described, section 5.1 discusses the impact-parameter determination of the data. It is known that the physics of heavy-ion collisions is strongly influenced by the impact parameter. Because not much of the effectiveness of the impact-parameter selection on small systems is known, IQMD and the GEANT detector simulation were used to study this for small systems. It is concluded that only the mid-central impact-parameter class can be used in the analysis. Section 5.2 then focusses on the collective motion of IMFs in the reaction plane. It will be shown that the magnitude of the collective in-plane flow at 45 AMeV is substantially larger than at 95 AMeV, in accordance with similar systems in literature. This section includes an elaborate study of the reaction-plane reconstruction. In section 5.3 the azimuthal correlations are used in conjunction with the polar-angle distributions to show that the IMF production in these small systems is a dynamic process.

5.1 Impact-parameter selection

The physics of heavy-ion collisions is strongly influenced by the amount of overlap between the two nuclei. This quantity is described by the impact parameter, b, which is defined as the distance between the centres of the colliding nuclei. Several methods have been proposed to measure b. These methods are generally based on the sum over one-body observables in an event, such as transverse momentum $|\mathbf{p}_{\mathrm{t}}|$, detected energy E_{det} or charged particle multiplicity N_{c} (see [106, 107] and references therein). Simulations with IQMD combined with the GEANT detector simulation do not show large differences in the accuracy with which b can be determined from $|\mathbf{p}_{\mathrm{t}}|$, E_{det} or N_{c}. For our data the charged particle multiplicity was used for the impact parameter determination. It is assumed that N_{c} depends monotonically on the impact parameter [107, 108]:

$$\hat{b}(N_{\mathrm{c}}^{\mathrm{m}}) = \frac{b}{b_{\mathrm{max}}} = \left(\int_{N_{\mathrm{c}}^{\mathrm{m}}}^{\infty} P(N_{\mathrm{c}}) \mathrm{d}N_{\mathrm{c}} \right)^{\frac{1}{2}}, \tag{5.2}$$

with $\hat{b}$ the impact parameter as a fraction of the maximum impact parameter, b_{max}, $N_{\mathrm{c}}^{\mathrm{m}}$ the charged particle multiplicity for which the impact parameter is to be determined and $P(N_{\mathrm{c}})$ the measured probability distribution of N_{c}. It is assumed that the two nuclei are classical spheres, with b_{max} the sum of the radii (for ^{24}Mg+^{27}Al , $b_{\mathrm{max}} = 6.6$ fm). Fig. 5.1 shows $P(N_{\mathrm{c}})$ in the Huygens detectors for the 45 and 95 AMeV data. In the 95 AMeV data the very low multiplicities are suppressed by the trigger. This data set was not taken with a minimum-bias trigger, but with the requirement that either in the forward scintillators or in the sideward scintillators two or more hits were registered. The 45 AMeV data was taken with a minimum bias trigger, i.e. a single hit in one of the plastic scintillators ($\theta_{lab} > 10°$) and shows the distribution expected in heavy-ion

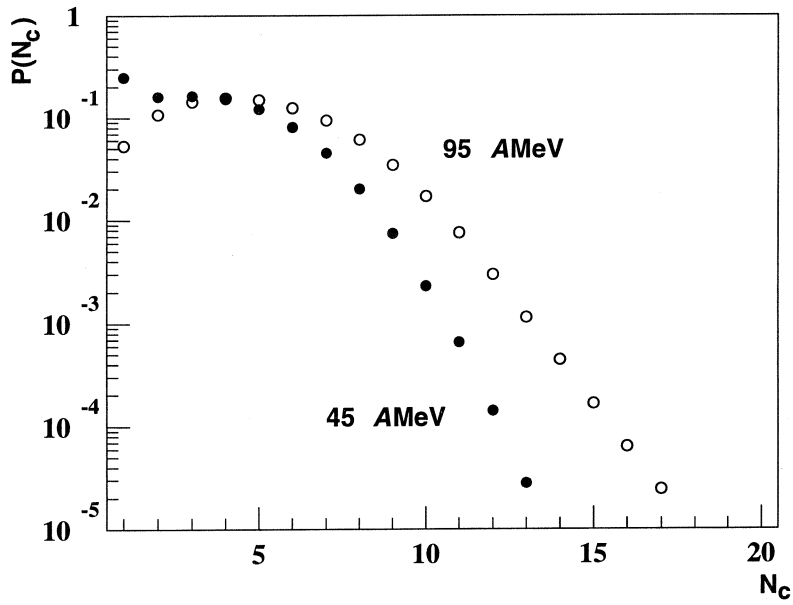

Figure 5.1: *The measured charged particle multiplicity, $P(N_c)$ in the Huygens detectors for 45 and 95 AMeV beam energy.*

collisions: a structureless plateau and a (near) exponential slope at high multiplicities. Because of the small number of participating nucleons the exponential decrease starts at low multiplicities. To compensate for the trigger effects, the structureless plateau in $P(N_c)$ for both distributions was extended to low multiplicities. With this assumption, different impact-parameter classes can be defined using eq. 5.2. Three different classes are defined, peripheral for $\hat{b} > 0.7$, mid-central for $0.35 > \hat{b} > 0.7$ and central for $\hat{b} < 0.35$. For the measured multiplicity distribution this results in a definition for mid-central events for 45 AMeV of $2 < N_c < 6$. For 95 AMeV mid-central is defined by $3 < N_c < 7$. Higher multiplicities are central and lower multiplicities are peripheral. Because of the low multiplicity ($N_c \leq 3$), peripheral events are not used in the analysis.

A similar analysis for the impact parameter can be performed on IQMD data, which is processed by the GEANT detector simulation. It should be noted that IQMD underestimates fragment formation, while proton and neutron yields are overestimated. These effects are caused by the evaporation of protons and neutrons from the surface of 'stable' nuclei, as discussed in section 4.3.2. This effect leads to an increased multiplicity for all impact parameter classes. Nevertheless, the analysis can give an indication of the accuracy of the definition of the impact-parameter classes. In fig. 5.2 the impact parameter is plotted of an IQMD simulation with GEANT for the three classes at 95 AMeV beam energy. The results are similar for 45 AMeV. The yield of the distributions are with a minimum bias trigger. The mean value and the RMS

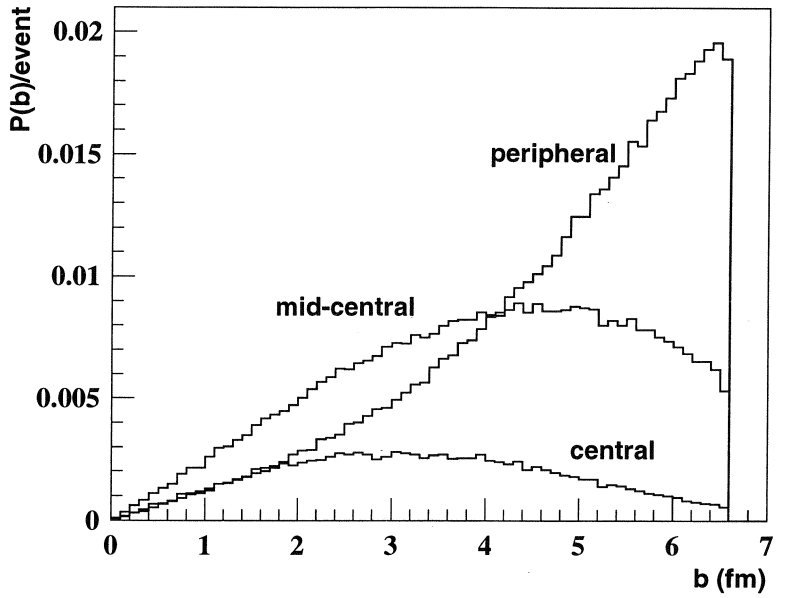

Figure 5.2: *Impact-parameter distribution for $^{24}Mg+^{27}Al$ at 95 AMeV for different impact-parameter classes generated by IQMD and filtered by GEANT. The peripheral data has a mean value of 4.8 fm with a RMS of 1.4 fm, for mid-central the mean is 4.0 fm with a RMS of 1.5 fm and the central selection has a mean of 3.3 fm with a RMS of 1.5 fm.*

for the peripheral, mid-central and central events are 4.8 ± 1.4 fm, 4.0 ± 1.5 fm and 3.3 ± 1.5 fm, respectively. The shapes of the distributions show the (in)accuracy by which the impact parameter can be determined. Therefore, these classes should merely be seen as an indication for the selected impact-parameter range. It should be noted that by selecting from these distributions events with a number of IMFs, a new implicit impact-parameter selection is made, which will result in an even more similar event selection for the impact-parameter classes.
In this chapter the event class 'mid-central' is used in the analysis. Fig. 5.2 shows that the central class is heavily polluted by mid-central events. Therefore, it is not possible to draw conclusions about very central collisions. The peripheral events are, like the mid-central events, reasonably well defined. However, due to the small charged-particle multiplicity, it is not possible to do a useful analysis on these events.

5.2 Collective motion

The collective motion of matter in nuclear collisions is deemed to be one of the primary observables to extract information on the EOS. During heavy-ion collisions the nuclear

matter experiences two, opposite, forces. Firstly, the nuclear material is attracted via the nuclear mean-field potential. This force is responsible for the stability of the elements. Secondly, the nucleon-nucleon interaction results in a repulsive force on the colliding systems. At low beam energies ($E_{\mathrm{beam}} \lesssim 40$ AMeV) the nuclear mean-field potential is the strongest, at higher beam energies ($E_{\mathrm{beam}} \gtrsim 100$ AMeV) the nucleon-nucleon interaction becomes the dominant force. Both processes cause a sideward flow of fragments within the reaction plane, which is called *directed in-plane flow.* In the intermediate-energy region, the interest of experimental groups has been focussed in particular on the balancing energy, E_{bal}. This is the beam energy where the attractive mean field potential and the repulsive nucleon-nucleon interaction cancel. Although the magnitude of the directed in-plane flow was found to depend on the mass of the emitted fragment, E_{bal} is the same for all fragments [109]. Furthermore, both experiment and simulation show that E_{bal} is proportional to $A^{-1/3}$, where A is the combined mass of the colliding system [11, 110]. In this section the directed flow is studied at the two incident energies. Although it is not possible to extract E_{bal}, it will be shown that the directed flow at 95 AMeV is substantially smaller than the flow at 45 AMeV, in agreement with expectations. For this study, the reaction plane itself has to be reconstructed. Methods to perform this reconstruction have an intrinsic error, which is inversely correlated to the number of fragments in an event. For the small system described in this thesis, IQMD and the GEANT detector-simulation program were used to study the event-plane reconstruction to show that the above-mentioned processes can be observed with the Huygens detectors.

5.2.1 Event-plane reconstruction

The event plane is defined by the vector connecting the two centres of the colliding nuclei at the time of the collision and the beam direction. In an experiment this is an unknown variable and, therefore, needs to be reconstructed from the observables. In simulated events, this variable is known and the effectiveness of the event-plane reconstruction can be studied. Three methods can be used to perform the reconstruction, the kinetic flow-tensor method [111], the transverse-momentum analysis [112] and the azimuthal-correlation method [113]. In this section the different methods are described briefly and the results are compared. The comparison is done using IQMD events for the ^{24}Mg+^{27}Al system at 45 and 95 AMeV before and after the simulation of the detector response. In this section all calculations are performed in the centre-of-mass frame of the colliding system.

The kinetic flow-tensor method constructs, for the determination of the reaction plane, the kinetic sphericity tensor F:

$$F_{ij} = \sum_{\nu=1}^{N} \omega_\nu p_{i\nu} p_{j\nu}, \tag{5.3}$$

with i, j running from 1 to 3, N the number of particles in an event, ω_ν a weight factor for each particle and $p_{i\nu}$ the i^{th} component of the momentum of particle ν. For the weight factor usually $\frac{1}{2m_\nu}$ is taken, with m_ν the mass of the particle, this method will

be referred to as STM. For this study the method was also tested with a weight factor of 1, which will be called ST1. In heavy-ion collisions F defines a volume in space, which in general is shaped like a *cigar*. Because the tensor is symmetric, diagonalisation of F yields three real eigenvalues f_i, which are ordered such that $f_3 \lesssim f_2 < f_1$. The eigenvector associated with the largest eigenvalue, $\mathbf{e}_1$, defines the largest component of the collective flow. This component, the directed in-plane flow, spans the reaction plane with the beam direction and thus defines the reaction plane.

In the transverse-momentum analysis (TMA) only the direction of the particles perpendicular to the beam axis are considered. The reaction plane is fixed by the beam direction and the $\mathbf{Q}$ vector, which is defined by:

$$\mathbf{Q} = \sum_{\nu=1}^{N} \omega_\nu \mathbf{p}_\nu^\perp, \tag{5.4}$$

with the sum over all particles in an event, $\mathbf{p}_\nu^\perp$ the momentum component perpendicular to the beam axis and ω_ν the weight factor which is $+1$ for particles with $Y_\nu > 0$ and -1 for $Y_\nu < 0$. This method assumes that the flow in the forward region is associated, via momentum conservation, with flow in the opposite direction in the backward region. The weight factor assures that both directions are summed with the same sign.

STM, ST1 and TMA all explicitly use and require the directed in-plane flow for the reconstruction of the reaction plane. The azimuthal-correlation method (ACM) does not use this feature but merely requires that the particles are preferably emitted within (close to) the reaction plane. This method again only uses the momenta of the particles perpendicular to the reaction plane. The azimuthal angle of the event plane is reconstructed using a test reaction plane. The deviation, D^2, of all momenta relative to this test plane is defined in terms of the slope, a, of the projection of the test plane in the x-y plane:

$$D^2 = \sum_{\nu=1}^{N} p_{x\nu}^2 + p_{y\nu}^2 - \frac{(p_{x\nu} + p_{y\nu})^2}{1 + a^2}, \tag{5.5}$$

with the sum being over all particles in an event and p_x, p_y the components of the momenta perpendicular to the beam. The real reaction plane is found by minimising D^2:

$$\frac{\mathrm{d}D^2}{\mathrm{d}a} = 0 \tag{5.6}$$

Note that ACM should not be confused with the azimuthal-correlation function described in section 5.3, which does not require an event-plane determination. The two methods regrettably share the same name in literature.

To avoid a strong auto-correlation between the angle of the particle and the angle of the reaction plane, the reconstruction of the reaction plane should be performed for

each particle individually, without using the information of the particle of interest. So in fact the sum over all particles, N, used in all three methods should be replaced with the sum over $N-1$. The result of this is that for each event N different reaction planes are defined. The omission of the particle of interest for the reaction-plane determination has, besides the reduced statistics, another negative effect on the event-plane reconstruction. Assuming that all particles are detected, the sum of the momenta should be equal to zero. Leaving one fragment out of the summation results in a violation of momentum conservation. To compensate for this, all particles are boosted by a weighted velocity, $\mathbf{v}_b$, related to the momentum of the particle of interest, $\mathbf{p}_{poi}$ [114]:

$$\mathbf{v}_b = \frac{\mathbf{p}_{poi}}{m_{sys} - m_{poi}}, \tag{5.7}$$

with m_{sys} the mass of the complete system and m_{poi} the mass of the particle of interest. Because the sum of the z-momenta in the experimental data already show a deviation from zero, this method was only applied to the transverse components of the momentum.

All four described methods, STM, ST1, TMA and ACM have been used to reconstruct the event plane on simulated data of mid-central events. Fig. 5.3 shows the results of this study. The plot on the left shows the distributions for the difference between the reconstructed reaction plane and the real reaction plane for TMA and ACM of ^{24}Mg+^{27}Al at 45 AMeV for IQMD data. All distributions show this shape and only differ in the width of the distribution. The table on the right of fig. 5.3 gives the RMS values of the different distributions. For all simulated data sets ACM gives the best results, although the differences, particularly after the detector simulations, are quite small. Therefore, ACM was used to reconstruct the reaction plane of the measured data. The influence of the beam energy and the detector on the distributions will be discussed shortly.

In the comparison above only the smallest angle between the calculated reaction plane and the real reaction plane was used. In fact this quantity is what can be measured experimentally. However, to do a flow analysis it is also necessary to determine the orientation of the reaction plane, i.e. whether the projectile passes the target on the left or on the right-hand side. This can not be done unambiguously. It is, however, possible to align the reaction plane for all events. For this the angle of the directed flow is used. Because it is expected that for ^{24}Mg+^{27}Al both at 45 and 95 AMeV the system experiences a negative flow, it is defined as such. If the calculated flow in an event is found to be positive, the reaction plane is rotated by 180°.
In fig. 5.4a the results of the event-plane analysis with ACM for IQMD data are shown for mid-central events. For this study all fragments with $1 \leq Z \leq 8$ were used. The 45 AMeV data shows a slightly better determination of the reaction plane than the 95 AMeV data. At 95 AMeV the number of light fragments is substantially higher than at 45 AMeV . These fragments are in general emitted more isotropically than larger fragments, which makes it more difficult to determine the reaction plane. Fig. 5.4b

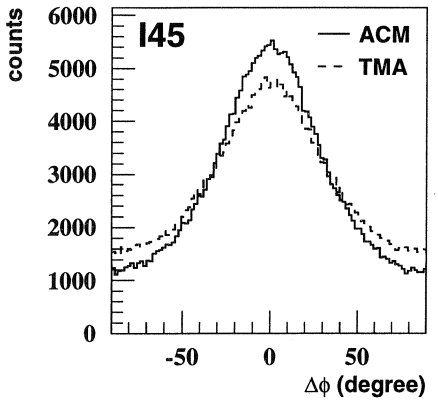

Table: RMS of $\Delta\phi$ distributions

	I45	I95	G45	G95
STM	41.5	45.1	46.2	48.4
ST1	41.5	44.4	46.8	48.5
TMA	43.0	44.8	46.7	48.4
ACM	39.8	43.4	45.8	48.2
error	0.1	0.1	0.3	0.1

Figure 5.3: *On the left: the distributions for the difference in azimuthal angle between the reconstructed reaction plane and the real reaction plane using the transverse-momentum analysis and the azimuthal-correlation method at 45 A MeV for IQMD data. On the right: RMS of the distributions of the difference between the reconstructed event-plane and the real event plane for the four described methods, the sphericity flow-tensor method with the mass (STM) and with 1 (ST1) in the weight factor, the transverse-momentum analysis (TMA) and the azimuthal-correlation method (ACM). The last row indicates the error in the values of that column. The methods were tested at 45 and 95 A MeV before and after the detector simulation, denoted respectively with* I *and* G. *All results are for mid-central events.*

shows the results for mid-central events after the IQMD events are processed by the detector simulation. Because in the experimental data only $2 \leq Z \leq 8$ are identified in the TPC and $Z = 1$ is only seen in the MUR, the analysis was restricted to these fragments. The reaction-plane determination after the detector simulation is considerably less accurate than before this simulation. This is mainly due to the reduction of the acceptance in the backward hemisphere and close to the beam. Again the 45 AMeV data shows a slightly better determination than the 95 AMeV data. Most importantly, from fig. 5.4b it can be concluded that it is possible to determine the reaction plane with the experimental data from the Huygens detectors. It should be noted that the production cross sections for the various IMFs in IQMD is underestimated. Therefore, the reaction-plane determination in the experimental data is expected to be better than shown by the IQMD simulations.

5.2.2 Directed in-plane flow

After the study of the reaction-plane reconstruction, this information can be used to calculate the directed in-plane flow. The influence of the inaccuracy of the reaction plane on the flow must be looked at carefully to justify conclusions from the experi-

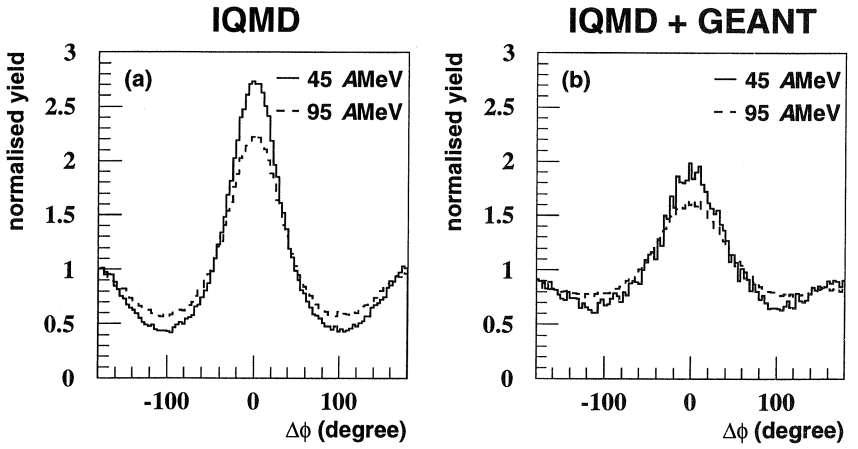

Figure 5.4: *The angle difference between the real reaction plane and the reaction plane determined with ACM for mid-central events. On the left-hand side the results for IQMD data, on the right-hand side the results after the GEANT program was used to simulate the detector effects on the IQMD data.*

mental data. The flow analysis will be used to show a difference in magnitude between the directed in-plane flow at 45 and 95 AMeV. With only these two data points it is not possible to extract E_{bal}. However, this quantity has already been measured for the system ^{20}Ne+^{27}Al and has a value of 111 ± 10 AMeV [11]. Assuming that E_{bal} depends on the mass of the system with $A^{-1/3}$, E_{bal} for ^{24}Mg+^{27}Al would be 114 ± 10 AMeV. It will be shown that our measurements are in agreement with this value.

It is known that although IQMD shows directed in-plane flow, and also the disappearance of flow, the value of E_{bal} in IQMD is in general much larger than the experimentally measured value [14, 41, 115]. The simulations presented in this section support this for the system ^{24}Mg+^{27}Al. It is, therefore, not possible to use IQMD to determine the EOS. However, the IQMD calculations are still valuable to prove that directed in-plane flow can be measured with the Huygens detectors.

To calculate the magnitude of the directed in-plane flow, the flow parameter F is defined:

$$F = \frac{\mathrm{d} < p_{x^*} >}{\mathrm{d}(Y/Y_{\mathrm{proj}})}, \tag{5.8}$$

with p_{x^*} the component perpendicular to the beam of the projection of the momentum on the reaction plane and Y/Y_{proj} the rapidity in the centre of momentum frame normalised to the projectile rapidity (as defined at the beginning of the chapter). The value F has to be calculated around mid-rapidity, usually between $-\frac{1}{2}Y_{\mathrm{proj}}$ and $\frac{1}{2}Y_{\mathrm{proj}}$, although this domain may vary in the region where p_{x^*} vs. Y can be fitted with a

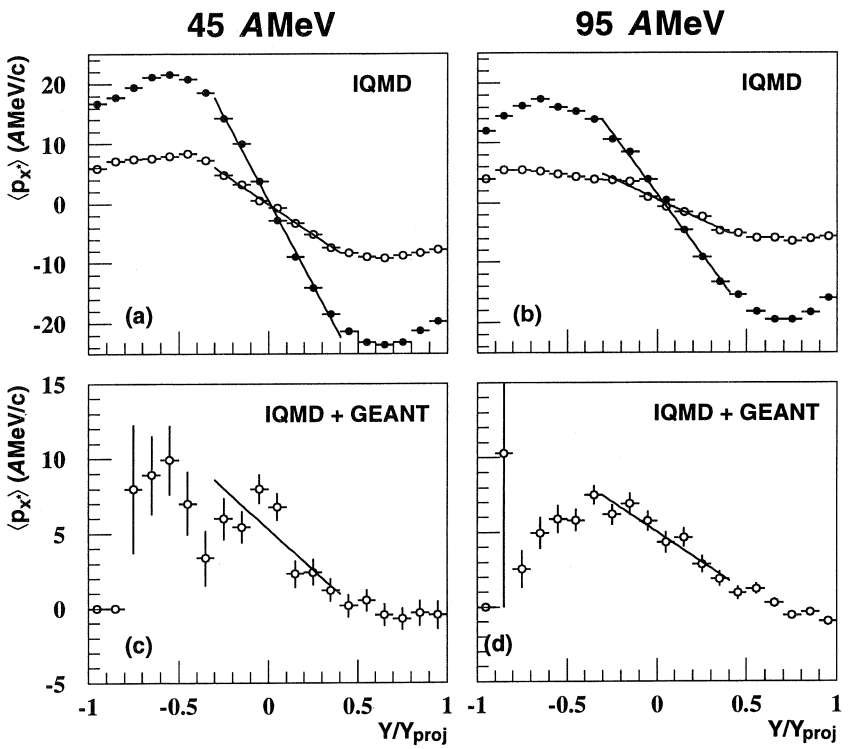

Figure 5.5: *Average in-plane transverse momentum as a function of the rapidity normalised to the projectile rapidity. The figures on the left are for 45 AMeV data, on the right for 95 AMeV. All data is mid-central. Figures (a) and (b) are the results for IQMD events with the projection on the real reaction plane (filled circles) and on the reconstructed reaction plane with the ACM (open circles). The figures (c) and (d) show the results after the IQMD events are processed by the detector simulation, with the reconstructed reaction plane. The lines are fits of a straight line and are used to calculate the flow (see text).*

straight line. Fig. 5.5 show the results of the flow calculations on simulated events in the mid-central impact-parameter class. In (a) and (b) the momentum projections of IQMD events on the real reaction plane are shown with filled circles. These graphs show the real directed in-plane flow. The fits are also drawn in the figure, for 45 AMeV the flow is -56.5 ± 1.1 AMeV and for 95 AMeV it is -41.2 ± 1.4 AMeV. These values indicate that E_{bal} in IQMD is much greater than the 114 ± 10 AMeV from literature. In (a) and (b) also the momentum projections are shown for the same events, with the reconstructed reaction plane (open circles). The uncertainty in the reaction-plane reconstruction reduces the measured flow by about a factor of three, but retains the ratio between 45 and 95 AMeV. The values for the fit for these distributions are

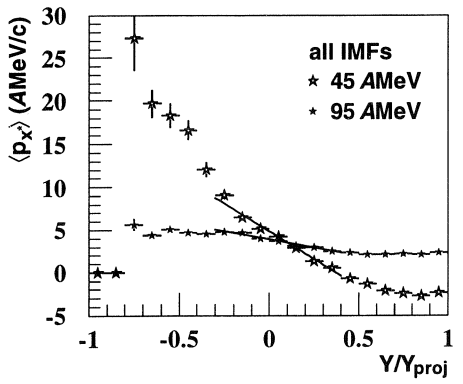

Table: flow values in AMeV/c

	45 AMeV	95 AMeV
all IMFs	−12.9(1.1)	−3.2(1.2)
$Z = 2$	−10.4(1.5)	−3.3(1.4)
$Z = 3$-4	−19.9(1.7)	−4.7(2.5)
$Z = 5$-8	−33(4)	−6.3(3.7)

Figure 5.6: *On the left, as in fig. 5.5 for measured data. The results of the fit are shown in the table on the right. Also the results for the different Z-classes are shown.*

-19.9 ± 0.6 AMeV for 45 AMeV and -12.9 ± 2.1 AMeV for 95 AMeV. Figures (c) and (d) show the momentum projections after the IQMD events have been processed by the detector simulation. Again these are projections on the reconstructed event plane. The values for the flow are for 45 AMeV -12 ± 3 AMeV and for 95 AMeV -7.6 ± 2.1 AMeV. Also after the detector simulation the ratio between the data sets are retained (within the error). Fig. 5.5c and 5.5d show that directed in-plane flow can be determined with the Huygens detectors using the procedures described above.

Fig. 5.6 gives the results of the directed in-plane flow measurements of the Huygens data of mid-central events. On the left-hand side the results of the momentum projection on the reconstructed reaction plane is shown for all IMFs. Similar to the IQMD data after the GEANT simulations, the measurements show a positive offset of $< p_{x^*} >$, which is due to the acceptance of the Huygens detectors. The simulations have shown that, despite this offset, the flow value F can still be used to measure directed in-plane flow. Clearly the flow is substantially reduced at 95 AMeV as compared to 45 AMeV. The flow analysis was also performed for the different Z-classes individually, the results of which are presented in the table on the right-hand side of fig. 5.6. Heavy fragments show a larger flow than light fragments, but they all indicate a similar E_{bal}, as is readily reported in literature (e.g. [109]). The errors in the results include the statistical error and the systematic error due to the selection of the fit area. The most important systematic error which is not taken into account, is the error in the event-plane reconstruction at small flow angles, as is the case at 95 AMeV. Because the directed in-plane flow is used to reconstruct the reaction plane, the accuracy of the reconstruction depends on the magnitude of the flow. At zero flow angle the reaction plane can not be determined (and therefore, zero flow will be measured). This effect will tend to diminish the value for in-plane flow at small flow angles. It is not possible to study this with IQMD as the directed in-plane flow at 95 AMeV is still too large

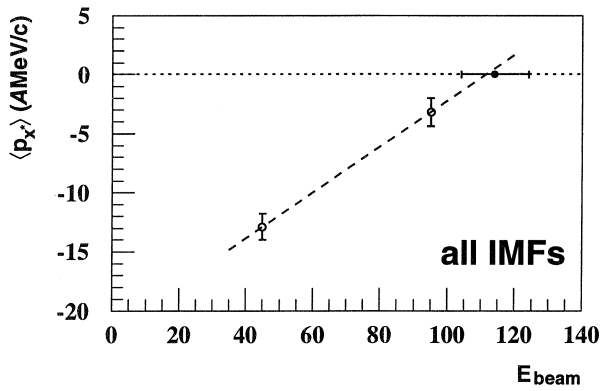

Figure 5.7: *Measured directed in-plane flow data (open circles) compared to the value derived from literature (filled circle). The line connects the two measured data points and serves to guide the eye.*

compared to the experimental results. This effect is, therefore, not be corrected for. In general a linear fit is used to determine E_{bal} from the measured flow values (e.g. [11, 109]). Fig. 5.7 shows the measured flow values (open circles) for ^{24}Mg+^{27}Al and the value derived from [11] (filled circle). The measured data points are in agreement with this value for E_{bal} of 114 $\pm$ 10 AMeV.

5.3 Azimuthal correlations and polar angles at mid-rapidity

Azimuthal correlations are considered to be a powerful tool to probe the dynamics of heavy-ion reactions, free from uncertainties in the reconstruction of the reaction plane [12, 101, 102, 116]. In this method the angular correlations of fragments emitted in the mid-rapidity region of the reaction are studied. The azimuthal-correlation method does not require an *event by event* reconstruction of the reaction plane and minimises other systematic uncertainties associated with detector acceptance and efficiency. Azimuthal correlations have been used to study many of the features of heavy-ion collisions, such as directed and rotational flow [101, 102, 103, 104, 105], balancing energy [12] and impact parameter [117].
Here the azimuthal correlations, in conjunction with the polar-angle distributions will be used to study the production of IMFs. It will be concluded that this is a dynamic process and that there is no evidence of a mid-rapidity source.

5.3.1 Introduction

The azimuthal-correlation method uses the angular difference in the azimuth, $\Delta\phi$, of different fragments to study the reaction dynamics. It makes use of the azimuthal-correlation function, which is defined as the ratio of the azimuthal angle differences of correlated fragments, $N_{\mathrm{cor}}(\Delta\phi)$ and the angle differences of uncorrelated fragments, $N_{\mathrm{uncor}}(\Delta\phi)$:

$$C(\Delta\phi) = \frac{N_{\mathrm{cor}}(\Delta\phi)}{N_{\mathrm{uncor}}(\Delta\phi)}. \tag{5.9}$$

The correlated angles are from fragments within one event. Uncorrelated fragments are generated by mixing tracks from different events. Events are mixed which are of the same impact-parameter class and have the same fragment multiplicity. These generated mixed events are corrected for the detector granularity, so two tracks are not identified by the same detector module. Real events are also corrected for this to ensure that events are processed similarly in the two (corrected and uncorrected) distributions. From this point on the term 'mixed events' will be used to indicate events consisting of uncorrelated fragments.

If particles are emitted independently, the azimuthal-correlation function is described by the auto-correlation function of the single-particle distribution:

$$C(\Delta\phi) = \int_0^{2\pi} P(\phi)P(\phi + \Delta\phi)\mathrm{d}\phi, \tag{5.10}$$

With $P(\phi)$ the distribution of independently emitted fragments. Empirically it has been shown that the fragment distribution is described by a second-order Legendre polynomial [117, 118]:

$$P(\phi) \propto 1 + a_1\cos(\phi) + a_2\cos(2\phi). \tag{5.11}$$

The value a_1 can be related to the *in plane* flow and the value a_2 is attributed to other directed motion, either *squeeze out*, if $a_2 < 0$ or rotational effects if $a_2 > 0$. If eq. 5.11 is substituted in eq. 5.10, the azimuthal-correlation function can be calculated for independently emitted fragments:

$$C(\Delta\phi) \propto \lambda_1\cos(\Delta\phi) + \lambda_2\cos(2\Delta\phi), \tag{5.12}$$

where the relationship between a_i and λ_i is given by:

$$\lambda_i = \tfrac{1}{2}a_i^2, \tag{5.13}$$

which again associates the first term in eq. 5.12 with directed flow and the second term with other collective motion, usually rotational effects, as derived in [104].

The azimuthal-correlation function will be used in our analysis to exclude the scenario of independently emitted fragments from a mid-rapidity source described above. Furthermore, the polar-angle distributions will be studied to distinguish between fragments

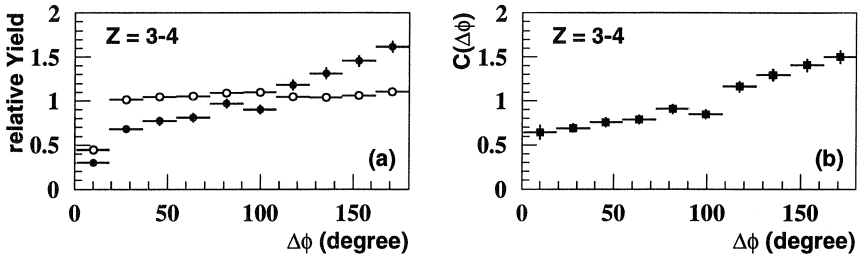

Figure 5.8: *Azimuthal distributions of IMFs with Z = 3-4 at a beam energy of 95 A MeV for mid-central events. In (a) the experimental data of correlated fragments (filled circles) and uncorrelated fragments (open circles) are shown, (b) contains the measured azimuthal-correlation function.*

emitted from a small decaying source and a dynamic production process described by IQMD. The analysis is restricted to the mid-rapidity region and the mid-central impact-parameter class. The peripheral class has a multiplicity which is too low to justify any conclusions and are excluded from the analysis. Central events show essentially the same azimuthal distributions as mid-central events. Small differences in these distributions can not be seen independently from the overall higher multiplicity of selected fragments. Because the number of fragments is used to select the centrality of the events, no conclusions can be drawn from these differences.

5.3.2 Acceptance and efficiency

The acceptance and the efficiency of the experimental set-up influence the resolution of the observables. In this section it will be shown that the azimuthal-correlation function is not influenced by the Huygens detector. This makes it possible to exclude from the data the scenario of an independently emitting mid-rapidity source (eq. 5.12). To distinguish between a small decaying source and a dynamic process, the polar angles of fragments have been studied. In the second part of this section it will be shown that the polar-angle distribution is influenced by the detector effects. However, in the mid-rapidity region this effect is small, which makes it possible to distinguish between the two different scenarios.

Azimuthal correlations

Fig. 5.8 shows the experimental azimuthal distributions between fragments with Z = 3-4 for a beam energy of 95 AMeV. In fig. 5.8a the measured distribution for correlated fragments are plotted with closed circles, the open circles show the measured distribution for mixed events. Both distributions show a strongly reduced yield at small angles, which is a direct consequence of the detector granularity. Tracks are only detected correctly if they are separated by a minimum distance, which depends on the laboratory angle of the tracks. In fig. 5.8b the resulting azimuthal-correlation

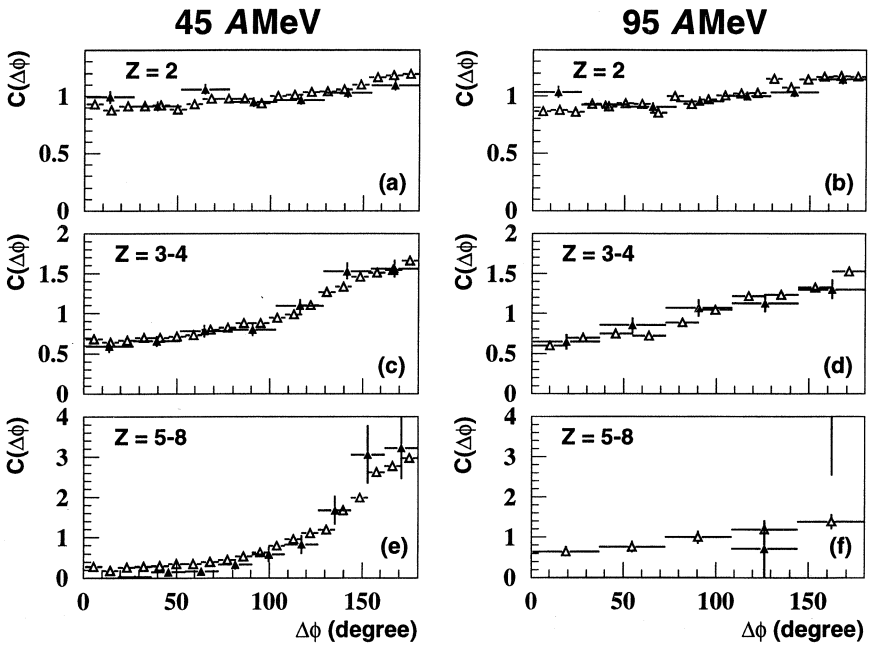

Figure 5.9: *Azimuthal correlations for IQMD events before (open triangles) and after (filled triangles) the GEANT detector simulation. All events are mid-central, the fragment charge is indicated in the top-left corner of each plot.*

function is plotted. Because the mixed events are also corrected for the detector modulation, this plot shows no detector effects. This is confirmed in fig. 5.9, where the IQMD results before and after the GEANT simulation are plotted for the different fragments at the two energies. The open triangles show the azimuthal-correlation function of IQMD results. The closed triangles show the same function as in fig. 5.8b for the IQMD events after the GEANT simulation. Fig. 5.9 shows that all detector effects are compensated and therefore, that the measured azimuthal-correlation function is equal to the real azimuthal-correlation function.

Polar-angle distributions

Due to the nature of fixed-target experiments, there will inherently be an influence of the detector on the polar-angle distributions. In the backward region the energy of emitted particles in the laboratory frame is low, therefore, the detector thresholds are relatively high. In the forward region the area close to the beam pipe (below 3°) is not covered by the Huygens detectors, which excludes this part of the phase space from the analysis. Therefore, a good detector simulation is necessary to compare the measurements to simulations. For this a GEANT detector simulation was used. This describes the interaction of a particle travelling through the detector set-up and yields the en-

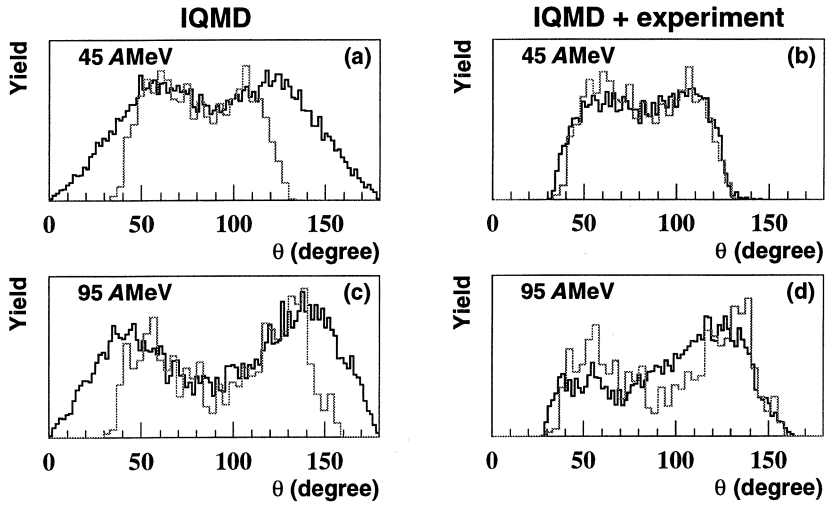

Figure 5.10: *Polar-angle distributions of Z = 3-4 at a beam energy of 45 AMeV in figures (a) and (b) and 95 AMeV in figures (c) and (d). In (a) and (c) the distributions are shown for IQMD results before (black line) and after the GEANT detector simulation (grey line). Figures (b) and (d) show the experimental data (black line) and the IQMD results after GEANT (grey line). The distributions in (b) and (d) have been normalised to the integrated area of the plots. In (a) the plots have been normalised to the integrated area between 55° and 110° and in (c) the normalisation was done for the area between 55° and 140°.*

ergy deposition of the particle in all the detector elements. The particle-identification and energy-reconstruction process performed on the experimental data (as described in chapter 3) is not incorporated in this simulation. The mid-rapidity region, where the particles used in this analysis are emitted is well covered by the Huygens detector, which makes it possible to distinguish between the different reaction scenarios.

The polar-angle distributions for mid-central events of fragments with Z = 3-4 emitted in the mid-rapidity region are shown in fig. 5.10 for the two beam energies. On the left-hand side the distributions from the IQMD simulations are shown before (black line) and after the GEANT detector simulation (grey line). The right-hand side shows the distributions of the experimental data (black line) and the IQMD results after the GEANT simulation (grey line). Fig. 5.10a illustrates the effects of the detector on the measurements. Effectively for 45 AMeV beam energy the mid-rapidity analysis is restricted to the area between 50° and 110° polar angle (in the centre-of-mass frame of the colliding nuclei). It should be noted that the MUR modules below 10° polar angle in the laboratory were not used in this analysis. These detectors have a large energy threshold which cause discontinuities in the polar-angle distributions. Because this region is not important for our investigation, it was excluded from the analysis.

Fig. 5.10b shows that the IQMD results are in agreement with the experiment.
In fig. 5.10c the effect of the detector response is simulated for the 95 AMeV data. For this beam energy the analysis is restricted to the area between 50° and 140° polar angle. Fig 5.10d shows the simulated data in conjunction with the experimental data. The mismatch between the experimental data and the simulations is mainly caused by misidentified lighter fragments. The misidentification occurs in the TPC, where the fragments are identified with a small energy, associated with the small energy deposition of the lighter fragment in the plastic scintillator. This effect is not incorporated in GEANT.

5.3.3 Results

In fig. 5.11 the azimuthal correlations for the experimental data at mid-rapidity with impact-parameter class mid-central are shown. As described before, the analysis is restricted to particles which are identified in the Huygens set-up between 10° and 78° polar angle, in the laboratory system. All figures are normalised with respect to the integrated surface of the distributions. The top six figures are for the 45 AMeV data, the bottom six are for the 95 AMeV data. On the left-hand side the correlated azimuthal distributions are shown with filled circles and the azimuthal distributions of mixed events are shown with open circles. On the right the ratio of the two (see eq. 5.9) shows the azimuthal-correlation function with filled squares. The fragments which are selected in the different figures are indicated in the top-left corner. The azimuthal-correlation functions at the two energies are for each Z-class quite similar, however, it was shown in section 5.2.2 that the directed in-plane flow at 45 AMeV is substantially larger than at 95 AMeV. From this it can be concluded that the azimuthal correlations are insensitive to directed in-plane flow.
Clearly, all distributions show an enhancement at 180°, which increases with fragment mass. Only the $Z = 2$ data at 45 AMeV shows a small increase at 0°. A description of the distributions with eq. 5.12 will yield a negative value for λ_1, using eq. 5.13 this will lead to an imaginary value for a_1. This clearly shows that these distributions can not be explained by independently emitted fragments.

Two models have been used to investigate the reaction mechanism for ^{24}Mg+^{27}Al at 45 and 95 AMeV. Firstly, the IQMD model described in chapter 4 gives a dynamic picture of the heavy-ion collision, without the inclusion of an equilibrated system at mid-rapidity. Secondly, because the maximum at 180° in the azimuthal distribution function could be due to momentum conservation of a small decaying source [116, 119, 120], a simple static-source model was used to describe the measured distributions.

In total 600.000 IQMD events were generated with a beam energy of 45 AMeV and 800.000 events with a beam energy of 95 AMeV. A GEANT simulation of the detector was used to compare the IQMD results with the data. In fig. 5.12 the azimuthal distributions of the experimental data are compared to the IQMD results. In section 5.3.2 it was shown that the detector does not influence the azimuthal distributions, therefore, the azimuthal distributions of IQMD without the GEANT detector simulation

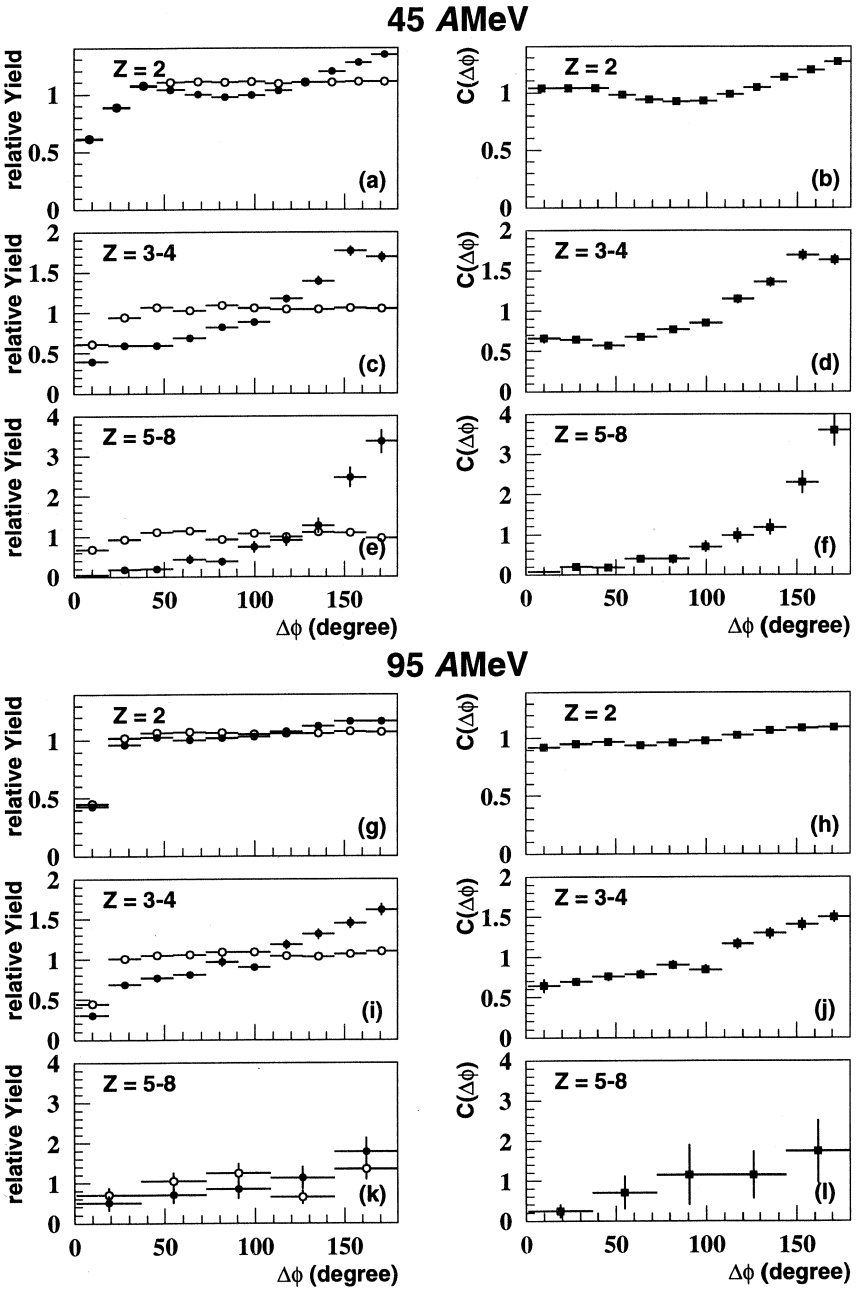

Figure 5.11: *Azimuthal correlations for different fragments and beam energies for mid-central events. The left column shows the raw-data correlations (filled circles) and the correlations for mixed events (open circles). The right column gives the ratio of the two: the azimuthal-correlation function. All plots are normalised to the integrated area of the distributions.*

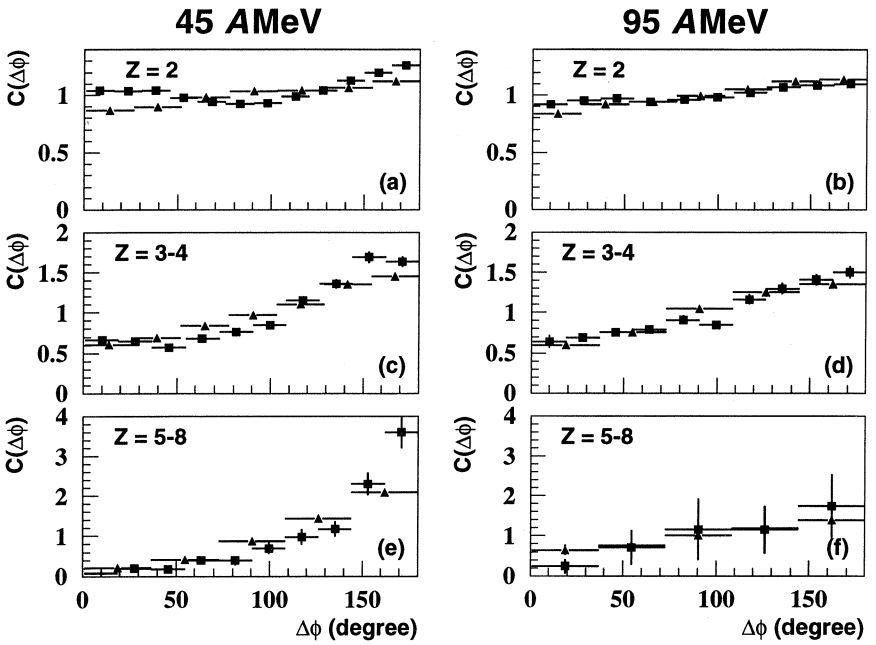

Figure 5.12: *Azimuthal correlations of the experimental data (filled squares) and IQMD events (filled triangles). All events are mid-central, the fragment charge is indicated in the top-left corner of each plot.*

are shown. Only the $Z = 2$ results are different for IQMD and the experimental data. This is due to a different production process for $Z = 2$ than the heavier IMFs, which is not incorporated in IQMD. All other distributions of the experimental data and IQMD are in good agreement.

To describe the decaying mid-rapidity source, a simple participant/spectator scenario was assumed. Events were generated using a model describing a small static source at mid-rapidity undergoing prompt multifragmentation [121]. In this model the Coulomb interaction is neglected and the multifragmentation process is governed by phase space. The source size, the excitation energy and the decay mode are input parameters. The excitation energy for the source was taken to be the average centre-of-mass energy per nucleon, i.e. 11 AMeV and 23 AMeV for beam energies of 45 AMeV and 95 AMeV, respectively. The distributions from this static-source model were also processed by the GEANT detector simulation. The source size was used as a parameter to fit the azimuthal distributions of the static-source model to the data. This fit was performed for each fragment-class individually and has an accuracy of approximately 10%. In fig. 5.13 the resulting azimuthal distributions (open crosses) are compared to the data (filled squares). The source sizes do not depend on the beam energy. They do, however, depend on the mass of the emitted IMFs. For the $Z = 2$ data the mass of the source

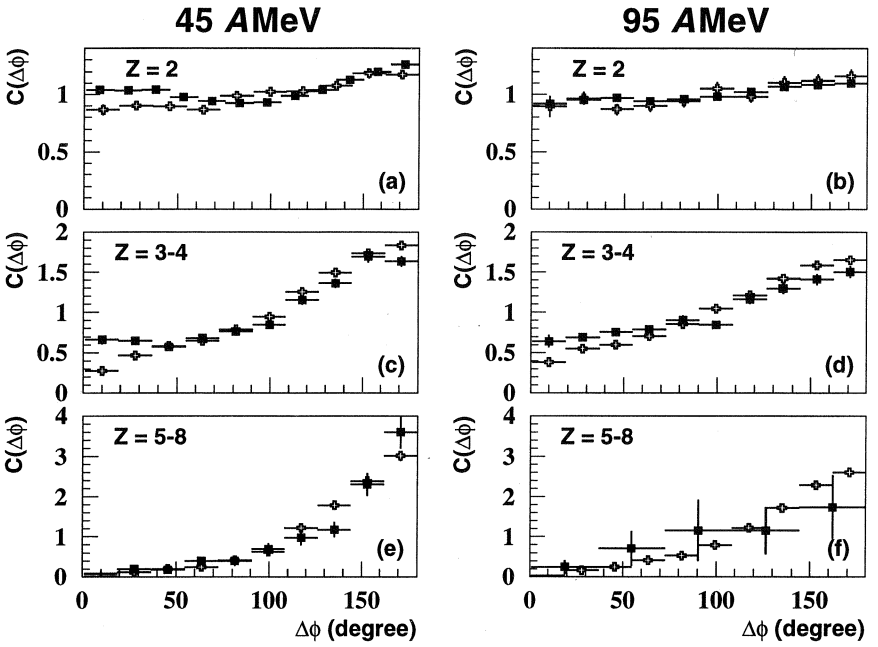

Figure 5.13: *Azimuthal correlations of the experimental data (filled squares) and of the static-source events filtered by GEANT (open crosses). The experimental data are mid-central, for details on the static-source data, see text. The fragment charge is indicated in the top-left corner of each plot.*

is 32 amu, for Z = 3-4 the mass is 36 amu and for Z = 5-8 the mass is 40 amu. The decay mode has very little influence on the distributions. Simulations for Z = 3-4 decaying in one Z = 3, one Z = 4 and several small fragments show essentially the same azimuthal distributions as a three particle decay mode. The decaying static-source distributions are in agreement with the experimental data, although the levelling of the experimental data (and the IQMD data) at small angles is not reproduced. Therefore, the static-source model and IQMD give an equally good description of the measured azimuthal distributions.

Although it is not possible to distinguish the two described models by studying the azimuthal correlations, the polar-angle distributions should be able to make a distinction [122]. Any decaying source at mid-rapidity will have a maximum in these distributions at 90°, whereas the polar-angle distributions of IQMD show a minimum at 90° flanked by two maxima [122, 123]. It was shown that these maxima in IQMD are remnants of the target and the projectile and are therefore called target-like and projectile-like [123]. This is a fundamental difference between the two models; an equilibrated decaying source has lost by definition all information about its initial state, whereas IQMD shows a strong initial-final state correlation. Fig. 5.14 shows the polar-angle

distribution at mid-rapidity for the different fragments at the two beam energies. On the left-hand side the IQMD results after GEANT (grey line) are compared to the measured distributions (black line), on the right-hand side the measured distributions (black line) are shown with the static-source results (grey line).
For 45 AMeV the IQMD results nicely describe the measured data. For Z = 3-4, fig. 5.14c shows for both IQMD and the measured data target and projectile-like maxima. Fig. 5.14d shows the same distributions for the measurement and the static-source model. These two figures clearly show that the experiment and IQMD are in agreement and that the static-source model fails to describe the measurement. In fact, as was already stated, any decaying-source model will always show a peak in the polar-angle distribution at 90°, which is contradicted by the measurement. For heavy fragments, fig. 5.14d and fig. 5.14e show that the measurement is in agreement with IQMD and is different from the static-source model. For these fragments the projectile-like and target-like maxima fall outside the experimentally accessible domain. The figures 5.14a and 5.14b for the Z = 2 distributions show no significant difference between IQMD and the static-source model. The data, however, seems to indicate target-like and projectile-like maxima. As in the azimuthal-correlation function this difference between the experimental data and IQMD is probably due to a different production process for Z = 2. The 95 AMeV distributions show essentially the same results as the 45 AMeV distributions. The experiment is well described by IQMD and the static-source model fails to describe the data. For Z = 2 the data in fig. 5.14g show definite target-like and projectile-like maxima in both the measured data and IQMD. The static-source model in fig. 5.14h shows a maximum where both other distributions show a minimum. This is also the case in fig. 5.14j for Z = 3-4. Despite the enhancement in fig. 5.14i for the measured data at small angles, discussed in the section 5.3.2, this distribution still shows target-like and projectile-like maxima, similar to the IQMD distribution. Statistics do not allow for a comparison of the Z = 5-8 data, for completeness they are shown in figures 5.14k and 5.14l.
From the polar-angle distributions a clear distinction can be made between a decaying-source scenario and a purely dynamic process as described by IQMD. Above it has been shown that the IMF production in the experimental data is the result of dynamic processes.

5.3.4 Discussion

In the previous section the azimuthal distribution function of mid-rapidity particles in conjunction with the polar-angle distributions showed that the IMF emission in nuclear collisions of ^{24}Mg+^{27}Al at 45 AMeV and 95 AMeV is governed by dynamic processes with no experimental evidence of a mid-rapidity source. The maxima in the azimuthal distributions were shown to be due to the correlations between target-like and projectile-like fragments.
It was found that the azimuthal correlations of mid-rapidity particles for both energies are quite similar, whereas the measured directed in-plane flow is substantially higher at 45 AMeV than at 95 AMeV. This shows that the azimuthal correlations are insensitive to the directed in-plane flow. The azimuthal-correlation functions of

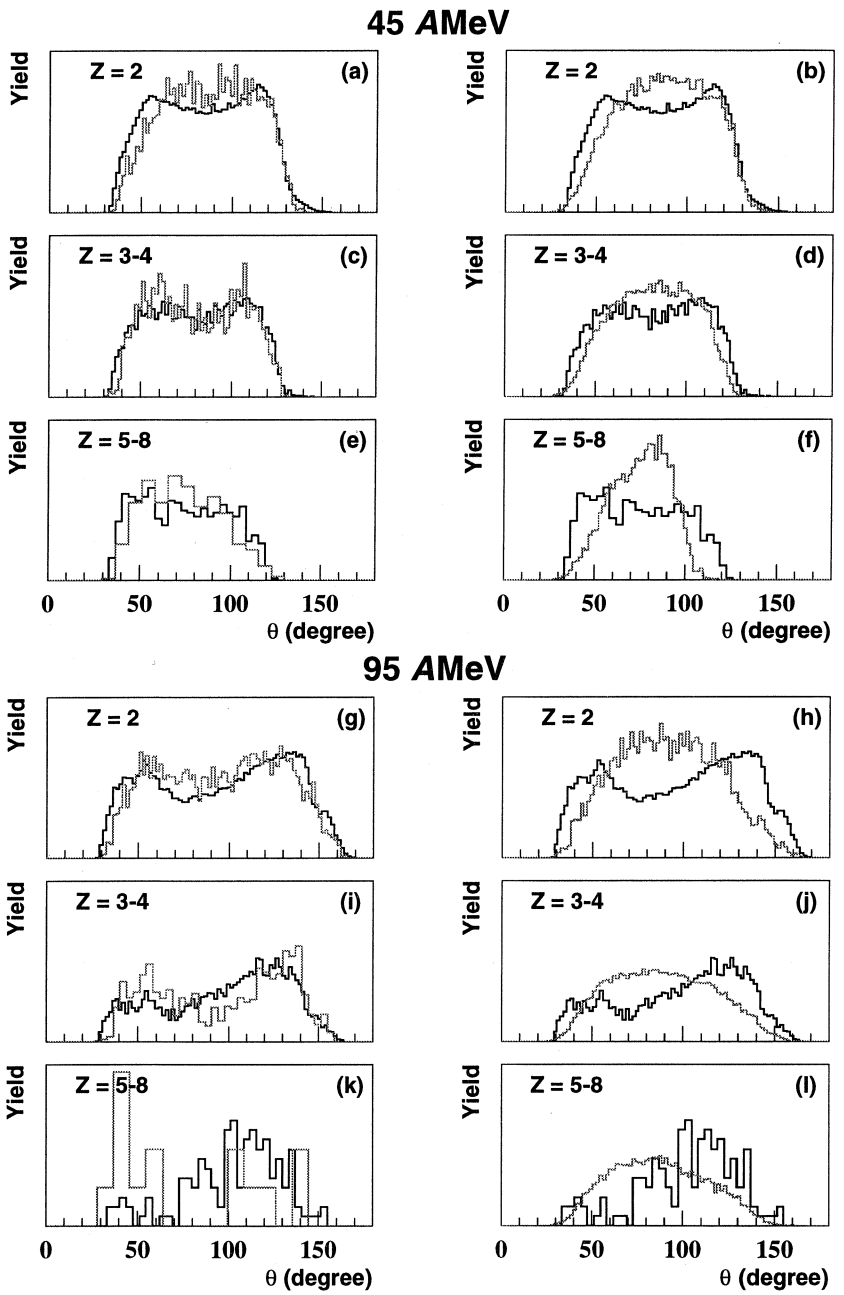

Figure 5.14: *Polar-angle distributions for the experimental data (black lines) and on the left-hand side IQMD data after GEANT (grey lines) and on the right the static-source data (grey lines). The fragment charge is indicated in the top-left corner of each plot.*

mid-rapidity particles in the aforementioned reaction exhibit pronounced maxima at 180°. This maximum increases with fragment size and its existence is not influenced by the beam energy. The measured azimuthal distributions can not be caused by a single mid-rapidity source emitting particles independently [101, 103, 104, 105], because the distribution can not be described using the auto-correlation function (eq. 5.10). Coulomb repulsion [104, 124] is also not responsible for the maxima in the azimuthal distributions [122]. Therefore, the maxima at 180° can only be explained if the emitted particles are strongly correlated [12]. Momentum conservation of a small decaying source can be responsible for this maximum [116, 119, 120]. Therefore, a model of a small static decaying source was used to fit to the data. More elaborate models, such as a hot fast-spinning source, a multifragmentation source or a statistical-decay source [119, 120] can also be used. However, all these models yield a maximum in the polar-angle distribution at 90°. The GEANT simulations show that the Huygens detector is sensitive to this maximum. However, the measured data does not show a maximum at this angle, but instead shows a minimum, flanked by a projectile-like and a target-like maximum, which are nicely described by the IQMD results. This conclusively shows that IMF production for these small systems is a dynamic process with no evidence of a single mid-rapidity source for IMF emission.
It can be stated that the nuclei of the small system studied in this thesis are not able to form a compound system. Literature shows that by increasing the size of one of the nuclei, the azimuthal distributions start to show a more symmetric shape [116, 120]. This could indicate that pressure from the surrounding nuclear matter forces the creation of a compound system. However, as was shown above, very different scenarios can lead to a similar azimuthal-correlation function. The azimuthal-correlation function should, therefore, not be taken as conclusive evidence of any scenario.

5.4 Conclusions

In this chapter the results of the study of the reaction ^{24}Mg+^{27}Al at 45 and 95 AMeV were presented. Three angles of investigation were taken. First the impact-parameter selection was studied, then the collective flow and finally the azimuthal correlations and polar-angle distributions. Each of the subjects yields its particular conclusions.

The impact-parameter selection procedure, based on the charged-particle multiplicity, was studied using IQMD events and the GEANT detector simulation. This showed that indeed an impact-parameter selection can be made with this method. However, the accuracy of this selection for these small systems is not very good. In particular the central-event selection is heavily polluted by mid-central events. Furthermore, the data showed that peripheral events have such small multiplicities, that no useful analysis can be performed on these events. Therefore, only mid-central events have been studied for ^{24}Mg+^{27}Al at 45 and 95 AMeV .

To study the collective flow, first the event plane has to be reconstructed. Again IQMD events and the GEANT detector simulation were used to study the effectiveness of sev-

eral different event-plane reconstruction methods. It was found that the event plane can be reconstructed. All methods give a similar accuracy, but the azimuthal-correlation method gives (marginally) the best result. Using this method to reconstruct the reaction plane, the directed in-plane flow was studied. The experimental data showed a strongly reduced flow at 95 AMeV compared to 45 AMeV, in accordance with a balancing energy of 114 $\pm$ 10 AMeV as derived from literature.

Finally the reaction dynamics were studied using the azimuthal correlations and the polar-angle distributions of IMFs emitted at mid-rapidity, both of which do not require an event-plane reconstruction. The azimuthal correlations for the two energies are quite similar, whereas the directed in-plane flow is substantially higher at 45 AMeV than at 95 AMeV. This shows that the azimuthal correlations are insensitive to the magnitude of the directed in-plane flow. At both energies, the azimuthal-correlation functions for the various IMFs show absolute maxima at 180°, which can not be explained by a mid-rapidity source emitting fragments independently. However, the distributions are in agreement IQMD. The maxima are either caused by momentum conservation or by target-projectile correlations. Therefore, a second model was introduced, which describes the prompt multifragmentation of a small source. This model was fitted to the measured azimuthal-correlation functions, resulting in source sizes between 32 and 40 amu, depending on the mass of the emitted IMFs. Subsequently, the polar angles of the two models were compared to the experimental data. The distributions of the experimental data showed target- and projectile-like maxima, which can not be described by a decaying source, but are described by IQMD. Therefore, it is concluded that IMF production in these small systems is a dynamic process with no evidence of a mid-rapidity source.

Bibliography

[1] P.M. Endt, Nucl. Phys. A633 (1998) 1.

[2] P.J. Brussaard and P.W.M. Glaudemans, *Shell-model applications in nuclear spectroscopy*, North-Holland, Amsterdam (1977).

[3] H. Satz, preprint CERN, cern-th/96-172, Proc. 1st Catania Rel. Ion Studies, Acicastella, Italy (1996).

[4] C.-Y. Wong, *Introduction to high-energy heavy-ion collisions*, Chapter 9, World Scientific, Singapore (1994).

[5] C. De Troyes, Arthurian legends, Troyes, France (1160-1172).

[6] P. Coles and F. Lucchin, *Cosmology*, Chapters 7-8, Wiley & Sons, Chichester (1995).

[7] A.C. Phillips, *The physics of stars*, Chapter 6, Wiley & Sons, Chichester (1994).

[8] E. Witten, Phys. Rev. D30 (1984) 272.

[9] F. Grassi *et al.*, Astrophys. J. 492 (1998) 263.

[10] L.P. Chernai, *Introduction to relativistic heavy ion collisions*, Chapters 1&11, Wiley & Sons, Chichester (1994).

[11] G.D. Westfall *et al.*, Phys. Rev. Let. 71 (1993) 1986.

[12] A. Buta *et al.*, Nucl. Phys. A584 (1995) 397.

[13] R. Pak *et al.*, preprint Michigan State University, MSUCL-1010 (1996).

[14] S. Soff *et al.*, Phys. Rev. C51 (1995) 3320.

[15] J. Péter, Nucl. Phys. A545 (1992) 173.

[16] G. Sauer, H.Chandra and U. Mosel, Nucl. Phys. A264 (1976) 221.

[17] H. Jaqaman, A.Z. Mekjian and L. Zamick, Phys. Rev. C27 (1983) 2782.

[18] A.I. Warwick *et al.*, Phys. Rev. C27 (1983) 1083.

[19] A.S. Botvina and D.H.E. Gross, Phys. Rev. C58 (1998) 23.

[20] J. Tõke and W.U. Schröder, preprint cern-th/9807066 (1998).

[21] A.S. Botvina and D.H.E. Gross, preprint CERN, nucl-th/9808004 (1998).

[22] L. Phair *et al.*, Phys. Rev. Let. 75 (1995) 213.

[23] M. D'Agostino *et al.*, Phys. Let. B371 (1996) 175.

[24] N. Marie *et al.*, Phys. Let. B391 (1997) 15.

[25] L. Beaulieu *et al.*, Phys. Rev. Let. 81 (1998) 770.

[26] L. Phair *et al.*, preprint LBNL-41893 (1998), sub. Phys. Rev. C.

[27] J. Tõke *et al.*, Phys. Rev. Let. 77 (1996) 3514.

[28] J. Tõke *et al.*, Phys. Rev. C56 (1997) 1683.

[29] M.F. Rivet *et al.*, preprint GANIL P9815 (1998), acc. Phys. Let. B.

[30] O. Tirel *et al.*, preprint GANIL P9826 (1998).

[31] T.M.V. Bootsma *et al.*, Nucl. Instr. and Meth. A349 (1994) 204.

[32] G.Bizard *et al.*, Nucl. Instr. and Meth A244 (1986) 483.

[33] T.M.V. Bootsma, Ph.D. thesis, Utrecht university (1993), ISBN 90-393-0026-7.

[34] J.B. Birks, *The theory and practice of scintillation counting*, Macmillon New York (1964).

[35] M.B. Koopmans, Internal Report, Utrecht University, UU(SAP) 96-1 (1996).

[36] R.B. Murray and A. Meyer, Phys. Rev. 122 (1960) 815.

[37] R. Gwin and R.B. Murray, Phys. Rev. 131 (1963) 501.

[38] P. Schotanus, R. Kamermans and P. Dorenbos, IEEE Trans. Nucl. Sci. 37 (1990) 177.

[39] A. Oed, Nucl. Instr. and Meth. A263 (1988) 351.

[40] G.J. van Nieuwenhuizen, Ph.D. Thesis, Universiteit Utrecht (1993), ISBN 90-393-0465-3.

[41] R.J.M. Snelling, Ph.D. thesis, Utrecht University (1998), ISBN 90-393-1634-1.

[42] A.J. Michielsen and C.J.W. Twenhöfel, Nucl. Instr. and Meth. A334 (1993) 234.

[43] E.H. Agterhuis, proc. AIHENP95 p.41-46, World Scientific (1995).

[44] E.H. Agterhuis, Ph.D. thesis, Utrecht University (1996), ISBN 90-393-1217-6.

[45] E.P. Prendergast *et al.*, Nucl. Instr. and Meth. A385 (1997) 243.

[46] M.P. Allen, D.J. Tildesley, *Computer Simulation of Liquids*, Clarendon Press, (1987).

[47] S. Biagi, private communication 1995.

[48] B. Sitar *et al.*, *Ionization Measurements in High Energy Physics, Springer tracts in modern physics*, Vol. 124, Springer-Verlag, (1993).

[49] L.G. Christophorou *et al.*, Nucl. Instr. and Meth. A200 (1979) 141.

[50] I. Lehraus, R. Matthewson and W. Tejessy, Nucl. Instr. and Meth. A200 (1982) 199.

[51] G.J. van Nieuwenhuizen *et al.*, Nucl. Instr. and Meth A325 (1993) 516.

[52] C.T.A.M. de Laat and P.G. Kuijer, IEEE Trans. on Nucl. Sci. Vol. 41 No. 1 (1994) 58.

[53] C.T.A.M. de Laat *et al.*, IEEE Trans. on Nucl. Sci. Vol. 44 No. 4 (1997) 1635.

[54] J.J. Langerak *et al.*, Nucl. Instr. and Meth. A340 (1994) 392.

[55] W.R. Leo, *Techniques for nuclear and particle physics experiments*, Springer-Verlag Berlin Heidelberg (1994).

[56] W. M. Arnold Bik and F.H.P.M. Habraken, Rep. on Prog. in Phys. 56 (1993) 859.

[57] R.J.M. Snelling *et al.*, submitted to NIM A.

[58] W. Hulsbergen, Internal report, Utrecht University, UU(SAP) 97-2 (1997).

[59] H. Bethe, Z. Phys. 76 (1932) 293.

[60] F. Bloch, Z. Phys. 81 (1933) 363.

[61] F. Bloch, A. Phys. 16 (1933) 285.

[62] Ziegler *et al.*, *The stopping and range of ions in solids*, Vol 1, Pergamon Press, New York (1985).

[63] J.B. Birks., Proc. Phys. Soc. A64 (1951) 874.

[64] E. Newman, A.M. Smith, F.E. Steigert, Phys. Rev. 122 (1961) 1520.

[65] J.J.L.M. Habets, Internal report, Utrecht University, UU(SAP) 97-7 (1997).

[66] GEANT 3.21, CERN Program library long writeup W5013.

[67] H. Stöcker, J.A. Maruhn and W. Greiner, Phys. Rev. Let 44 (1980) 725.

[68] H. Stöcker *et al.*, Phys. Rev. C25 (1982) 1873.

[69] B.D. Day, Rev. Mod. Phys. 39 (1967) 719.

[70] J.W. Negele, Phys. Rev. C1 (1970) 1260.

[71] W. Scheid, H. Müller and W. Greiner, Phys. Rev. Let. 32 (1974) 741.

[72] H.G. Baumgardt *et al.*, Z. Physic A273 (1975) 359.

[73] A.S. Hirsch *et al.*, Phys. Rev. C29 (1984) 508.

[74] P. Danielewicz, Nucl. phys. A314 (1979) 465.

[75] B. Friedman and V.R. Pandharipande, Nucl. phys. A361 (1981) 502.

[76] G. Bertsch and P.J. Siemens, Phys. Let. B126 (1983) 9.

[77] J. Randrup and S.E. Koonin, Nucl. Phys. A356 (1981) 223.

[78] J.P. Bondorf *et al.*, Nucl. Phys. A443 (1985) 321.

[79] B. Friedman and W.G. Lynch, Phys. Rev. C28 (1983) 16.

[80] C. Barbagallo, J. Richert and P. Wagner, Z. Physic A324 (1986) 97.

[81] D. Staufer, Phys. Rep. 54 (1979) 1.

[82] W. Bauer *et al.*, Phys. Let. 150B (1985) 53.

[83] G. Bertsch and S. Das Gupta, Phys. Rep. 160 (1988) 189.

[84] E.A. Uehling and G.E. Uhlenbeck, Phys. Rev. 43 (1933) 552.

[85] H. Kruse, B.V. Jacak and H. Stöcker, Phys. Rev. Let. 54 (1985) 289.

[86] G. Bertsch, H. Kruse and S. Das Gupta, Phys. Rev. C29 (1984) 673.

[87] L.W. Nordheim, Proc. Roy. Soc. (London) A119 (1928) 689.

[88] C. Gregoire *et al.*, Nucl. Phys. A465 (1987) 317.

[89] W. Botermans and R. Malfliet, Phys. Rep. 198 (1990) 115.

[90] J. Aichelin and H. Stöcker, Phys. Let. B176 (1986) 14.

[91] J. Aichelin *et al.*, Phys. Rev. C37 (1988) 2451.

[92] J. Aichelin, Phys. Rep. 202 (1991) 233.

[93] T.H.R. Skyrme, Phil. Mag. 1 (1956) 1043.

[94] T.H.R. Skyrme, Nucl. Phys. 9 (1959) 615.

[95] D. Vautherin and D.M. Brink, Phys. Rev. C5 (1972) 626.

[96] C. Hartnack, Ph.D. thesis, GSI-Report 93-05 (1993), ISBN 0171-45446.

[97] H. Feldmeier, K. Bieler and J. Schnack, Nucl. Phys. A586 (1995) 493.

[98] A. Ono *et al.*, Phys. Rev. Let. 68 (1992) 2898.

[99] E.D. Cooper *et al.*, Phys. Rev. C36 (1987) 2170.

[100] C. Hartnack *et al.*, Eur. Phys. J. A1 (1998) 151.

[101] R.A. Lacey *et al.*, Phys. Rev. Let. 70 (1993) 1224.

[102] J.C. Angélique *et al.*, Nucl. Phys. A614 (1997) 261.

[103] S. Wang *et al.*, Phys. Rev. C44 (1991) 1091.

[104] L. Phair *et al.*, Phys. Rev. Let. 77 (1996) 822.

[105] W.Q. Shen *et al.*, Phys. Rev. C57 (1998) 1508.

[106] C.A. Ogilvie *et al.*, Phys. Rev. C40 (1989) 654.

[107] L. Phair *et al.*, Nucl. Phys. A548 (1992) 489.

[108] C. Cavata *et al.*, Phys. Rev. C42 (1990) 1760.

[109] C.A. Ogilvie *et al.*, Phys. Rev. C42 (1990) 10.

[110] V. de la Mota *et al.*, Phys. Rev. C46 (1992) 677.

[111] M. Gyulassy, K.A. Frankel and H. Stöcker, Phys. Let. B110 (1982) 185.

[112] P. Danielewicz and G. Odyniec, Phys. Let. B157 (1985) 146.

[113] W.K. Wilson *et al.*, Phys. Rev. C45 (1992) 738.

[114] C.A. Ogilvie *et al.*, Phys. Rev. C40 (1989) 2592.

[115] C. Liewen, Z. Fengshou, and J. Genming, Phys. Rev. C58 (1998) 2283.

[116] C.B. Chitwood *et al.*, Phys. Rev. C34 (1989) 858.

[117] W.Q. Shen *et al.*, Nucl. Phys. A551 (1993) 333.

[118] M. Demoulins *et al.*, Phys. Let. B241 (1990) 476.

[119] T. Ethvignot *et al.*, Phys. Rev. C47 (1993) 2099.

[120] T. Ethvignot *et al.*, Phys. Rev. C48 (1993) 618.

[121] F. James, CERN report 68-15 (1968).

[122] R.J.M. Snelling *et al.*, Phys. Let. B426 (1998) 263.

[123] P.-B. Gossiaux and J. Aichelin, Phys. Rev. C56 (1997) 2109.

[124] T.M. Hamilton *et al.*, Phys. Rev. C53 (1996) 53.

Summary

This thesis describes the study of the reaction dynamics in heavy-ion collisions of small nuclear systems at intermediate energies. For this, experiments were performed of ^{24}Mg+^{27}Al at 45 and 95 AMeV.

The experiments described in this thesis were performed at the GANIL accelerator facility in Caen (France) using the Huygens detectors in conjunction with the 'MUR'. The Huygens detectors consist of the CsI(Tl)-Wall (CIW) covering the backward hemisphere and, located at mid-rapidity, the central trigger detector (CTD), a gas chamber with microstrip read-out backed by 48 plastic scintillators. The forward region is covered by 16 of the plastic scintillators of the CTD and by the MUR, a time-of-flight wall consisting of 96 plastic scintillator sheets.

In earlier experiments only fragments with atomic number, Z, greater then two could be identified in the CTD. Therefore, an elaborate investigation was done into the properties of different drift gases. The use of freon (CF_4) in the drift chamber, combined with an increase of the gas pressure to 150 mbar, makes it possible to identify all particles with $Z \geq 2$. Under these conditions particles with $Z = 1$ can only be identified to approximately 25 AMeV. In the forward region all particles with $Z \geq 1$ are identified. Due to technical difficulties the CIW could only be used as a multiplicity counter.

The Isospin Quantum Molecular Dynamics (IQMD) model has been used, to interpret the measured data. This model gives a microscopical description of heavy-ion collisions and simulates collisions on an *event by event* basis. This approach ensures that natural fluctuations and particle correlations are included in the simulations. In IQMD all protons and neutrons are represented as individual Gaussian wave packets. They are initialised in the nucleus with the full available Fermi energy. After initialisation the path of each nucleon is calculated for 200 fm/c, after which the simulation is stopped. At this time, nucleons which are close in space are clustered into fragments. The events generated by IQMD can then be processed by a GEANT detector simulation. This calculation takes into account the effects of the detector geometry and the response of the detector on the incoming particles. By using the GEANT simulation it is possible to give a direct comparison between the results of IQMD (or of any other model) and the experimental data.

The impact-parameter selection procedure, based on the charged-particle multiplicity, was studied using IQMD events and the GEANT detector simulation. This showed that indeed an impact-parameter selection can be made with this method. However, the accuracy of this selection for these small systems is not very good. In particular the central-event selection is heavily polluted by mid-central events. Furthermore, the experimental data showed that peripheral events have such small multiplicities, that no useful analysis can be performed on these events. Therefore, only mid-central events have been studied for ^{24}Mg+^{27}Al at 45 and 95 AMeV.

In order to study the collective flow in heavy-ion collisions, first the event plane has to be reconstructed. Again IQMD events and the GEANT detector simulation were used to investigate the effectiveness of several different event-plane reconstruction methods. It was found that an event plane can be reconstructed. All methods give a similar accuracy, however, the azimuthal-correlation method gives (marginally) the best result. With this method to reconstruct the reaction plane, the directed in-plane flow was studied. The experimental data showed a strongly reduced flow at 95 AMeV compared to 45 AMeV, in accordance with a balancing energy of 114 $\pm$ 10 AMeV as derived from literature.

Finally, the reaction dynamics were studied using the azimuthal correlations and the polar-angle distributions of intermediate-mass fragments (IMFs) emitted at mid-rapidity, both of which do not require an event-plane reconstruction. The azimuthal correlations for the two energies are quite similar, whereas the directed in-plane flow is substantially higher at 45 AMeV than at 95 AMeV. This shows that the azimuthal correlations are insensitive to the magnitude of the directed in-plane flow. At both energies, the azimuthal-correlation functions for the various IMFs show absolute maxima at 180°, which can not be explained by a mid-rapidity source emitting fragments independently. However, the distributions are described by IQMD. The maxima are either caused target-projectile correlations (as in IQMD) or by momentum conservation. To describe the momentum-conservation scenario, a second model was introduced, which simulates the prompt multifragmentation of a small source. This model was fitted to the measured azimuthal-correlation functions, resulting in source sizes between 32 and 40 amu, depending on the mass of the emitted IMFs. Subsequently, the polar-angle distributions of the two models were compared to the experimental data. The distributions of the experimental data showed target- and projectile-like maxima, which can not be described by a decaying source, but are nicely described by IQMD. Therefore, it is concluded that the IMF production in these small systems is a dynamic process with no evidence of a mid-rapidity source.

Samenvatting

Dit proefschrift beschrijft het onderzoek naar de reactiedynamica in zware-ionenbotsingen van kleine nucleaire systemen bij intermediaire energieën. Hiervoor zijn experimenten uitgevoerd van ^{24}Mg+^{27}Al met energieën van 45 en 95 AMeV.

De experimenten beschreven in dit werk zijn uitgevoerd met de Huygensdetectoren en de 'MUR' bij het versnellerinstituut GANIL te Caen (Frankrijk). De Huygensdetectoren bestaan uit een CsI(Tl)-muur (CIW), die de achterwaartse ruimtehoek bestrijkt en, in het mid-rapiditeitsgebied, de centrale trekker detector (CTD), een gasgevulde kamer met microstripuitlezing, omsloten door 48 plastic scintilatoren. Het voorwaartse gebied wordt bestreken door 16 plastics van de CTD en de MUR, een vluchttijdmetingsmuur, bestaande uit 96 plastic scintilatorvellen.

In voorgaande experimenten was het alleen mogelijk om deeltjes met atoomgetal, Z, groter dan twee in de CTD te meten. Daarom is uitgebreid onderzoek gedaan naar de eigenschappen van verschillende driftkamergassen. Met freon (CF_4) in de driftkamer en door de druk te verhogen naar 150 mbar is het mogelijk om alle deeltjes met $Z \geq 2$ te meten. Onder deze omstandigheden kunnen deeltjes met $Z = 1$ alleen geïdentificeerd worden met energieën lager dan 25 AMeV. In het voorwaartse gebied worden alle deeltjes met $Z \geq 1$ geïdentificeerd. Door technische problemen kon de CIW alleen gebruikt worden als een multipliciteitsteller.

Het Isospin Quantum Moleculaire Dynamica (IQMD) model is gebruikt, om de experimentele gegevens te interpreteren. Dit model geeft een microscopische beschrijving van zware-ionenbotsingen en simuleert per berekening één enkele individuele botsing. Deze aanpak zorgt ervoor dat de natuurlijke fluctuaties en de correlaties tussen deeltjes binnen een botsing behouden zijn. In IQMD worden alle protonen en neutronen beschreven als individuele Gaussische golfpakketten. Zij worden geïnitialiseerd in de kern, gebruik makend van de volledig beschikbare Fermi-energie. Na de initialisatie wordt het pad van elk individueel kerndeeltje gevolgd gedurende 200 fm/c, waarna de simulatie wordt gestopt. Vervolgens worden de kerndeeltjes, die zich in de ruimte dicht bij elkaar bevinden, samengebonden in fragmenten. De botsingen, die door IQMD zijn gegenereerd, kunnen dan worden verwerkt door de GEANT-detectorsimulatie. GEANT simuleert de effecten van de detectorgeometrie en de respons van de detector op de inkomende deeltjes. Door GEANT te gebruiken, is het mogelijk om de resulta-

ten van IQMD (of van elk ander model) en de experimentele data direct met elkaar te vergelijken.

De botsingsparameterselectieprocedure, die gebaseerd is op de hoeveelheid geladen deeltjes, is bestudeerd, gebruik makend van IQMD-botsingen en de GEANT-detectorsimulatie. Dit liet zien dat er inderdaad een botsingsparameterselectie kan worden gemaakt. Echter, de nauwkeurigheid van deze selectie voor kleine systemen is niet erg goed. In het bijzonder is gebleken dat de centrale-botsingsselectie zwaar verontreinigd is met mid-centrale botsingen. Verder bleek uit de experimentele data dat de multipliciteit van de perifere botsingen zo laag is, dat er geen analyse met deze botsingen gedaan kan worden. Daarom zijn alleen mid-centrale botsingen bestudeerd voor ^{24}Mg+^{27}Al bij 45 en 95 AMeV.

Om de collectieve stroom in zware-ionenbotsingen te bestuderen, moet eerst het reactievlak worden gereconstrueerd. Weer zijn IQMD botsingen en de GEANT-detectorsimulatie gebruikt om de effectiviteit te testen van verschillende methodes om het reactievlak te bepalen. Alle onderzochte methodes geven een vergelijkbare nauwkeurigheid, echter, de azimutale-correlatiemethode geeft (marginaal) het beste resultaat. Met deze methode om het reactievlak te bepalen, is de collectieve, in het reactievlak liggende stroom bestudeerd. De experimentele gegevens laten bij 95 AMeV een sterk gereduceerde stroom zien ten opzichte van 45 AMeV . Dit komt overeen met de uit de literatuur bepaalde waarde voor de evenwichtsenergie van 114 $\pm$ 10 AMeV.

Tenslotte is de reactiedynamica bestudeerd met behulp van azimutale correlaties en polaire-hoekverdelingen van de in het mid-rapiditeitsgebied uitgezonden intermediaire-massafragmenten (IMFs). Hiervoor is geen reactievlakbepaling nodig. De azimutale correlaties voor beide energieën lijken sterk op elkaar, terwijl de gerichte stroom bij 95 AMeV aanzienlijk kleiner is dan bij 45 AMeV. Dit laat zien dat de azimutale correlaties ongevoelig zijn voor de grootte van de stroom. Bij beide energieën zijn er maxima in de azimutale-correlatiefuncties voor de verschillende IMFs bij 180°. Deze maxima kunnen niet verklaard worden door een mid-rapiditeitsbron die deeltjes onafhankelijk van elkaar uitzendt. De verdelingen worden echter wel beschreven door IQMD. De maxima worden veroorzaakt ofwel door correlaties tussen deeltjes van de trefplaat en van het projectiel (zoals in IQMD), ofwel door impulsbehoud. Om het impulsbehoudscenario te beschrijven, is een tweede model geïntroduceerd, dat de directe multifragmentatie simuleert van een kleine bron. Dit model is passend gemaakt aan de gemeten azimutale-correlatiefuncties, hetgeen brongroottes opleverde tussen de 32 en 40 amu, afhankelijk van de massa's van de uitgezonden IMFs. Vervolgens zijn de polaire verdelingen van de twee modellen vergeleken met de experimentele data. De verdelingen van de experimentele data lieten trefplaat- en projectiel-achtige maxima zien, welke niet kunnen worden verklaard met een uit elkaar vallende bron. Deze verdelingen komen wel overeen met de IQMD-verdelingen. Daarom is de conclusie van dit onderzoek dat de IMF-productie in deze kleine systemen een dynamisch proces is en dat er geen aanwijzingen zijn voor een mid-rapiditeitsbron.

Mijn dank

Vier jaar lang heb ik gewerkt aan de totstandkoming van dit boekje. Ondanks de bloed, zweet en tranen die dit heeft gekost (vaak letterlijk), kijk ik met plezier terug op deze tijd. Dit heeft veel te maken met de mensen die mij hebben geholpen bij mijn werk. Ik ben blij dat ik hier de kans heb om hen (nogmaals) te bedanken:

Als eerste wil ik mijn promotor René Kamermans noemen. Niet alleen heeft hij qua fysica veel in mijn onderzoek ingebracht, ook was hij in staat mij tijdens de vele, lange maanden kalibreren te blijven motiveren. De wekelijkse discussies in zijn kamer staan aan de basis van de resultaten in mijn proefschrift.
Voor de dagelijkse problemen kon ik altijd terecht bij Paul Kuijer. Zonder zijn hulp was ik blijven steken in het moeras van de software en hardware dat de Huygensdetectoren omringt. De discussies die wij hebben gevoerd over de analyse en de interpretatie van de resultaten hebben zeker bijgedragen aan de kwaliteit van dit boekje.
Raimond Snellings heeft voor mij de weg gebaand, waardoor ik mijn werk inderdaad binnen vier jaar af heb kunnen ronden. Niet alleen heb ik heel veel gehad aan zijn proefschrift, ook heb ik hem, met name in mijn begintijd, weten te vervelen met vaak zeer triviale vragen. Na zijn promotie heb ik hem (digitaal) achtervolgd over de oceaan, vanwaar hij altijd trouw en kritisch mijn vragen en opmerkingen beantwoordde.
Het onderzoek met de Huygensdetectoren was niet mogelijk geweest zonder diegenen die haar en de uitlees-elektronica ontworpen en gebouwd hebben: Ton van de Brink, Dirk Balke, Jan Sodaar, Arie de Haas, Kees Oskamp, Marco Voerman en Wieger Smit. Ondanks de haat-liefdeverhouding tussen (sommige van) deze mensen en de Huygensdetectoren heeft hun tomeloze inzet, zowel hier als in het buitenland, ervoor gezorgd dat er überhaupt data is genomen, waarop ik nu kan promoveren.
Cees de Laat is altijd bereid geweest het programma UMAC aan te passen om te voldoen aan mijn specifieke wensen. Ondanks dat dit regelmatig diep in de nacht gebeurde, heb ik hem niet (vaak) op een fout kunnen betrappen. Reint Ostendorf maakte in mijn begintijd deel uit van de Huygensgroep. Ook nadat hij naar Groningen is vertrokken, heeft hij veel voor mij gedaan; met name zijn inspanningen tijdens ons verblijf op GANIL waren zeer waardevol. I would like to thank the LPC for making the MUR available and in particular Alain Pégaire for operating the MUR during my experiment.
Verschillende studenten hebben in de afgelopen vier jaar voor kortere of langere tijd bijgedragen aan het Huygensproject: Maarten Koopmans, Marcel Rossewij, Jeroen Ha-

bets, Wouter Hulsbergen, Mustapha Skefati en Elliott Oti. Allen hebben op positieve wijze bijgedragen aan het onderzoek en de sfeer in de Huygensgroep. Het werk van Wouter en Jeroen is op verschillende manieren terug te vinden in hoofdstuk 3. Met Elliott heb ik het laatste jaar succesvol samengewerkt aan de IQMD simulaties en de gerichte-stroomanalyse welke in sectie 5.2 beschreven staat.
De simulaties van Erik Agterhuis, te vinden in sectie 2.2, en onze discussies hier-over hebben mijn begrip van electronenlawines in driftgassen vergroot. Diewert Inia heeft mij geholpen door met ERD de zuurstofinhoud van mijn trefplaatje te bepalen (sectie 2.4). De bundeltechnici, Henk Kersemaekers, Ruud van Stappershoef en Gerard van Gelder hebben mij verschillende malen een uitstekende testbundel bezorgd. Henk wil ik ook bedanken voor de koffie. Verder hebben Henk Mos en Pim van Ingenegeren mijn netwerkproblemen/blunders altijd snel en vakkundig opgelost. En tenslotte, wil ik Adriaan Buijs, Jos Engelen en Peter de Witt Huberts bedanken voor de allerlaatste correcties en suggesties voor mijn manuscript.
De *finishing touch* is geleverd door Jan de Groot en Jannie van de Visch, die mij enorm hebben geholpen met de kaft van dit boekje.

Naast diegenen die hebben meegewerkt aan het Huygensproject, kon ik gelukkig in mijn directe omgeving ook mensen vinden die hier niks mee te maken hadden en waar ik even stoom kon afblazen. Met Frank Geurts viel over elk onderwerp wel te praten, maar met name onze gezamenlijke interesse in *ramsj*-films heeft ons aardig bezig gehouden. Om de ware aard van onze collega's te leren kennen hebben wij de vakgroep (twee keer) over weten te halen om elkaar met een laserpistool te lijf te gaan. Wim van Rossum en Ivo van Vulpen delen mijn enthousiasme voor de lokale FC en wij hebben dan ook verschillende malen samen het stadion bezocht. De laatste anderhalf jaar heb ik mijn kamer gedeeld met Marcel Merk. Hierdoor is, naast de gezelligheid, ook het geluidsvolume in de kamer aanzienlijk toegenomen. Marcel heeft mij geholpen met een legio aan software-problemen en heeft hij mij bijgestaan in mijn verschillende sollicitatie perikelen. Onze dagelijkse interactie zal ik zeker gaan missen. Bij Birgit Gorter kon ik twee dagen per week mijn hart uitstorten, al dan niet met een gedicht. Tijdens de lange avonden en de koude weekenden in het Robert Van de Graafflaboratorium zijn er twee mensen die er voor gezorgd hebben dat ik niet helemaal eenzaam en alleen was. Ik wil dan ook Renée Heller en Cees Alderliesten aanraden om wat minder hard te gaan werken!
Als laatste wil ik alle (ex)collega's van de vakgroep SAP én van de buurvakgroepen bedanken voor de gezelligheid en de prettige werksfeer.

Naast alle hulp in de werkkring hebben ook (schoon)familie en vrienden mij bijzonder gesteund tijdens mijn promotie. Ik wil dan ook mijn excuses aanbieden aan al mijn vrienden die ik (met name) het laatste halfjaar schromelijk heb verwaarloosd. Ik zal het proberen weer goed te maken.
Zonder mijn moeder was dit boekje nooit tot stand gekomen. Mijn hele leven heeft ze mij aangemoedigd in mijn keuzes, ook waar dat voor haar moeilijk was, en ze heeft me geholpen waar ze kon. De afgelopen vier jaar waren daarop geen uitzondering.
Manon, het is niet altijd even makkelijk om tegelijkertijd te promoveren, maar samen is het ons gelukt. Jij bent mijn belangrijkste steun.

Curriculum Vitae

Op 19 februari 1971 ben ik geboren in London, waar ik de eerste twee jaar van mijn leven woonde. Daarna hebben mijn ouders mij meegenomen naar Gouda. Hier heb ik mijn jeugd doorgebracht. Via Het Bijenkorfje en de Regina Mundischool ben ik in 1983 op het St.-Antoniuscollege beland, waar ik in 1989 mijn diploma voor het V.W.O. behaalde.

In september 1989 ben ik natuurkunde gaan studeren aan de (destijds Rijks) Universiteit Utrecht. Mijn propaedeuse behaalde ik in 1990. Voor mijn afstudeeronderzoek kwam ik eind 1993 terecht bij de vakgroep Atoom- en Grenslaagfysica. Hier kreeg ik de mogelijkheid om een deel van mijn onderzoek in Wales uit te voeren. Dit onderzoek bestond uit de studie van verschillende aspecten van amorf silicium, met name van de invloed van het productieproces op de kwaliteit van de halfgeleider. In het begin van 1994 deed ik enkele maanden onderzoek aan de *Department of Materials Engineering* van de *University of Wales* in Swansea. Met de resultaten van dit onderzoek ben ik in oktober 1994 afgestudeerd in de experimentele natuurkunde.

Op 1 december 1994 ben ik begonnen als assistent-in-opleiding bij de vakgroep Subatomaire Fysica aan de Universiteit Utrecht. Mijn promotieonderzoek richtte zich op de studie van zware-ionenbotsingen bij intermediaire energieën met de Huygensdetectoren. De eerste anderhalf jaar heb ik voornamelijk gewerkt aan de verbetering van de Huygensdetectoren, waarna ik in het voorjaar van 1996 met een groep fysici en technici enkele weken heb doorgebracht bij de *Grand Accélérateur National d'Ions Lourds* (GANIL) in Caen (Frankrijk). Hier hebben we het experiment uitgevoerd dat in dit proefschrift staat beschreven. De afgelopen tweeëneenhalf jaar ben ik bezig geweest met het uitwerken en opschrijven van de resultaten van dit experiment.
In 1996 heb ik de AiO-school Beekbergen en de AiO-school Rolduc bezocht. Tevens heb ik in 1996 en 1997 het *topical lecture*-programma van de onderzoekschool Subatomaire Fysica gevolgd.
Bij het takenpakket van een AiO behoort ook het geven van onderwijs. Ik heb in 1995 en 1996 het werkcollege subatomaire fysica voor 2^{de}-jaars studenten natuurkunde gegeven. In 1996 heb ik de natuurkundepractica begeleid voor 1^{ste}-jaars studenten Natuurwetenschappen Bedrijf & Bestuur en in 1995 en 1997 het natuurkundepracticum voor de 2^{de}-jaars studenten van dezelfde studierichting.

Room for notes